Self-Consistent Green's Functions in Nuclear Matter at Finite Temperature

D I S S E R T A T I O N

Zur Erlangung des Grades eines Doktors
der Naturwissenschaften

der Fakultät für Physik
der Eberhard-Karls-Universität zu Tübingen

vorgelegt von

Tobias Frick
aus Nürtingen

2004

Tag der mündlichen Prüfung:	11. Mai 2004
Dekan:	Prof. Dr. Herbert Müther
1. Berichterstatter:	Prof. Dr. Herbert Müther
2. Berichterstatter:	Prof. Dr. Artur Polls

Contents

Chapter 1

Introduction

The first attempt to describe atomic nuclei goes back to 1936, when Bethe and Weizsäcker proposed the empirical liquid drop model that relates the number of nucleons in a nuclear system to the binding energy [bet36, wei36]. The protons and the neutrons in the nucleus form a fermion many-body system for which the Bethe-Weizsäcker formula models the action of a short-ranged nuclear force and the electromagnetic repulsion between the protons in a phenomenological way.
The volume to surface ratio in a nucleus increases with increasing mass number. Due to the short-ranged character of the nuclear potential, the nucleons in the center of the nucleus are more tightly bound than those at the surface. This leads to an increase of the mean binding energy per nucleon up to the mass number of ^{56}Fe. Beyond, the repulsion due to the large number of positive charged protons that are confined in a small volume overcompensates this energy gain and the mean binding energy is reduced whenever a further particle is added. Thus, for heavy systems, binding energy can only be gained by a reduction of the system size. Processes like the emission of α-particles or spontaneous fission set an upper limit to the mass number of stable nuclei. In low-energy experiments on primordial nuclei, condensed hadronic matter can be studied from the very low-density region in light nuclei up to the central density of the ^{208}Pb nucleus. Over the last 60 years, all possible kinds of experiments on nuclei close to the valley of stability have accumulated a huge amount of information about the structure of the nuclei and the nature of the interaction between the individual constituents, the proton and the neutron.
In modern acceleration facilities, the beam energies are large enough to overcome

the Coulomb barrier between two heavy nuclei. For a short period of time and in a very limited region in space, a hot and dense system can be formed in the laboratory when two heavy ions collide. The particles that are produced (or their decay products) are detected after the collision. Experiments with heavy ion beams are the only possible way to study the properties of matter under extreme conditions in a laboratory on earth.
In astrophysics, hadronic matter occurs in a range of different environments, some of which may be briefly sketched in the following description of the evolution of a massive star that undergoes a type II supernova explosion and forms a neutron star. The matter in an aging star that has gone through various burning stages is composed of electrons and a gas of nuclei. While in the outer layers of the star, still, hydrogen and helium are fused, more heavy elements like carbon, oxygen or neon are burned in the dense and hot interior. The proton to neutron ratio is close to one and the temperature amounts to some hundreds of keV. The pressure is maintained by exothermic nuclear reactions. It stabilizes the system against gravitational collapse that occurs as soon as no further energy can be gained by fusion processes, i.e., when an iron core has been formed in the center of the star. If the mass of the star exceeds the Chandrasekhar limit, it is energetically favorable to form neutrons and neutrinos from highly energetic electrons and protons via weak interaction processes. The collapsing matter in the center of the star forms a high density neutron rich core of uniform structure that is now stabilized by the pressure of the nearly degenerate neutron gas. Due to the low compressibility of this system, the in-falling hot and asymmetric matter is reflected at the core and ejected in the shock wave of a supernova explosion, which is probably boosted by interaction of matter with neutrinos that leave the core region.
The remnant is a hot neutron star with a neutron to proton ratio of the order of ten. It cools down by emission of neutrinos. The composition inside the neutron star changes from the low density crust region, where nuclei are thought to form a lattice structure, embedded in neutron matter, to homogeneous matter in a superfluid state. The composition of matter in the center of the neutron star is speculative. Strange baryons like the Λ or the Σ^- are likely to appear when a certain threshold density is reached. The attractive interaction between nuclear matter and mesons may lead to π^-- or K^--condensates, and a transition to a deconfined phase is also discussed.

The hope to understand the properties of systems of interacting nucleons under all kinds of physical conditions, such as different temperature and density domains,

from a common point of view is a strong motivation for nuclear physicists to investigate microscopic approaches. In low energy nuclear physics, the relevant degrees of freedom are the hadrons, which are treated as structureless particles. Although a truly microscopic description should take into account their composite nature, a quantitative description of hadronic matter starting out from quarks and gluons as the fundamental degrees of freedom is currently out of reach.
Most modern realistic nucleon-nucleon (NN) potentials like the CDBONN [mac96], the Argonne V18 [wir95], or the Nijmegen potentials [sto94] are based on the meson exchange picture that goes back to Yukawa [yuk35]. The complicated structure of the nuclear force is modeled by mesons with different quantum numbers, like the π, the σ, the ρ and the ω, that are emitted by one nucleon and absorbed by another one. The potential models include a number of free parameters that can be fitted in order to accurately describe the properties of the deuteron and the NN scattering phase shifts in free space up to energies of about 300 MeV. The challenge is to derive the properties of matter from such realistic potentials. Defining a 'microscopic approach' in this way has the advantage that the two-body problem of finding the appropriate NN Hamiltonian is decoupled from the many-body problem.

The specific many-body system that will be studied in this Thesis is symmetric nuclear matter (NM). This is a hypothetical, infinite and homogeneous system that consists of an equal fraction of protons and neutrons, in which the electromagnetic interaction, that is responsible for the limitation of the system size, has been turned off artificially. Although NM cannot be observed in nature for this reason, it approximates the conditions in the central region of heavy nuclei. Neutron star matter has also many features in common with NM (for both examples, the restriction is valid that one actually would have to consider asymmetric NM where the neutron fraction is larger than the proton fraction).
The big advantage of an infinite system from the point of view of theoretical physics is, that translational invariance allows much more sophisticated many-body calculations. This makes NM a popular testing ground for nuclear physicists. For instance, the best possible choice for single-particle states in NM are plane waves. This represents a great simplification compared to finite nuclei, where the determination of the appropriate single-particle basis, e.g., in a Hartree-Fock calculation, is a complicated problem itself.

Well-known characteristic features of realistic nuclear forces are the strong repul-

sion at small interparticle distances, mediated by the exchange of the ω meson, and the intermediate-range attraction. It is the repulsive core that prevents a simple mean field description of nuclear systems. A mean field single particle potential is obtained by an averaging of the two-body potential over the Fermi sea. Such an averaging also includes configurations where two nucleons are very close and interpenetrate their repulsive cores. In this way, the repulsive contributions are overestimated and lead to an unbound system. A more realistic model should allow for correlations between individual nucleons that suppress energetically unfavorable configurations. A similar argument applies to the predominantly attractive tensor components of the nuclear interaction. These give rise to important tensor correlations that can enhance favorable configurations in the wave function.

Correlated Fermi liquids can be treated within a variety of distinct many-body theories. The following brief overview tries to give some very basic ideas of the philosophy of different methods that are applied.
Variational methods assume a trial many-body wave function composed of a slater determinant and a correlation operator that describes the deviation of the true wave function with respect to the slater determinant when two particles are close. This operator possesses some functional freedom to be constrained by a variational minimization procedure of the ground state energy of the system. This leads to the so-called Fermi hypernetted-chain (FHNC) integral equations. Refs. [cla79, fan98] are detailed reviews of the variational method.
The variational results for the expectation value of the Hamiltonian represent an upper bound to the ground state energy. A main drawback of the method is that it is quite difficult to find a trial wave function that is reasonable close to the to the true ground state. However, the result can be systematically improved by the method of *Correlated Basis Functions* [cla59, fee69]. In a first step, a complete set of correlated eigenstates is constructed from the variational results. The correlated basis is assumed to be close enough to the exact eigenstates of the Hamiltonian, so that it is sufficient to do low order perturbation theory. Variational methods are successful in reproducing the properties of very dense systems such as liquid ^{3}He, and they are also suitable to describe correlations in NM and finite nuclei [fan84, ben89, ben94].

Monte Carlo sampling methods can be applied to calculations in quantum many-body systems in various ways. In the *Variational Monte Carlo* method, for instance, the expectation value for the ground state energy is explicitely computed

from a trial wave function with an integral in $3N$-dimensional configuration space. The Monte Carlo integral is a summation over the value of the integrand for random configurations, each contribution to the sum being weighted by the square of the wave function. The optimal ground state can be found by minimizing the expectation value for the energy. For an efficient sampling of configuration space, a rejection algorithm must take care that only configurations with a large probability can contribute to the sum.
In so-called *Quantum Monte Carlo* methods, the time-dependent Schrödinger equation for the many-body system is integrated stochastically starting from an initial trial wave function, and the ground state can be projected out. Although Monte Carlo methods are capable to find the exact ground state, it is often not easy to interprete the results in an intuitive way. Another problem is that the complicated structure of the nuclear force makes it very difficult to compute the solution for a large number of particles. Refs. [cep95, gua98] are recent reviews on Monte Carlo methods. Applications for nuclear systems are described in Refs. [car91, pie98].

The *Coupled Cluster* or $\exp(S)$ method is another way to describe correlated many-body systems [kue78]. The exact many-body wave function is generated by the action of the $\exp(S)$ operator on a Slater determinant of model states. S contains a sum of excitation operators — labeled by n — that excite clusters of n particles above the Fermi level, leaving n holes below. Due to the exponential structure of the wave function, independent events of, for instance, two-particle two-hole excitations are contained in the wave function according to their multiplicity, so that double counting of statistically independent events is avoided. This leads automatically to the correct form of a many-body wave function. The Coupled Cluster approach is successfully applicable in all kinds of many-body systems. A review on the method and a comparison to other quantum many-body theories has recently been given by Bishop in Ref. [bis98].

The general idea of *diagrammatic approaches* is to expand physical quantities in terms of diagrams that provide a graphical interpretation of the interaction processes between the relevant degrees of freedom. In nuclear physics, these diagrams are composed of two types of lines that describe the motion of the nucleons and the exchange of bosons between them. A one-to-one correspondence between such diagrams and a set of rules that enable their evaluation must be established. Diagrammatic approaches have the great advantage that they offer intuitive interpretations to the approximations being made. Diagrams can be classified according to

various criteria, among which there are the number of interaction lines or certain structural elements. The importance of certain classes of diagrams for a many-body system can often be judged by physical arguments and in this way, one is then guided to include the most sizable contributions.
A very well known example for a diagrammatic theory is the Brueckner hole-line expansion. In this approach, the shift between the ground state energy of the interacting system and the non-interacting system is expanded in terms of so-called Goldstone diagrams. The criterion for the classification of the diagrams is the the number of fermions in a diagram that are scattered out of their single-particle states, leaving a hole. Following the respective set of rules for the evaluation of the diagrams, each hole-line implies an integration over the phase space of the hole states, and accordingly, each particle line implies an integration over the accessible phase space of the particles. Since the latter is much larger than the former in a low-density system, the diagrams containing many hole lines are suppressed with respect to those with less hole lines.

In the many-body approach that is applied in this Thesis, the quantity that is expanded in terms of diagrams is the single-particle Green's function. This function can be defined for a grand-canonical ensemble and describes the propagation of nucleon states that interact with other nucleons along their path through the many-body system. The approach is related to the Brueckner hole line expansion, however, forward and backward propagation in time is treated on a symmetric footing, while, for instance, in the two-hole line expansion, the latter is neglected. In the Green's functions theory, correlated nucleons are off-shell particles that do not fulfill an energy-momentum relation. The energy of a momentum state k is fragmented over a wide range of energies with a peak at the position of the quasiparticle energy. In scattering experiments on nuclei, such a fragmentation of strength can indeed be observed and quantitatively described in terms of the nuclear spectral function [roh03]. This central quantity arises in a natural way in the formalism of Green's functions.

It has been an aim of various groups working on the Green's function description of nuclear systems, to find a self-consistent Green's function (SCGF) for the many-body problem in the following sense: the Green's function that characterizes the propagating particle must be determined from its interaction with the surrounding nucleons. These particles are also off-shell, and so they should in turn be described by the same Green's function. While it is relatively simple to write down a number

of diagrams that express this concept of self-consistency, it is quite another matter to implement a numerical scheme that solves the problem.
Over more than 15 years, many attempts have been made to find a solution in T matrix approximation. This ansatz takes correlations into account by summing up multiple two-nucleon scattering processes in the medium and becomes exact in the low density limit. In the early works of Ramos, Polls, Dickhoff *et. al.* in Barcelona and St. Louis [ram88, ram89, von90, von91, von93], the problem has been treated at zero temperature in a quasiparticle description. The fragmented strength distribution is approximated by a single Dirac function, the so-called quasiparticle peak, that is located at the quasiparticle energy. Self-consistency is obtained on the level of the quasiparticle spectrum only, but not for the off-shell structure, that can nevertheless be computed. Similar quasiparticle calculations have been performed at finite temperature by Schnell, Alm, Röpke *et. al.* in the Rostock group [snl96, alm96]. Over the recent 5 years, several papers have been published that aim at a self-consistent description of the off-shell structure of the spectral function. Roth, Dickhoff *et. al.* have tried to find a self-consistent solution by approximating the off-shell structure of the nuclear self energy [dic99, rot00] by a set of Gaussians. Bożek *et. al.* from the Krakow group were the first to iterate the full off-shell structure of the spectral function using simple separable NN potentials [boz99, boz01]. Meanwhile, separable versions of more realistic potentials have also been applied [boz03]. Dewulf, Van Neck *et. al.* in the Gent group have approximated the off-shell structure of the spectral function by a number of discrete Dirac peaks [dew00, dew02, dew03]. They have obtained self-consistent results for various realistic potentials.
In this work, a self-consistent solution for the Green's function will be presented for symmetric nuclear matter at finite temperature, using a realistic NN potential. The full off-shell structure of all relevant quantities is calculated on an energy-momentum lattice and no parameterization procedures are applied. The numerical routine that has been developed to solve the many-body problem is capable to obtain very stable results by iteration of the spectral function. The method and some of the results that are presented in this work have already been published in Ref. [fri03].

In Chapter 2, the finite temperature Green's functions formalism is introduced. The notation follows the book of Kadanoff and Baym [kad62]. The basic concepts of the expansion of the propagator are reviewed and the nuclear self energy is defined. To illustrate the failure of the mean field picture, but also to introduce the

concept of self-consistent dressing, the Hartree-Fock approximation is discussed. To improve the description of nuclear matter beyond the mean field level, the T matrix is then introduced as the solution of an integral equation that takes into account in-medium scattering processes of the propagating particle with the surrounding particles to all orders. Some of the limitations of the T matrix formalism are discussed in the final Section of Chapter 2.
The many-body equations in Chapter 2 are formulated in terms of the imaginary time Matsubara Green's function. Chapter 3 contains a description how these are related to physical observables like the spectral function or the momentum distribution. In order to write down a set of equations that can be solved numerically, some manipulations must be applied: the analytic properties of the Green's function and the T matrix can be used to perform the Matsubara summations. Furthermore, the in-medium integral equation must be decomposed into partial waves. Chapter 3 includes a discussion of quasiparticle approximations to the SCGF solution.
Results are presented in Chapter 4. The qualitative features of the T matrix and the nuclear self energy are discussed, and the issue of NN pairing at low temperatures is alluded. The density and the temperature dependence of the nuclear spectral function and the momentum distributions are discussed, and finally, results for the internal energy per particle are presented. The work closes with a summary and some conclusions.

Chapter 2

Many-Body Theory

2.1 Green's Functions at Finite Temperature

The time evolution of a many-body system of identical particles that interact with each other via a two-body potential V is determined by the following expression for the Hamiltonian in second quantization,

$$\begin{aligned} H &= H_0 + H_1 \\ &= \int \mathrm{d}^3x\, \psi^\dagger(\mathbf{x}) \left[-\frac{\nabla^2}{2m}\right] \psi(\mathbf{x}) + \frac{1}{2}\int \mathrm{d}^3x \int \mathrm{d}^3x'\, \psi^\dagger(\mathbf{x})\psi^\dagger(\mathbf{x}')V(\mathbf{x},\mathbf{x}')\psi(\mathbf{x}')\psi(\mathbf{x}). \end{aligned} \tag{2.1}$$

$\psi(\mathbf{x})$ and $\psi^\dagger(\mathbf{x})$ are quantum field operators that describe the annihilation and the creation of particles in the Schrödinger picture. m is the particle mass. For the sake of simplicity, spin and isospin projection indices are understood to be included in the argument $\mathbf{x}$ and each integration over $\mathbf{x}$ implies a summation over the respective projection quantum numbers.
The Green's functions theory allows to expand physical quantities in terms of Feynman diagrams that can be interpreted as elementary descriptions of interaction and propagation processes in the many-body system. The basic physical quantity that is expanded in terms of diagrams is the N-particle Green's function. It describes the propagation of disturbances, that arise from adding or removing N particles, through a medium that is composed of identical particles of the same type. In a

grand-canonical formulation, the one-particle Green's function can be defined in the following way, for both real and imaginary time arguments t, t' [kad62],

$$\mathrm{i}g(\mathbf{x}t;\mathbf{x}'t') = \mathrm{Tr}\{\rho_G\,\mathbb{T}[\psi(\mathbf{x}t)\psi^\dagger(\mathbf{x}'t')]\}. \tag{2.2}$$

$\mathbb{T}$ is the time ordering operator that acts on a product of Heisenberg field operators, $\psi(\mathbf{x}t) = e^{\mathrm{i}tH}\psi(\mathbf{x})e^{-\mathrm{i}tH}$, in such a way that the field operator with the largest time argument t (or it in the case that t is imaginary) is put to the left. A minus sign is generated for each commutation between two field operators within a time ordered product of field operators:

$$\mathbb{T}[\psi(\mathbf{x}t)\psi^\dagger(\mathbf{x}'t')] = \begin{cases} \psi(\mathbf{x}t)\psi^\dagger(\mathbf{x}'t') & \text{for} \quad t > t' \quad \text{or} \quad \mathrm{i}t > \mathrm{i}t' \\ -\psi^\dagger(\mathbf{x}'t')\psi(\mathbf{x}t) & \text{for} \quad t < t' \quad \text{or} \quad \mathrm{i}t < \mathrm{i}t'. \end{cases} \tag{2.3}$$

The trace in Eq. (2.2) is to be taken over a complete basis of the many-body system, which is built of simultaneous eigenstates of the Hamiltonian H and the particle number operator N. The trace is weighted by the statistical operator,

$$\rho_G = \frac{1}{Z}\,e^{-\beta(H-\mu N)}. \tag{2.4}$$

β and μ denote the inverse temperature and the chemical potential of the system, respectively. N counts the total number of particles in the system

$$N = \int \mathrm{d}^3x\,\psi^\dagger(\mathbf{x}t)\psi(\mathbf{x}t). \tag{2.5}$$

N is independent of time, since it commutes with H. The operator $\rho(\mathbf{x},t) = \psi^\dagger(\mathbf{x}t)\psi(\mathbf{x}t)$ measures the density ρ of particles at the space-time point $(\mathbf{x},t)$. The normalization of the probability (2.4) defines the partition function of the grand canonical ensemble,

$$Z = \mathrm{Tr}\,e^{-\beta(H-\mu N)}. \tag{2.6}$$

The general N-particle Green's function is defined analogously, and it contains the time ordered product of N creation operators and N annihilation operators. The two-body Green's function, e.g., has the form

$$\mathrm{i}g_{\mathrm{II}}(\mathbf{x}_1t_1,\mathbf{x}_2t_2;\mathbf{x}_1't_1',\mathbf{x}_2't_2') = \mathrm{Tr}\{\rho_G\,\mathbb{T}[\psi(\mathbf{x}_1t_1)\psi(\mathbf{x}_2t_2)\psi^\dagger(\mathbf{x}_2't_2')\psi^\dagger(\mathbf{x}_1't_1')]\}. \tag{2.7}$$

To circumvent the time ordering operator $\mathbb{T}$, the so-called correlation functions $g^>$ and $g^<$ are now introduced. Depending on whether $t > t'$ or $t < t'$, the one-particle Green's function equals

$$\mathrm{i}\,g^>(\mathbf{x}t;\mathbf{x}'t') = \mathrm{Tr}\{\rho_G\,\psi(\mathbf{x}t)\psi^\dagger(\mathbf{x}'t')\} \tag{2.8}$$

in the former case, and

$$\mathrm{i}\, g^{<}(\mathbf{x}t;\mathbf{x}'t') = -\mathrm{Tr}\{\rho_G\, \psi^{\dagger}(\mathbf{x}'t')\psi(\mathbf{x}t)\} \tag{2.9}$$

in the latter case. Note that for real time arguments, $-\mathrm{i}g^{<}(\mathbf{x}t;\mathbf{x}t)$ is the expectation value of the particle density operator $\rho(\mathbf{x},t)$.
It can be checked from the definitions of the correlation functions that the absolute convergence of the trace is guaranteed by the factor $e^{-\beta(H-\mu N)}$ as long as $0 < \mathrm{Im}\, t,\ \mathrm{Im}\, t' < -\beta$, so that the Green's function is defined for imaginary time arguments in the region $0 < \mathrm{i}t,\ \mathrm{i}t' < \beta$. Due to the invariance of the trace under cyclic permutations, it can be shown that the one-particle Green's functions obeys the following quasi-periodic boundary condition:

$$g(\mathbf{x}, t=0; \mathbf{x}'t') = -e^{\beta\mu} g(\mathbf{x}, t=-\mathrm{i}\beta; \mathbf{x}'t'). \tag{2.10}$$

For the derivation of Eq. (2.10), the relation $\psi(\mathbf{x})e^{\beta\mu N} = e^{\beta\mu(N+1)}\psi(\mathbf{x})$ has been used [kad62].

It is clear from its definition, Eq. (2.2) – Eq. (2.6), that the single-particle Green's function contains a lot of physics. Strategies are required to determine g at least approximately. One possible method was suggested by Martin and Schwinger in Ref. [mar59] and will be sketched in this paragraph. Starting from the equation of motion for the Heisenberg field operator,

$$\mathrm{i}\frac{\partial\psi(\mathbf{x}t)}{\partial t} = [\psi(\mathbf{x}t), H], \tag{2.11}$$

it is possible to derive the equations of motion for the Green's functions. Since the particles move in a strongly correlated many-body system, the motion of a single particle is coupled to the motion of all other particles in the medium. It turns out that for the Hamiltonian (2.1), the equation of motion for the single-particle Green's function involves the two-body potential V and the two-particle Green's function g_{II},

$$\begin{aligned}\left[\mathrm{i}\frac{\partial}{\partial t} + \frac{\nabla^2}{2m}\right] g(\mathbf{x}t;\mathbf{x}'t') \;&+\; \mathrm{i}\int \mathrm{d}^3x''\, V(\mathbf{x},\mathbf{x}'') g_{\mathrm{II}}(\mathbf{x}t,\mathbf{x}''t;\mathbf{x}'t',\mathbf{x}''t^{+}) \\ &= \delta^{(3)}(\mathbf{x}-\mathbf{x}')\delta(t-t').\end{aligned} \tag{2.12}$$

The derivation of this result is reported, e.g., in Refs. [mar59, kad62]. In general, for $N > 1$, the equation of motion for the N-particle Green's function is coupled

to the $(N+1)$-particle Green's function and the $(N-1)$-particle Green's function, if the Hamiltonian contains a two-body interaction. Therefore, a good approximation scheme for $g(\mathbf{x}, t; \mathbf{x}', t')$ must be based upon an appropriate truncation scheme for an expansion of the two-particle propagator. To obtain a closed equation for the single-particle Green's function, the truncated two-particle Green's propagator should be expressed as a function of g. One possible choice is to replace g_{II} by an antisymmetric product of two single-particle Green's functions. In this case, one obtains the Hartree-Fock equations that are discussed in Section 2.2. In a systematic way, it is shown in Refs. [kad62, mat67], how different truncation schemes lead to different levels of approximations.

It has already been mentioned in this Section that it is possible to expand the imaginary time Green's function in a perturbation series that can be interpreted in terms of diagrams. It is this alternative, maybe more intuitive method to find approximation schemes to the single-particle Green's function, that will be adopted in this Thesis.
Before the diagrams are introduced, it is convenient to take advantage of the fact that nuclear matter is a quantum mechanical system that is invariant under translations in space and time as well as under spatial rotations. As a consequence of these symmetries, the Green's function g depends only on the difference variables $\xi = |\mathbf{x} - \mathbf{x}'|$ and $\tau = t - t'$. Therefore, one can identify

$$g(\mathbf{x}t; \mathbf{x}'t') = g(\xi = |\mathbf{x} - \mathbf{x}'|, \tau = t - t'). \tag{2.13}$$

The optimal representation to deal with translationally invariant systems is the momentum-frequency space. The quasi-periodicity of the Green's function along the imaginary time axis suggests a discrete Fourier representation,

$$g(\xi, \tau) = \int \frac{\mathrm{d}^3 k}{(2\pi)^3}\, e^{\mathrm{i}\mathbf{k}\boldsymbol{\xi}} \frac{1}{-\mathrm{i}\beta} \sum_{\nu} e^{-\mathrm{i}z_\nu \tau} g(k, z_\nu), \tag{2.14}$$

where $z_\nu = \frac{\pi\nu}{-\mathrm{i}\beta} + \mu$ are the so-called fermionic Matsubara frequencies, for which the index ν is an odd integer. The Fourier coefficient $g(k, z_\nu)$ is given by the inverse transformation,

$$g(k, z_\nu) = \int \mathrm{d}^3\xi \int_0^{-\mathrm{i}\beta} \mathrm{d}\tau\; e^{-\mathrm{i}\mathbf{k}\boldsymbol{\xi} + \mathrm{i}z_\nu \tau} g(\xi, \tau). \tag{2.15}$$

In a non-interacting system, the single-particle Green's function is defined in the same way as for the interacting system, however, the Hamiltonian is just given by

the kinetic term H_0. Hence, the equation of motion for this object, g^0, reduces to the simple form,

$$\left[\mathrm{i}\frac{\partial}{\partial\tau}+\frac{\nabla^2}{2m}\right]g^0(\xi,\tau)=\delta^{(3)}(\boldsymbol{\xi})\delta(\tau). \tag{2.16}$$

After multiplication by $e^{-\mathrm{i}\mathbf{k}\boldsymbol{\xi}+\mathrm{i}z_\nu\tau}$ and integration over all $\boldsymbol{\xi}$ and all τ in the interval 0 to $-\mathrm{i}\beta$, one obtains a simple expression for the free Green's function in momentum-frequency representation,

$$g^0(k,z_\nu)=\frac{1}{z_\nu-k^2/2m}. \tag{2.17}$$

The perturbation series of the imaginary time Green's function in an interacting many-body system is an expansion in terms of the free Green's function g^0 and the interaction potential V. A comprehensive derivation can be found in Ref. [fet71]. For the slightly different definitions and notations adopted in this Thesis, a recapitulating summary is given in Appendix A. The basic ideas are sketched in a few words below.

The Heisenberg field operators in the definition of the Green's function, Eq. (2.2), are rewritten using interaction picture field operators. As a consequence of this transformation, they are sandwiched between exponential factors of the form $e^{\pm\mathrm{i}t(H-H_0)}$, which means that these factors are functions of the interaction part H_1 of the Hamiltonian only. The exponentials are expanded and this leads to a sum of terms containing thermal averages of time ordered products of creation and annihilation field operators. The different contributions can be classified according to the order in the interaction potential V. Wick's theorem is then applied and it turns out that the time ordered products of field operators can be written as products of free Green's functions.

Up to first oder in V, the perturbation expansion reads (cf. Appendix A):

$$\begin{aligned} g(k,z_\nu) &= g^0(k,z_\nu)+g^0(k,z_\nu) \\ &\quad\times\left[(-1)\mathrm{i}\frac{1}{-\mathrm{i}\beta}\sum_{\nu'}e^{z_{\nu'}\eta}\int\frac{\mathrm{d}^3k'}{(2\pi)^3}\,\langle\mathbf{k}\mathbf{k}'|\,V\,|\mathbf{k}\mathbf{k}'\rangle\,g^0(k',z_{\nu'})\right. \\ &\quad\left.+\,\mathrm{i}\,\frac{1}{-\mathrm{i}\beta}\sum_{\nu'}e^{z_{\nu'}\eta}\int\frac{\mathrm{d}^3k'}{(2\pi)^3}\,\langle\mathbf{k}\mathbf{k}'|\,V\,|\mathbf{k}'\mathbf{k}\rangle\,g^0(k',z_{\nu'})\right]g^0(k,z_\nu)+\cdots. \end{aligned} \tag{2.18}$$

A set of rules, the famous Feynman rules, establishes a one-to-one correspondence between each term in this expansion and a Feynman diagram. In the diagrammatic

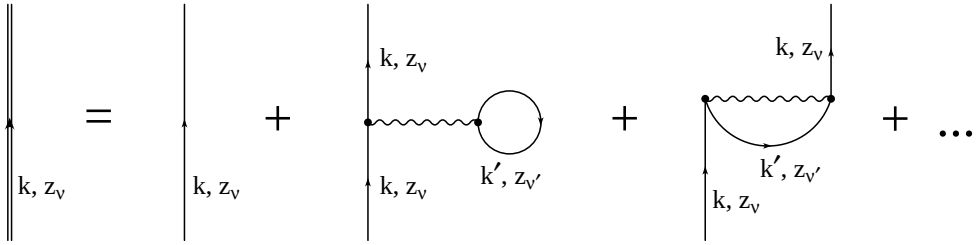

Figure 2.1: *All Feynman diagrams that contribute to the Green's function up to first order in the nuclear two-body interaction.*

language, a free Green's functions g^0 is depicted by a straight line, for which an arrow denotes the direction of momentum flow. A horizontal wavy line characterizes the action of the two-body potential. The full Green's function of the interacting system is represented by a double straight line. Fig. 2.1 shows the translation of Eq. (2.18) into Feynman diagrams. The complete set of Feynman rules is given in Appendix B.

Note that there are no unknown quantities on the right hand side of Eq. (2.18), and this holds for all orders of the expansion. Unfortunately, the number of diagrams grows quickly and the structure of the individual terms becomes more and more complicated, so that it is practically impossible to compute the exact Green's function diagram by diagram. In second order, there are already 10 diagrams to be evaluated. They are shown in Fig. 2.2.

By introducing the concept of the self energy, the number of diagrams that must be retained in the expansion can be reduced efficiently. A self energy insertion is obtained from each diagram by cutting the propagating lines to the external points, as illustrated in Fig. 2.3. In Eq. (2.18), the self energy insertions that correspond to the two first order diagrams are located between the square brackets.

Self energy insertions can be classified into two groups: the reducible self energy diagrams can be decomposed into two parts by cutting a single fermion line only. In Fig. 2.2, such a cut is possible in diagrams (a) – (d), whereas diagrams (e) – (j) are obviously irreducible. It is clear that an arbitrary contribution to the self energy is either irreducible or a combination of at least two irreducible terms. The reducible self energy, Σ^{red}, is composed of both the complete set of the latter type of combined diagrams and all irreducible self energy insertions. In contrast, the irreducible self energy is defined as the sum of all irreducible self energy insertions only, and will be denoted by Σ in the following. By inspection, the reducible

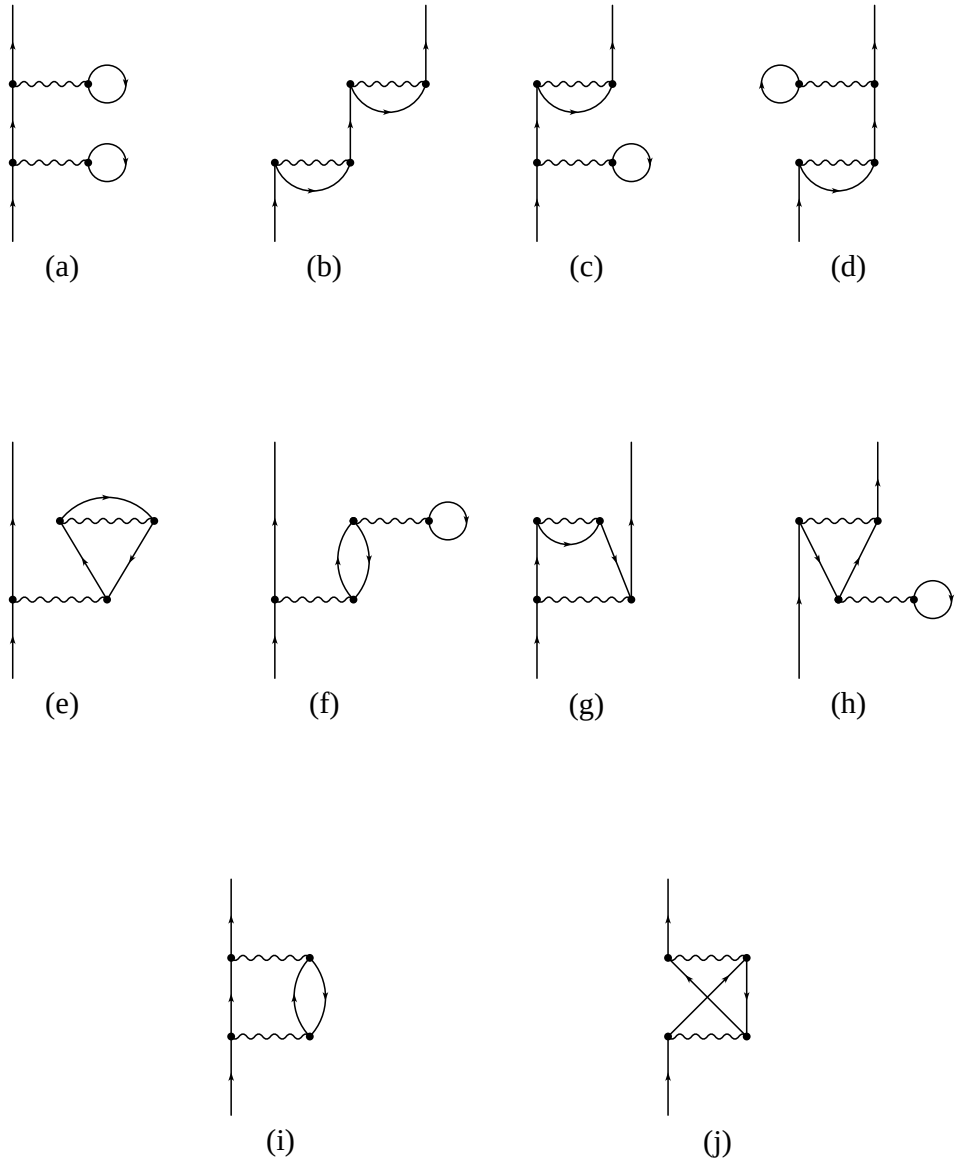

Figure 2.2: *All second order contributions to the Green's function. Diagrams (a) – (d) are reducible, i.e., they are sequential repetitions of first order diagrams. Diagrams (e) – (h) are nested repetitions of first order diagrams in the sense that one first order diagram is inserted in the intermediate line of the other. Diagrams (i) and (j) are the only ones in second order that contain new structural elements.*

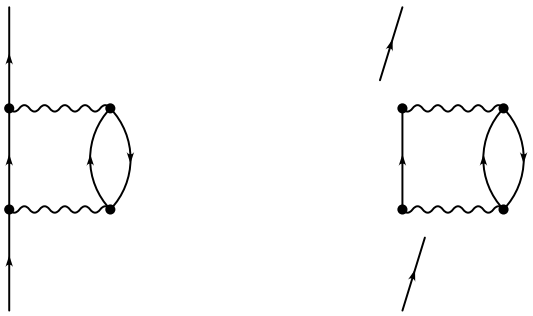

Figure 2.3: *A self energy insertion is obtained from a contribution to the Green's function by cutting the propagator lines to the external points. By removing these lines, external vertex points are generated, that are at most connected to one internal line.*

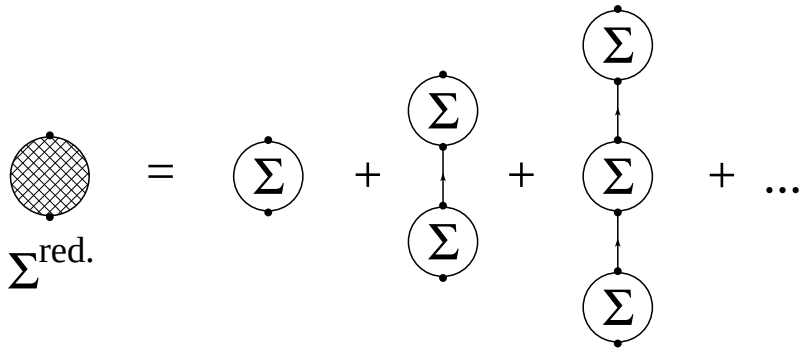

Figure 2.4: *The reducible self energy is composed of the irreducible self energy diagrams plus all possible repetitions of irreducible self energy insertions.*

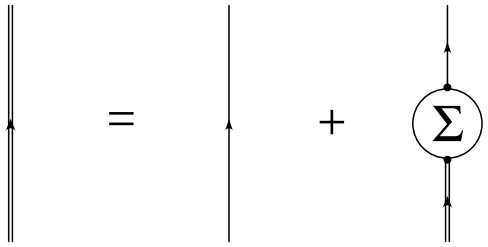

Figure 2.5: Dyson's equation in diagrammatic form.

self energy can be generated by the diagrammatic series depicted in Fig. 2.4. Using the irreducible self energy, one can formulate Dyson's equation that allows to determine the single-particle Green's function,

$$g(k, z_\nu) = g^0(k, z_\nu) + g^0(k, z_\nu)\Sigma(k, z_\nu)g(k, z_\nu). \tag{2.19}$$

All reducible terms can be generated from this recursive expression by repeatedly replacing the full Green's function on the right hand side by the complete right hand side of the equation. Due to the translational invariance in an infinite system, Dyson's equation is an algebraic equation in momentum-frequency space. The solution is trivial,

$$g(k, z_\nu) = \frac{1}{g^0(k, z_\nu)^{-1} - \Sigma(k, z_\nu)}. \tag{2.20}$$

Dyson's equation itself can be represented diagrammatically, as it is shown in Fig. 2.5.

Up to this point, no selection on the diagrams was made on the basis of physical arguments. It turns out in the derivation of the diagrammatic expansion of the single-particle Green's function that only connected diagrams contribute (cf. Appendix A). By introducing the concept of the self energy, it is immediately clear from the structure of Dyson's equation that only one-particle irreducible self energy diagrams need to be considered. However, the number of irreducible diagrams increases in each order and their structure gets more and more complicated. A direct calculation of all self energy diagrams is impossible. Fig. 2.6 gives an impression of the variety of diagrams that can appear up to fifth order. All diagrams in one column belong to the same order, which means that they have the same number of interaction lines. Diagrams that have a similar structure are grouped in each row. Of course, the list represents only a selection.

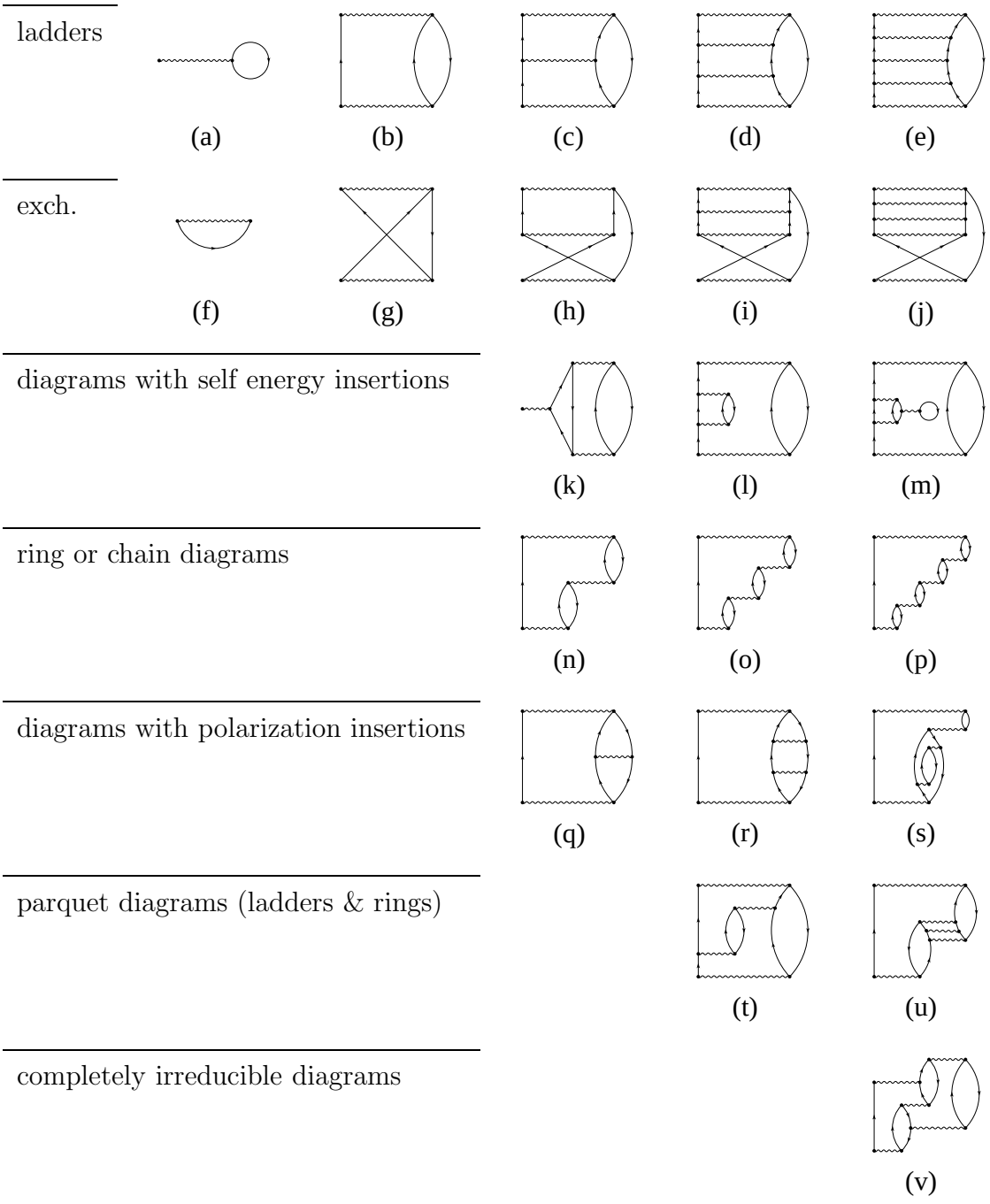

Figure 2.6: *A selection of contributions to the irreducible self energy. The diagrams are classified according to their order (from left to right) and their type (from top to bottom).*

2.2 Self-Consistent Hartree-Fock

At first sight, one is tempted to start to evaluate the self energy diagrams according to the ordering in the perturbation expansion, starting with the two first order diagrams depicted in Fig. 2.6. This may be a good approximation if the potential is small in the sense that the terms of order $n+1$ are suppressed by some factor with respect to the terms of order n. In the present Section, it is illustrated that this assumption is wrong for any realistic nuclear potential. However, the failure of the Hartree-Fock (HF) approximation is a motivation for more sophisticated summation methods for diagrams. Besides, studying this oversimplified ansatz, techniques like contour integration or the concept of self-consistent renormalization can be introduced in a clear manner.
From the Feynman rules in momentum space, it follows that the first order self energy has the form

$$\Sigma^{(1)}(k) = -\mathrm{i}\frac{1}{-\mathrm{i}\beta}\sum_{\nu} e^{z_\nu \eta}\int \frac{\mathrm{d}^3k'}{(2\pi)^3}\,\langle \mathbf{k}\mathbf{k}'|\,V\,|\mathbf{k}\mathbf{k}'\rangle_A\, g^0(k', z_\nu), \tag{2.21}$$

where the subscript A indicates an anti-symmetric matrix element $|\mathbf{k}\mathbf{k}'\rangle_A = |\mathbf{k}\mathbf{k}'\rangle - |\mathbf{k}'\mathbf{k}\rangle$.

The sum in Eq. (2.21) is a structure that occurs frequently in statistical Green's functions theory. It can be evaluated by applying a transformation into a contour integral. Consider the function

$$-\beta f(z) = \frac{-\beta}{e^{[\beta(z-\mu)]}+1}. \tag{2.22}$$

This function has simple poles with unit residues at the fermion Matsubara frequencies z_ν. Since none of these poles coincides with the one of $g^0(k,z) = [z-\epsilon(k)]^{-1}$, one can write

$$\sum_{\nu} e^{z_\nu\eta} g^0(k, z_\nu) = -\beta \int_C \frac{\mathrm{d}z}{2\pi\mathrm{i}} e^{z\eta} f(z) g^0(k,z), \tag{2.23}$$

where C is a contour that encircles all poles of f in the positive sense. The contour C can be deformed to the contour C' as depicted in Fig 2.7. Due to the convergence factor, the contributions from the arcs vanish everywhere in the complex plane, and one is left with a contour that encircles the pole of g^0 at $z=\epsilon(k)$, with residue

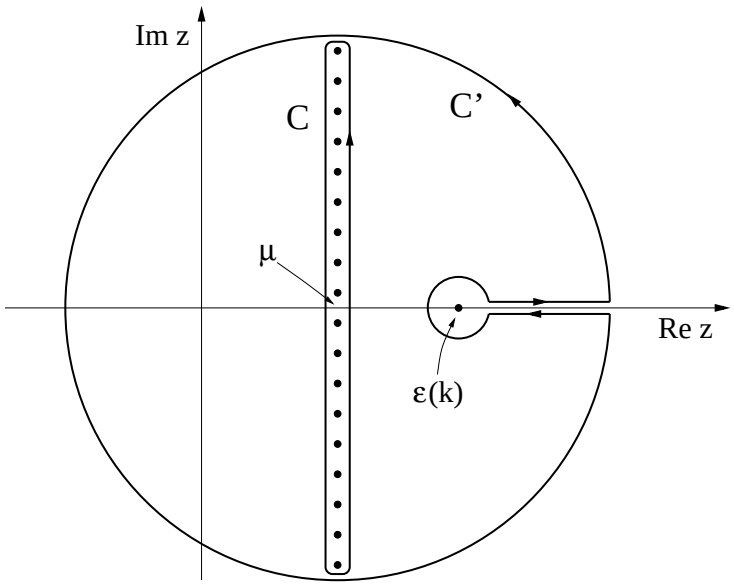

Figure 2.7: *Deformation of the contour C to the contour C'. The dots that are encircled by C are the complex poles of the Fermi function. Integrating along C', the contributions from the arcs vanish, and the result is determined by the residue of the pole of the Green's function on the real axis, at $z = \epsilon(k)$. Note that C' encircles this pole in the negative sense.*

$\mathrm{Res}\,[g^0(z), \epsilon(k)] = +1$, in the negative sense, yielding a minus sign. Hence, the frequency summation yields

$$\sum_\nu e^{z_\nu \eta} g^0(k, z_\nu) = \beta f(\epsilon(k)), \tag{2.24}$$

and the first order self energy becomes

$$\Sigma^{(1)}(k) = \int \frac{\mathrm{d}^3 k'}{(2\pi)^3} \langle \mathbf{k}\mathbf{k}' | \, V \, | \mathbf{k}\mathbf{k}' \rangle_A \, f(\epsilon(k')). \tag{2.25}$$

By construction of the perturbation expansion, $\epsilon(k)$ is the energy of a free nucleon with momentum k, and thus $f(\epsilon(k))$ is the occupation probability of the unperturbed system,

$$f(\epsilon(k)) = [e^{\beta(\frac{k^2}{2m} - \mu)} + 1]^{-1}. \tag{2.26}$$

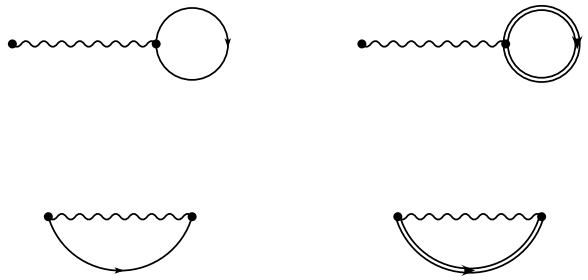

Figure 2.8: *Self-consistent renormalization on the level of the HF self energy. The free Green's function in the first order contributions (left) are replaced by full propagators that, in turn, contain iterated self energy insertions of the first order type (right). By using antisymmetrized potential matrix elements, the exchange diagrams (lower diagrams) are assumed to be automatically included in the notation for the direct terms and will not be displayed separately from now on.*

The interpretation of the first order result is the following: Eq. (2.25) takes into account the interaction of a nucleon in an initial state $\mathbf{k}$ with all occupied states via the bare NN potential. Only processes are allowed in which the final state is also $\mathbf{k}$. Since the particles are not distinguishable, one should take care to include both the direct forward scattering term and the exchange term, where the initial nucleon ends up in an state $\mathbf{k}'$ and the nucleon occupying that state is scattered into the state $\mathbf{k}$.

It is important to emphasize that Eq. (2.25) contains an inconsistency. The external nucleon interacts with a Fermi sea of nucleons that are non-interacting. However, a consistent solution should contain a Fermi sea of nucleons that interact with each other in the same way as with the external nucleon. A natural way to cure this problem is to replace the non-interacting propagator line g^0 in the first oder self energy by a Green's function that is obtained from Dyson's equation (2.19), in which one inserts the first order approximation to the irreducible self energy, $\Sigma^{(1)}$. This is shown diagrammatically in Fig. 2.8. The two equations form a problem that has to be solved self-consistently, the solution is the HF self energy Σ^{HF} and the HF Green's function, g^{HF}. This procedure is called self-consistent renormalization. Whereas the first order self energy contains only the simplest two diagrams of the complete set, as shown in the left part of Fig. 2.8, the self-consistent HF self energy diagrams include implicitly contributions to all

orders in the interaction potential — successive first-order self energy insertions, generated by Dyson's equation. Note that the second order diagrams (a) – (h) in Fig. 2.2 are included in a self-consistent HF Green's function. The only formal difference between the first oder self energy $\Sigma^{(1)}$, Eq. (2.25), and the self-consistent HF self energy Σ^{HF} for a uniform system is the replacement of the free occupation probability by

$$n^{HF}(k) = [e^{\beta(\epsilon(k)-\mu)} + 1]^{-1}, \tag{2.27}$$

where $\epsilon(k) = \frac{k^2}{2m} + \Sigma^{HF}(k)$. This structural resemblance is due to the fact that the mathematical form of g^{HF} is equal to the structure of the free Green's function. The internal energy per particle in HF approximation is given by the integral over all occupied states [fet71],

$$\frac{E_{HF}}{A} = \frac{\gamma}{\rho} \int \frac{\mathrm{d}^3k}{(2\pi)^3} \left[\frac{k^2}{2m} + \frac{1}{2}\Sigma^{HF}(k) \right] n^{HF}(k), \tag{2.28}$$

where $\gamma = (2s+1)(2t+1)$ is the spin-isospin degeneracy factor of symmetric nuclear matter, composed of nucleons with spin $s = \frac{1}{2}$ and isospin $t = \frac{1}{2}$. The explicit factor $\frac{1}{2}$ in Eq. (2.28) must be included to avoid double counting of self energy contributions. The density of the system is

$$\rho = \gamma \int \frac{\mathrm{d}^3k}{(2\pi)^3} n^{HF}(k). \tag{2.29}$$

In practice, the density is fixed at the beginning of the calculation, and Eq. (2.29) is then used to determine the chemical potential μ.

Unfortunately, the HF approximation is not very well suited for a description of nuclear systems with realistic potentials. In Fig. 2.9, numerical results for the Argonne V18 potential and the CDBONN potential are compared at different temperatures. Up to a laboratory energy of 350 MeV, both of them fit the available experimental two-nucleon data to a very high level of accuracy with a χ^2 value per data point close to one. However, in a many-body calculation on the HF level, they fail completely. First of all, neither of the two potentials is able to describe a bound system (right panel): the internal energy is positive over the whole density range, the Argonne potential yielding even more repulsion than the CDBONN potential. The repulsive effect at finite temperature amounts to about 4 MeV at saturation density and this is predominantly due to an increase of the

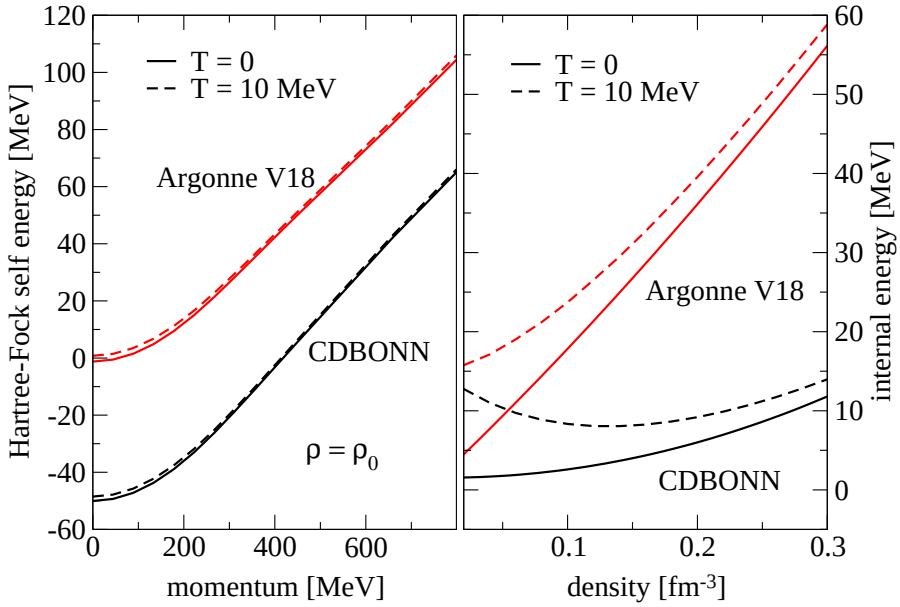

Figure 2.9: *Results of a Hartree-Fock calculation for two different realistic potentials. The HF self energy at saturation density, $\rho_0 = 0.16\,fm^{-3}$, is shown in the left panel. Only a small repulsion at finite temperature is observed. The internal energy is shown in the right panel. At saturation density, the temperature effect is about 4 MeV.*

kinetic energy term in Eq. (2.28). This can be inferred from the HF self energies, which display only a weak temperature dependence (left panel).
The large difference between the two potentials of about 50 MeV for the self energies and more than 20 MeV for the internal energies shows drastically how sensitive a HF calculation is to the structure of those components in the nuclear potential that are not fixed by two-nucleon scattering data. In particular, the HF approximation neglects correlation effects, which means that the wave function is an antisymmetric product of plane waves. These plane waves feel the full short-range repulsion of the potential if two (or more) nucleons are close, and the large deviations for different realistic NN potentials reflect basically the different modeling of the repulsive core. One must conclude from these observations, that correlation effects between nucleons play an important role. In order to improve the description of nuclear matter, one should therefore include those type of higher order diagrams in the perturbation expansion that are relevant for two-body correlations.

2.3 Ladder Approximation to the Self Energy

The Hartree-Fock approximation to the self energy describes particles that move in an averaged potential generated by all other particles in the Fermi sea. Since a nucleon with a certain momentum **k** either stays in its orbit or is exchanged with a particle in an occupied orbit, a redistribution of momentum or spin-isospin quanta with other nucleons propagating along with it in the medium cannot be described within the HF formalism. Only the consideration of multiple interaction processes between co-propagating pairs or clusters will yield information about the correlated system. The suppression of configurations in which two nucleons are very close such that they feel their mutual repulsion, and, in turn, the enhancement of energetically favorable groupings is an important effect to be expected from two-body correlations. In this way, the self energy will become more attractive.
The approximation scheme to the self energy that will be introduced in the present section takes multiple scattering processes into account. This leads to a coupled set of equations for the correlated many-body system, that is formulated in terms of self-consistent Green's functions. It is the main focus of this Thesis to find a solution to these equations. The techniques that are necessary to solve the SCGF equations will be described in detail in Chapter 3 and results are presented in Chapter 4.

It is well known from NN scattering in free space that a resummation of one-boson exchange processes to all orders in the Lippman-Schwinger equation is required to achieve an exact description of experimental data. Summation techniques of this kind are called non-perturbative. In contrast, in perturbative approaches, one is obliged to evaluate the perturbation series diagram by diagram, starting with the first order contributions. Due to the repulsive core of the nucleons, the matrix elements containing the bare potential are large, and the perturbation series converges too slowly if at all. Under the assumption that the dominant contribution to the self energy from the higher order diagrams is due to multiple scattering processes of only two participant nucleons, it is reasonable to apply a similar non-perturbative method like in free space to the many-body system. This approximation should work well in the limit of low densities. Around the central density of ^{208}Pb, only about 20% of the space is occupied by the repulsive core of the nucleons, which means that the range of the interaction is smaller than the mean interparticle distance, so that the assumption of a dilute system is justified to some extent.

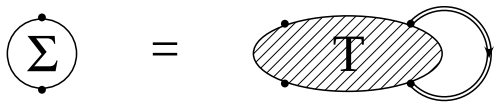

Figure 2.10: *The ladder self energy approximation in a diagrammatic representation. The exchange diagrams are included since the T matrix elements are assumed to be anti-symmetrized.*

There are of course other processes that start to play a role, which are neglected by choosing a low density ansatz; some of them are briefly discussed in Section 2.4. In Fig. 2.6, the direct self energy diagrams, (a) – (e), as well as the corresponding exchange terms, (f) – (j), that are contained in the so-called T matrix approximation, are depicted up to fifth order. Due to their structure, they are called ladder diagrams. Note that the ladder series includes the two first order diagrams.
The structure of the self energy in ladder approximation is similar to Eq. (2.21),

$$\Sigma^L(k, z_\nu) = -\mathrm{i}\frac{1}{-\mathrm{i}\beta}\sum_{\nu'}\int\frac{\mathrm{d}^3k'}{(2\pi)^3}\,\langle\mathbf{k}\mathbf{k}'|T(z_\nu + z_{\nu'})|\mathbf{k}\mathbf{k}'\rangle_A\, g(k', z_{\nu'}), \tag{2.30}$$

and it is shown diagrammatically in Fig. 2.10. The T matrix has been introduced as an auxiliary quantity representing an effective two-body interaction that contains a resummation of all ladders; it is defined as

$$\begin{aligned}\langle\mathbf{k}\mathbf{k}'|T(Z_\Lambda)|\mathbf{p}\mathbf{p}'\rangle \;=\; & \langle\mathbf{k}\mathbf{k}'|V|\mathbf{p}\mathbf{p}'\rangle + \mathrm{i}\left(\frac{1}{-\mathrm{i}\beta}\right)^2\sum_{\nu_1\nu_2}\int\frac{\mathrm{d}^3k_1}{(2\pi)^3}\int\frac{\mathrm{d}^3k_2}{(2\pi)^3}\\ & \times\langle\mathbf{k}\mathbf{k}'|V|\mathbf{k}_1\mathbf{k}_2\rangle\, g(k_1, z_{\nu_1})g(k_2, z_{\nu_2})\,\langle\mathbf{k}_1\mathbf{k}_2|T(Z_\Lambda)|\mathbf{p}\mathbf{p}'\rangle\\ & \times(2\pi)^3\delta^{(3)}(\mathbf{k}+\mathbf{k}'-\mathbf{k}_1-\mathbf{k}_2)(-\mathrm{i}\beta)\delta_{\Lambda;\nu_1+\nu_2}.\end{aligned} \tag{2.31}$$

Graphically, the ladder equation is depicted in Fig. 2.11. The delta functions guarantee the conservation of the center of mass momentum and the total pair frequency $Z_\Lambda = \frac{\pi\Lambda}{-\mathrm{i}\beta} + 2\mu$, where Λ is an even integer. One can check that all orders of direct and exchange contributions to the self energy in ladder approximation are reproduced according to the Feynman rules (cf. Appendix B) by repeatedly inserting Eq. (2.31) into Eq. (2.30). Note, however, that the free propagators have been replaced by the full Green's functions, following the procedure of self-consistent renormalization that was explained in Section 2.2. As in the case of the

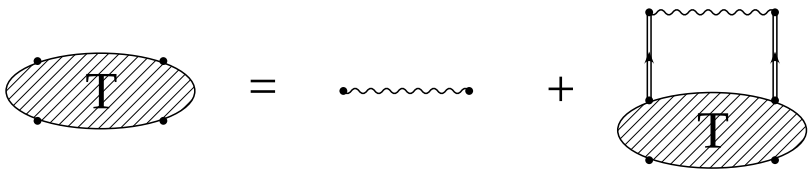

Figure 2.11: *The graphical representation of the T matrix. The structure is similar to the scattering matrix that describes NN collisions in free space, but the propagators are dressed in-medium Green's functions.*

self-consistent HF approximation, the dressing of the particle lines implicates that an additional subset of self energy contributions, the ones containing self energy insertions, is implicitly included. Typical examples are given by the diagrams (k), (l) and (m) in Fig. 2.6.
Both Eq. (2.31) and Eq. (2.30) contain Matsubara summations. After performing the trivial summation over ν_2 in the ladder equation, the non-interacting two-particle propagator appears:

$$g^0_{\mathrm{II}}(k_1, k_2, Z_\Lambda) = -\frac{1}{\beta}\sum_{\nu_1} g(k_1, z_{\nu_1}) g(k_2, Z_\Lambda - z_{\nu_1}). \tag{2.32}$$

The evaluation of the remaining Matsubara sum in this interesting quantity is postponed to Section 3.2. In principle, it follows similar lines as the frequency summation carried out in Section 2.2, however, due to the more complicated structure of the renormalized Green's functions, a spectral decomposition of g is required. The evaluation of the frequency sum in the ladder self energy requires a spectral decomposition of the T matrix and is also discussed in Section 3.2.

2.4 Beyond the Ladder Approximation

In the final Section of this Chapter, the following three questions will be addressed: what are the improvements that can be expected from the T matrix approach, what are possible shortcomings and in which way one might be able to further improve the description of nuclear matter.
The T matrix scheme offers an approximate solution to the nuclear many-body problem. It is a non-perturbative method that is capable to sum up the specific

class of ladder diagrams to all orders. By dressing of the propagators, the variety of diagrams that are included in this set becomes very rich and detailed information about the energy and momenta of nucleons in the medium can be expected. The two-particle Green's function, Eq. (2.32), is a product of two SCGF's and treats forward (particle-particle) propagation and backward (hole-hole) propagation on the same footing, so that intermediate NN states are correctly described. The method constitutes a consistent type of approximation, but one should not forget that it is focused predominantly on the problem of adequately treating the short-range correlations. Remember that in Section 2.2, it was argued that these contributions were likely to improve the results for bulk properties of the nuclear medium, in particular the internal binding energy, with respect to the poor HF result. Long-range low-energy excitations in the region around the Fermi surface are not as well incorporated in the ladder approximation.
It can be considered as one of the drawbacks of the method, that it is difficult to predict the importance of the retained diagrams relative to the neglected terms. The Green's function is not expanded in terms of a small quantity as, e.g., the *hole-line* in the Goldstone diagrams for the energy in the Brueckner hole-line expansion. Carried out to all orders, Brueckner and Green's function's theory must yield the same result. Both methods should work well at low densities, but in contrast to the latter, the former method can be characterized as an expansion in powers of the density, in which the suppression of diagrams that contain more and more hole-lines is guaranteed. Indeed, a reasonable convergence seems to be achieved already at the three hole-line level, as was shown by Baldo and collaborators in Ref. [son98]. In the same paper, it is demonstrated that, although the absolute three hole-line contribution to the internal energy is small, this partly due to a cancellation effect between repulsive Goldstone diagrams of the ladder type with dressed particle lines and attractive ring diagrams.
In the Green's functions approach, it is difficult to control the error that is made by neglecting diagrams of other structural types, e.g. the ring or chain diagrams that are depicted in Fig. 2.6 (n), (o) and (p). The lowest order self-energy contributions of the ring type is of third order in the interaction potential. Similar non-perturbative summation techniques as for the ladder diagrams exist for the complementary sector of long-ranged, low-energy and collective excitations in many-body systems. These methods are based on a partial summation of rings, which is described in many textbooks on Green's functions, e.g., in Refs. [mat67, fet71, neg88]. A consistent treatment of the long-range excitations in nuclear matter is related to

the problem of pion condensation and the unresolved issue of the role of $\Delta(1232)$ excitations. These effects could have a large effect on the nuclear binding energy. Further information on the topic can be found, e.g., in Refs. [dic81, dic82, dic83].
Diagrammatic Green's functions theory can be improved systematically: the parquet equations [jac82] allow a consistent resummation of self energy contributions of the ladder type and the ring type as well as generalized types of diagrams that include mixtures of both. Two examples are shown in Fig. 2.6. Diagram (t) is generated from the ladder diagram (c) by augmenting the middle rung with a polarization insertion, and in diagram (u), a ladder was inserted in the third order ring diagram (n). The parquet equations can be formulated as a closed system of equations in terms of the dressed Green's functions, similarly to the dressed ladder equations for the T matrix. A solution of the parquet equations for the full nuclear many-body system has never been achieved so far. In any case, it would go far beyond the SCGF approximation applied in this Thesis.
Still, there are diagrams that are not included in the parquet approximation. They first appear in fifth order in the potential. One example is given by Fig. 2.6 (v). These fully irreducible diagrams can be related to the so-called elementary diagrams of the hypernetted chain summation techniques.

Chapter 3

Ladder Approximation in Detail

3.1 The Spectral Function

In the previous Chapter, it was shown how the Green's function can be described in different approximations by applying diagrammatic methods. Due to the formal identity of the the the thermal weight factor $e^{\beta H}$ and the time evolution factor $e^{\mathrm{i}tH}$ for $t = -\mathrm{i}\beta$, the diagrammatic expansion for the Green's function holds for a bounded interval in the imaginary time domain or, equivalently, at discrete Matsubara frequencies. However, physical quantities that depend on real-time or frequency variables have a simpler interpretation. Since we deal with functions that are analytic in certain regions of the complex ω plane, it is possible to use the concept of analytic continuation to learn about the properties of the Green's function or the self energy along the real time or frequency axis. A very interesting quantity in this context is the spectral function, that will be introduced in this Section.

It was mentioned in the paragraph after Eq. (2.9), that $-\mathrm{i}g^<(\mathbf{x}t;\mathbf{x}t)$ is the particle density of the system at the real spacetime point $(\mathbf{x}, t)$. The Fourier transform of the correlation function in a uniform system, along the real time axis, reads

$$g^<(k,\omega) = -\mathrm{i}\int \mathrm{d}^3x \int_{-\infty}^{+\infty} \mathrm{d}t\, e^{-\mathrm{i}\mathbf{k}\mathbf{x}+\mathrm{i}\omega t} g^<(x,t), \tag{3.1}$$

where the explicit factor $-\mathrm{i}$ is included. This function describes a spectral distribution of the number of particles in the state k. To make the point very clear,

$g^<(k,\omega)\,\mathrm{d}\omega/2\pi$ is the probability to remove a particle with an energy ω from the momentum state k of the many-body system. In the same way, one can define another real and positive function that is interpreted as the spectral probability to attach a further particle with energy ω to the momentum state k,

$$g^>(k,\omega) = \mathrm{i}\int \mathrm{d}^3x \int_{-\infty}^{+\infty} \mathrm{d}t\, e^{-\mathrm{i}\mathbf{kx}+\mathrm{i}\omega t} g^>(x,t). \tag{3.2}$$

For a given momentum state k, the correlation function $g^<(k,\omega)$ bears information about the spectral distribution of the thermally populated energy domain, while $g^>(k,\omega)$ describes the capability of the system to pick up particles in the energy region that is not accessible in thermal equilibrium. In other words, $g^>(k,\omega)$ describes the *potential* occupation of state k. The sum of both functions is a positive quantity that defines the spectral function,

$$A(k,\omega) = g^>(k,\omega) + g^<(k,\omega). \tag{3.3}$$

An important property of the spectral function $A(k,\omega)$ — and the reason why one can speak of probabilities — is its normalization to one. The Pauli exclusion principle requires that each state k can at most be occupied by only one particle, so that the following sum rule must be fulfilled,

$$\int_{-\infty}^{+\infty} \frac{\mathrm{d}\omega}{2\pi} A(k,\omega) = 1. \tag{3.4}$$

From Eq. (3.1) and the quasi-periodicity condition, Eq. (2.10), it follows that the Fourier transformed correlation functions are related by detailed balance,

$$g^>(k,\omega) = e^{\beta(\omega-\mu)} g^<(k,\omega). \tag{3.5}$$

Using this condition, the correlation functions can be expressed by the spectral function,

$$g^<(k,\omega) = f(\omega) A(k,\omega). \tag{3.6}$$

and

$$g^>(k,\omega) = [1 - f(\omega)] A(k,\omega) \tag{3.7}$$

In the limit of zero temperature, $g^<$ and $g^>$ are the hole spectral function and the particle spectral function, respectively [ben89, von93].
The Fourier coefficients of the imaginary time Green's function and the spectral function are related by the Lehman decomposition [kad62],

$$g(k, z_\nu) = \int_{-\infty}^{+\infty} \frac{\mathrm{d}\omega}{2\pi} \frac{A(k,\omega)}{z_\nu - \omega}. \tag{3.8}$$

$g(k, z_\nu)$ can be continued analytically to all non-real frequencies, just by replacing the Matsubara frequencies z_ν by a complex number z. The Plemelj identity,

$$\frac{1}{\omega + \mathrm{i}\eta} = \frac{\mathcal{P}}{\omega} - \mathrm{i}\pi\,\delta(\omega), \tag{3.9}$$

is used to separate the real and the imaginary part of the retarded propagator $g(k, \omega + \mathrm{i}\eta)$ from each other. $\mathcal{P}$ denotes the principal value. The spectral function is then related to the imaginary part of the retarded propagator,

$$A(k,\omega) = -2\,\mathrm{Im}\,g(k, \omega + \mathrm{i}\eta). \tag{3.10}$$

For practical purposes, the spectral function is computed from the self energy by inserting the solution of Dyson's equation, Eq. (2.20), into Eq. (3.10). This yields

$$A(k,\omega) = \frac{-2\,\mathrm{Im}\,\Sigma(k, \omega + \mathrm{i}\eta)}{[\omega - \frac{k^2}{2m} - \mathrm{Re}\,\Sigma(k,\omega)]^2 + [\mathrm{Im}\,\Sigma(k, \omega + \mathrm{i}\eta)]^2}. \tag{3.11}$$

If the self energy had no frequency dependence, the spectral function would have a perfect Lorentzian shape. Due to the explicit ω dependence, there are deviations, but the Lorentzian provides a rather satisfying description of the spectral function in the region around the peak of the spectral function.
A special case is sketched in the following. For non-interacting particles or in a system where interactions are mediated via a mean field described in the HF approximation, the self energy has no imaginary part. But also in a correlated system, the imaginary part can be neglected as an approximation. If only the real part of the self energy is considered, it follows from Eqs. (3.9) and (3.10) that the spectral function is just a delta spike,

$$A(k,\omega) = 2\pi\delta(\omega - \epsilon(k)). \tag{3.12}$$

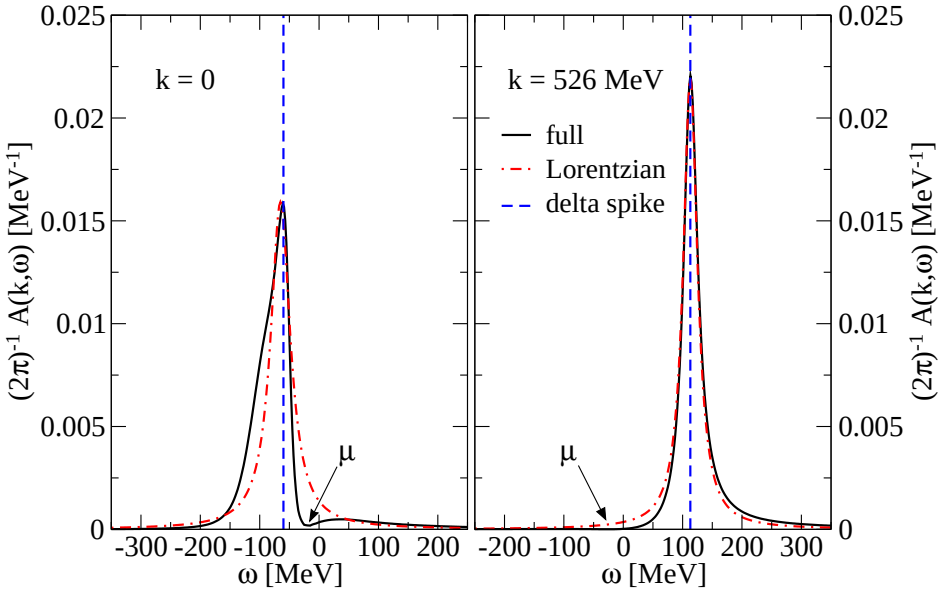

Figure 3.1: *Spectral function in nuclear matter for $k = 0$ and $k = 526\,MeV$. The solid line is a non-trivial spectral function, calculated from Eq. (3.11). The dash-dotted line is the Lorentzian approximation and the dashed line is the quasiparticle delta spike. The calculation was performed at $T = 3\,MeV$ and a density of $\rho = 0.16\,fm^{-3}$. The chemical potential is also indicated.*

$\epsilon(k)$ is the single-particle energy for a particle with momentum k,

$$\epsilon(k) = \frac{k^2}{2m} + \mathrm{Re}\Sigma(k, \epsilon(k)). \tag{3.13}$$

Since an energy-momentum relation of this type is commonly associated with the particle character of matter, an approximation scheme for which the spectral function has the form of Eq. (3.12) is called quasiparticle picture. In Fig. 3.1, a non-trivial spectral function, the Lorentzian approximation and a quasiparticle delta spike are shown. The peak of the spectral function is located at the quasiparticle energy. Quasiparticle approximations to the SCGF formalism are discussed in Section 3.5. One should keep in mind that it is the correlations between the particles that lead to the non-existence of an energy-momentum relation, and this implies the use of a spectral function in advanced many-body calculations.
It is a very nice feature of the Green's functions formalism that it provides imme-

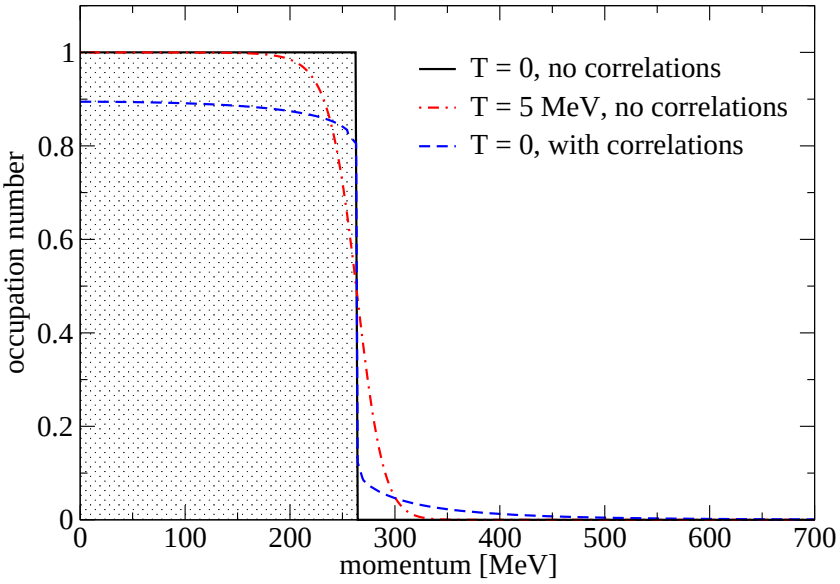

Figure 3.2: *Momentum distribution in nuclear matter. At zero temperature, there is a sharp Fermi surface located at k_F (solid line). The step is smeared out at finite temperature (dash-dotted line). Due to correlations, the occupied states are depleted and the states above k_F display a finite occupation (dashed line).*

diate access to the nucleon spectral function. On the one hand, it follows from the spectral representation, Eq. (3.8), that the knowledge of the spectral function is equivalent to the information contained in the single-particle Green's function. On the other hand, $A(k,\omega)$ also provides a link between theory and experiment. At zero temperature, for instance, the cross section of a proton knock-out reaction is proportional to $A(k,\omega)$, which is hardly surprising, because this was interpreted as the probability to find a nucleon with momentum k and energy ω in the many-body system.

It is clear from the interpretation of $g^<(k,\omega)$, that the overall occupation number for a state with momentum k is given by the integral

$$n(k) = \int_{-\infty}^{+\infty} \frac{\mathrm{d}\omega}{2\pi} A(k,\omega) f(\omega). \tag{3.14}$$

In turn, the depletion of a state k can be expressed by the difference

$$d(k) = 1 - n(k). \tag{3.15}$$

Already at zero temperature, a non-trivial nucleon spectral function in nuclear matter yields occupation numbers different from unity below the Fermi momentum k_F, and a finite fraction of high-momentum nucleons, see Fig. 3.2. This effect is only due to NN correlations and cannot be described within the traditional shell model or the HF picture, where the states below (above) the Fermi momentum are considered to be fully occupied (unoccupied). In hot systems, there is also a temperature induced depletion effect, especially for the weakly bound states.
The density ρ of the system is deduced from the occupation number $n(k)$,

$$\rho = \gamma \int \frac{\mathrm{d}^3 k}{(2\pi)^3} n(k). \tag{3.16}$$

Again, $\gamma = 4$ is the degeneracy factor for spin-isospin symmetric nuclear matter.
Experimental evidence on the effects of short range correlations on the occupation of low-lying states can be deduced from the analysis of nucleon knock-out reactions [sic91, bat01]. A recent analysis of the $(e, e'p)$ reaction on ^{208}Pb, covering a wide range of missing energies, indicates that the deeply bound proton states are on average depleted by $(22 \pm 8)\%$ [bat01]. Another experiment of knock-out reactions of protons from high-momentum states up to $k = 650\,\mathrm{MeV}$ on ^{12}C, Al, Fe and Au provides a complementary view [roh03]. The analysis demonstrates that there are indeed high-momentum off-shell nucleons present in the ground state of a nucleus. Also the strength distribution over a large range of energies can be observed experimentally.

3.2 Evaluation of Matsubara Sums

The Green's function in T matrix approximation is completely determined by a set of three equations: Dyson's equation (2.19), the ladder equation (2.31), and the expression for the ladder self energy, Eq. (2.30). As a first step towards a numerical solution of this set, the Matsubara summations that appear in Eqs. (2.31) and (2.30) must be performed. The techniques that are applied are similar for both cases and the basic ingredients are the spectral representation of the Green's function and the integration of complex functions along contours in the complex

ω plane as discussed in Section 2.2. Derivations that are similar to those that are discussed below can be found in Refs. [kra86, snl96].
The starting point for the evaluation of the Matsubara sum in the ladder equation is the non-interacting two-particle Green's function, g^0_{II}, that was already reported in Section 2.3 (cf. Eq. (2.32)),

$$g^0_{\mathrm{II}}(k_1, k_2, Z_\Lambda) \;=\; -\frac{1}{\beta}\sum_{\nu=-\infty}^{\infty} g(k_1, z_\nu) g(k_2, Z_\Lambda - z_\nu). \tag{3.17}$$

The spectral representation of the Matsubara Green's functions (3.8) is inserted into Eq. (3.17) and the Matsubara sum is converted into a contour integral [kra86]. This procedure is completely analogous to the transformation of the Matsubara sum that was discussed in connection with the first order self energy in Section 2.2, Eq. (2.23). The contour C encircles all poles of the Fermi function $f(z)$ as shown in Fig. 2.7,

$$g^0_{\mathrm{II}}(k_1, k_2, Z_\Lambda) = \int_{-\infty}^{+\infty} \frac{\mathrm{d}\omega}{2\pi} \int_{-\infty}^{+\infty} \frac{\mathrm{d}\omega'}{2\pi} A(k_1, \omega) A(k_2, \omega') \int_C \frac{\mathrm{d}z}{2\pi \mathrm{i}}\, f(z) F(z, Z_\Lambda), \tag{3.18}$$

where

$$F(z, Z_\Lambda) = \frac{1}{(z - \omega)(Z_\Lambda - z - \omega')}. \tag{3.19}$$

The poles of F are located at $z_1 = \omega$ and $z_2 = Z_\Lambda - \omega'$. The contour C can be deformed to a contour C' in such a way that that only the residues of the product $f(z)F(z, Z_\Lambda)$ at the poles of F contribute. The result is

$$g^0_{\mathrm{II}}(k_1, k_2, Z_\Lambda) = \int_{-\infty}^{+\infty} \frac{\mathrm{d}\omega}{2\pi} \int_{-\infty}^{+\infty} \frac{\mathrm{d}\omega'}{2\pi} A(k_1, \omega) A(k_2, \omega') \frac{1 - f(\omega) - f(\omega')}{Z_\Lambda - \omega - \omega'}. \tag{3.20}$$

Here, the relation $f(Z_\Lambda - \omega) = 1 - f(\omega)$ has been applied, that holds for even integers Λ. The expression for the two-particle propagator, Eq. (3.20), can be continued analytically to slightly complex values $Z = \Omega + \mathrm{i}\eta$ (Ω real). Substituting $\omega' = \Omega' - \omega$, the real and the imaginary part of the retarded propagator are

separated from each other,

$$g^0_{\mathrm{II}}(k_1,k_2,\Omega+\mathrm{i}\eta) \;=\; -\frac{\mathcal{P}}{\pi}\int\limits_{-\infty}^{+\infty}\mathrm{d}\Omega'\,\frac{\operatorname{Im} g^0_{\mathrm{II}}(k_1,k_2,\Omega'+\mathrm{i}\eta)}{\Omega-\Omega'}+\mathrm{i}\operatorname{Im} g^0_{\mathrm{II}}(k_1,k_2,\Omega+\mathrm{i}\eta), \tag{3.21}$$

where

$$\operatorname{Im} g^0_{\mathrm{II}}(k_1,k_2,\Omega+\mathrm{i}\eta) = -\frac{1}{2}\int\limits_{-\infty}^{+\infty}\frac{\mathrm{d}\omega}{2\pi}A(k_1,\omega)A(k_2,\Omega-\omega)[1-f(\omega)-f(\Omega-\omega)]. \tag{3.22}$$

This result is extremely useful since it allows us to obtain $\operatorname{Im} g^0_{\mathrm{II}}$ by carrying out only one ω-integration. Since the spectral functions are sharply peaked and therefore rather difficult to handle numerically, this is essential for the computational treatment. The technical procedure to obtain the complex non-interacting two-particle propagator works as follws: in a first step, $\operatorname{Im} g^0_{\mathrm{II}}$ is calculated for a distribution of Ω, and stored. In a second step, the stored data is used for the evaluation of the principal value integral.

Before the integral in Eq. (3.22) can be computed, a chemical potential μ must be fixed (remember that μ appears in the Fermi function). In principle, Eq. (3.16) must be inverted to find μ. In practice, the density is computed for a number of chemical potentials in a sufficiently wide range, and the final μ is interpolated from the results. The results in this Thesis have been obtained in this way. Alternatively, the chemical potential can be considered as an external variable as described in Ref. [fri03]. In this case, the density will vary in each iteration cycle unless convergence is achieved.
The construction of $\operatorname{Im} g^0_{II}$ is rather delicate, since two sharply peaked spectral functions have to be folded. The careful evaluation of Eq. (3.22) is crucial for the self-consistent procedure. Actually, it is convenient to consider

$$\begin{aligned}\operatorname{Im} g^0_{\mathrm{II}}(k_1,k_2,\tilde{\Omega}+\mathrm{i}\eta) \;=\; & -\frac{1}{2}\int\limits_{-\infty}^{+\infty}\frac{\mathrm{d}\omega}{2\pi}A(k_1,\omega+\epsilon(k_1))A(k_2,\tilde{\Omega}-\epsilon(k_1)-\omega)\\ & \times[1-f(\omega+\epsilon(k_1))-f(\tilde{\Omega}-\epsilon(k_1)-\omega)],\end{aligned} \tag{3.23}$$

where $\tilde{\Omega} = \Omega + \epsilon(k_1) + \epsilon(k_2)$. The on-shell energy $\epsilon(k)$ is defined by

$$\epsilon(k) = \frac{k^2}{2m} + \mathrm{Re}\Sigma(k, \epsilon(k)). \tag{3.24}$$

Note that the peaks of the spectral functions in Eq. (3.23) are located around $\omega = 0$ and $\omega = \Omega$, independent of k_1 and k_2. This simplifies the construction of the integration mesh. Furthermore, in the subsequent angle-averaging procedure, one can take advantage of the fact that $\mathrm{Im}\, g^0_{\mathrm{II}}(k_1, k_2, \tilde{\Omega})$ is peaked around $\Omega = 0$ for all single-particle momenta. This is the quasiparticle peak, and it is formed where the peaks of both one-particle spectral functions coincide in the folding integral, Eq. (3.23).
A sum rule for the two-particle spectral function was given in Ref. [dic99] for zero temperature. For the present case of finite temperature, this sum rule was generalized to

$$-\frac{1}{\pi}\int_{-\infty}^{+\infty} \mathrm{d}\Omega\, \mathrm{Im}\, g^0_{\mathrm{II}}(k_1, k_2, \Omega + \mathrm{i}\eta) = 1 - n(k_1) - n(k_2). \tag{3.25}$$

Since the right hand side is easily computed from the single-particle spectral function, the relation can be used to check the numerical accuracy that is achieved for $\mathrm{Im}\, g^0_{\mathrm{II}}$ after performing the integration in Eq. (3.23). Mesh spacings and integration limits were adjusted such that both sides of Eq. (3.25) do not deviate by more than 1% for single particle momenta up to $k \approx 2000\,\mathrm{MeV}$.
The real part of the two-particle propagator is obtained from the principal value integration according to Eq. (3.21). In principal value integrals, one has to take care that the integration mesh points in the vicinity of the pole at $\Omega' = \Omega$ are arranged symmetrically in order to guarantee a proper cancellation of large contributions with opposite sign. $N_{\tilde{\Omega}} = 120$ mesh points are used for the final mesh and the number of mesh points for either of the momentum variables is $N_k = 70$, which means that $N_{\tilde{\Omega}} \times N_k \times N_k \approx 6 \times 10^5$ integrals have to be evaluated.

The Matsubara summation that appears in the expression for the ladder self energy,

$$\Sigma^L(k, z_\nu) = \frac{1}{\beta}\sum_{\nu'} \int \frac{\mathrm{d}^3k'}{(2\pi)^3} \langle \mathbf{k}\mathbf{k}'|T(z_\nu + z_{\nu'})|\mathbf{k}\mathbf{k}'\rangle_A\, g(k', z_{\nu'}), \tag{3.26}$$

will be performed in the second part of this Section. Again, the spectral representation of the single-particle Green's function is inserted. Since the T matrix shows a dependence upon the Matsubara frequency $z_{\nu'}$, a spectral decomposition of T is required,

$$T(z_\nu + z_{\nu'}) = V - \frac{1}{\pi}\int_{-\infty}^{+\infty} \mathrm{d}\Omega \; \frac{\mathrm{Im}T(\Omega + \mathrm{i}\eta)}{z_\nu + z_{\nu'} - \Omega}. \tag{3.27}$$

This relation follows from the definition of the T matrix and the analytical properties of the Green's function, Eq. (3.8). Using once again the contour C, the ladder self energy can be written as

$$\begin{aligned}\Sigma^L(k, z_\nu) &= \int \frac{\mathrm{d}^3k'}{(2\pi)^3} \langle \mathbf{k}, \mathbf{k}' | \, V \, | \mathbf{k}, \mathbf{k}' \rangle_A \, n(k') + \int_{-\infty}^{+\infty} \frac{\mathrm{d}\Omega}{\pi} \int \frac{\mathrm{d}^3k'}{(2\pi)^3} \int_{-\infty}^{+\infty} \frac{\mathrm{d}\omega'}{2\pi} \\ &\quad \times \langle \mathbf{k}\mathbf{k}' | \mathrm{Im}T(\Omega + \mathrm{i}\eta) | \mathbf{k}\mathbf{k}' \rangle_A \, A(k', \omega') \int_C \frac{\mathrm{d}z}{2\pi\mathrm{i}} \, f(z) G(z, z_\nu), \end{aligned} \tag{3.28}$$

where

$$G(z, z_\nu) = \frac{1}{(z + z_\nu - \Omega)(z - \omega')}. \tag{3.29}$$

The first term in Eq. (3.28) is a *generalized* HF contribution in the sense that it does not only contain HF self energy insertions in the propagating line, but the mean field effects of more complex excitations, which are contained in the full momentum distribution $n(k)$ given by Eq. (3.14). One of the most important contributions for the modification of $n(k)$ with respect to the HF result, the rearrangement term that accounts for the depletion effect in the Bethe-Brueckner-Goldstone theory [jeu76, zuo99], is included in the diagram (k) of Fig. 2.6.
The contour integration in the second term can be performed with the residues of the function G at the poles $z_1 = \omega'$ and $z_2 = \Omega - z_\nu$. The result is

$$\begin{aligned}\Sigma^L(k, z_\nu) &= \Sigma^{HF}(k) - \int_{-\infty}^{+\infty} \frac{\mathrm{d}\Omega}{\pi} \int \frac{\mathrm{d}^3k'}{(2\pi)^3} \int_{-\infty}^{+\infty} \frac{\mathrm{d}\omega'}{2\pi} \, \langle \mathbf{k}\mathbf{k}' | \mathrm{Im}T(\Omega + \mathrm{i}\eta) | \mathbf{k}\mathbf{k}' \rangle_A \\ &\quad \times \frac{A(k', \omega')[f(\omega') + b(\Omega)]}{z_\nu + \omega' - \Omega}. \end{aligned} \tag{3.30}$$

The factor $[f(\omega') + b(\Omega)]$ contains the Bose function, $b(\Omega) = [e^{\beta(\Omega-2\mu)} - 1]^{-1}$ that appears due to the symmetric treatment of hole-hole and particle-particle propagation in the T matrix approach. In the derivation of Eq. (3.30), the relation $f(\Omega - z_\nu) = -b(\Omega)$ was used, which holds for odd integers ν. In order to separate the real part from the imaginary part, one considers the retarded self energy and substitutes $\Omega = \lambda + \omega'$ in Eq. (3.30),

$$\Sigma^L(k, \omega + \mathrm{i}\eta) = \Sigma^{HF}(k) - \frac{\mathcal{P}}{\pi} \int_{-\infty}^{+\infty} \mathrm{d}\lambda \, \frac{\mathrm{Im}\Sigma(k, \lambda + \mathrm{i}\eta)}{\omega - \lambda} + \mathrm{i}\,\mathrm{Im}\Sigma(k, \omega + \mathrm{i}\eta), \quad (3.31)$$

where

$$\begin{aligned} \mathrm{Im}\Sigma^L(k, \omega + \mathrm{i}\eta) \;\; = \;\; & \int \frac{\mathrm{d}^3k'}{(2\pi)^3} \int_{-\infty}^{+\infty} \frac{\mathrm{d}\omega'}{2\pi} \, \langle \mathbf{k}\mathbf{k}' | \mathrm{Im}T(\omega + \omega' + \mathrm{i}\eta) | \mathbf{k}\mathbf{k}' \rangle_A \\ & \times A(k', \omega')[f(\omega') + b(\omega + \omega')]. \end{aligned} \quad (3.32)$$

The Bose function $b(\Omega)$ has a pole at $\Omega = 2\mu$ that is exactly canceled by a node in the imaginary part of the T matrix [alm93, alm96]. As long as the T matrix does not acquire a pole at $\omega + \omega' = 2\mu$, the integrand remains a smooth function of ω'. Such a pole in the T matrix occurs below a critical temperature T_C, a phenomenon which is often referred to as pairing instability. Both the sign change of ImT and the pole formation at low temperatures are discussed in Section 4.2.

3.3 Partial Wave Decomposition

Up to this point, spin-isospin indices have been suppressed according to the convention that was introduced after Eq. (2.1), and the matrix elements of the nuclear potential have been described in the basis of the three momenta $\mathbf{k}$ and $\mathbf{k}'$. However, a coupled two-nucleon basis is much better suited to take advantage of the symmetries of the NN potential. For this purpose, it is at first necessary to construct the transformation matrix between the uncoupled basis, in which the Feynman diagrams are formulated, and the coupled two-particle basis that is described in terms of a maximal set of good quantum numbers of the interacting nucleon pair. Then, an explicit partial wave decomposition of the self energy is carried out.

In the following, single particle angular momentum and isospin quantum numbers are denoted by s and t; the corresponding projection quantum numbers by σ and τ. Two-nucleon quantum numbers and their projections are denoted by capital letters, e.g., J and m_J.

The HF self energy, including the explicit labels of spin and isospin degrees of freedom, can be written as

$$\begin{aligned}\Sigma^{HF}(k) &= \frac{1}{(2s+1)(2t+1)} \sum_{\sigma\tau} \sum_{\sigma'\tau'} \\ &\quad \times \int \frac{\mathrm{d}^3k'}{(2\pi)^3} \langle \mathbf{k}\sigma\tau, \mathbf{k}'\sigma'\tau' | \, V \, |\mathbf{k}\sigma\tau, \mathbf{k}'\sigma'\tau'\rangle_A \, n(k'). \end{aligned} \tag{3.33}$$

Note that only the summations over the internal spin-isospin quantum numbers σ' and τ' were assumed to be implicitly included in the momentum integration. The summations over the external spin-isospin projection quantum numbers σ and τ correspond to an averaging, and one has to normalize by dividing by the degeneracy factors $(2s+1)$ and $(2t+1)$.
As a first step, the anti-symmetric matrix element is expressed in terms of the relative momentum $\mathbf{q} = \frac{1}{2}(\mathbf{k} - \mathbf{k}')$ and the spin and isospin quantum numbers of the pair, S, m_S, T and m_T. The center of mass dependence of the state vectors is suppressed, since the potential matrix elements depend only on the relative momenta,

$$\begin{aligned}|\mathbf{k}\sigma\tau, \mathbf{k}'\sigma'\tau'\rangle_A &= |\mathbf{q}; \sigma\tau, \sigma'\tau'\rangle - |-\mathbf{q}; \sigma'\tau', \sigma\tau\rangle \\ &= \sum_{Sm_S} \sum_{Tm_T} |\mathbf{q}\; Sm_S Tm_T\rangle \, C^{Sm_S}_{s\sigma s'\sigma'} C^{Tm_T}_{t\tau t'\tau'} \\ &\quad - \sum_{Sm_S} \sum_{Tm_T} |-\mathbf{q}\; Sm_S Tm_T\rangle \, C^{Sm_S}_{s'\sigma' s\sigma} C^{Tm_T}_{t'\tau' t\tau}. \end{aligned} \tag{3.34}$$

$C^{Xm_X}_{a\alpha b\beta}$ is the Clebsch-Gordan coefficient that connects the uncoupled basis $|\alpha\beta\rangle$ to the coupled basis $|Xm_X\rangle$ for given angular momenta a and b by means of a unitary transformation.
The next step requires an expansion of the relative wave vector state $\mathbf{q}$ in partial waves. In coordinate space, this expansion reads [jac98]:

$$(2\pi)^{3/2} \langle \mathbf{r}|\mathbf{q}\rangle = e^{\mathrm{i}\mathbf{qr}} = 4\pi \sum_{L=0}^{\infty} \mathrm{i}^L j_L(qr) \sum_{m_L=-L}^{+L} Y_{Lm_L}(\hat{\mathbf{e}}_r) Y^*_{Lm_L}(\hat{\mathbf{e}}_q) \tag{3.35}$$

Here, the j_L represent the spherical Bessel functions and the Y_{Lm_L} are the spherical harmonics. The coordinate representation of the partial wave state is [sak95]

$$\langle \mathbf{r}|q\,Lm_L\rangle = \sqrt{\frac{2}{\pi}}\mathrm{i}^L j_L(qr)Y_{Lm_L}(\hat{\mathbf{e}}_r). \tag{3.36}$$

Comparing Eq. (3.35) and Eq. (3.36), one can identify that the transformation matrix elements are just given by the spherical harmonics,

$$|\mathbf{q}\rangle = \sum_{L=0}^{\infty}\sum_{m_L=-L}^{+L} |q\,Lm_L\rangle\, Y^*_{Lm_L}(\hat{\mathbf{e}}_q). \tag{3.37}$$

Using this decomposition into partial waves, the expansion of the anti-symmetric two-particle state takes the form

$$\begin{aligned}|\mathbf{k}\sigma\tau,\mathbf{k}'\sigma'\tau'\rangle_A &= \sum_{Lm_L}\sum_{Sm_S}\sum_{Tm_T}|q\;Lm_LSm_STm_T\rangle \\ &\quad\times\left[Y^*_{Lm_L}(\hat{\mathbf{e}}_q)C^{Sm_S}_{s\sigma s'\sigma'}C^{Tm_T}_{t\tau t'\tau'} - Y^*_{Lm_L}(-\hat{\mathbf{e}}_q)C^{Sm_S}_{s'\sigma' s\sigma}C^{Tm_T}_{t'\tau' t\tau}\right].\end{aligned} \tag{3.38}$$

The tensor components in the nuclear potential lead to a coupling of partial waves with different orbital angular momentum L; the conserved quantum number is the total angular momentum J. A recoupling of the projection quantum numbers m_L and m_S to J and m_J by a further unitary transformation makes it possible to express the uncoupled two-particle state by a coupled state that is given in terms of J, m_J, T, m_T and S. This is the maximal set of good quantum numbers,

$$\begin{aligned}|\mathbf{k}\sigma\tau,\mathbf{k}'\sigma'\tau'\rangle_A &= \sum_{Jm_J}\sum_{Lm_L}\sum_{Tm_T}\sum_{Sm_S}|q\;LSJm_JTm_T\rangle \\ &\quad\times C^{Jm_J}_{Lm_LSm_S}Y^*_{Lm_L}(\hat{\mathbf{e}}_q)C^{Sm_S}_{s\sigma s'\sigma'}C^{Tm_T}_{t\tau t'\tau'}\left[1-(-1)^{L+S+T}\right].\end{aligned} \tag{3.39}$$

Due to symmetry properties of the Clebsch-Gordan coefficients that are reported, e.g., in Ref. [var88], the anti-symmetry restriction for the coupled state can be expressed by the factor $\left[1-(-1)^{L+S+T}\right]$, which yields either zero or two. This is a selection rule for the partial waves with

$$L+S+T = \text{odd}. \tag{3.40}$$

The full HF self energy can now be obtained by sandwiching the potential between the expressions (3.39) for the state $\langle \mathbf{k}\sigma\tau, \mathbf{k}'\sigma'\tau'|$ and the anti-symmetric state $|\mathbf{k}\sigma\tau, \mathbf{k}'\sigma'\tau'\rangle_A$,

$$\begin{aligned}
\Sigma^{HF}(k) &= \frac{2}{(2s+1)(2t+1)} \sum_{\substack{JST \\ LL'}} \int \frac{\mathrm{d}^3k'}{(2\pi)^3} \langle q| V_{LL'}^{JST} |q\rangle \, n(k') \\
&\times \underbrace{\sum_{m_T} \sum_{\tau\tau'} C^{Tm_T}_{t\tau t'\tau'} C^{Tm_T}_{t\tau t'\tau'}}_{(2T+1)} \sum_{\substack{m_L \\ m_{L'}}} \sum_{\substack{m_S \\ m_{S'}}} \underbrace{\sum_{\sigma\sigma'} C^{Sm_S}_{s\sigma s'\sigma'} C^{Sm_{S'}}_{s\sigma s'\sigma'}}_{\delta_{m_S m_{S'}} \Rightarrow \delta_{m_L m_{L'}}} \\
&\times \sum_{m_J} C^{Jm_J}_{Lm_L Sm_S} C^{Jm_J}_{L'm_{L'} Sm_{S'}} Y_{Lm_L}(\hat{\mathbf{e}}_q) Y^*_{L'm_{L'}}(\hat{\mathbf{e}}_q). \qquad (3.41)
\end{aligned}$$

In Eq. (3.41), the trivial summations over J', $m_{J'}$, S', T' and $m_{T'}$ — the conserved quantum numbers — have already been carried out and the order of the remaining sums in Eq. (3.41) has been arranged in a way that is most convenient for the subsequent steps. The potential matrix elements, $\langle q| V_{LL'}^{JST} |q\rangle$, can be handled in a relative simple way in numerical calculations, because they are a function of only one continuous variables. It is understood that in the ket vector, only partial waves that fulfill condition (3.40) can contribute.

The nuclear interaction does not conserve the angular momentum L, because the tensor components of the NN force lead to a coupling of partial waves with equal parity, $\Pi = (-1)^L$ and $\Delta L = 2$. The best known example for a system with coupled partial waves is the deuteron, which is a ${}^3S_1 - {}^3D_1$ bound neutron-proton state.

Rules for the sums involving Clebsch-Gordan coefficients are given in Ref. [var88]. Note that the factor $\delta_{m_L m_{L'}}$ follows from the conservation of the spin projection m_S and the LS coupling rules $m_S + m_L = m_J$ and $m_{S'} + m_{L'} = m_J$. The remaining summations over m_J, m_L and m_S are carried out in the following steps,

$$\begin{aligned}
\Sigma^{HF}(k) &= \frac{2}{(2s+1)(2t+1)} \sum_{\substack{JST \\ LL'}} (2T+1) \int \frac{\mathrm{d}^3k'}{(2\pi)^3} \langle q| V_{LL'}^{JST} |q\rangle \, n(k') \\
&\times \sum_{m_L} \underbrace{\sum_{\substack{m_J \\ m_S}} C^{Jm_J}_{Lm_L Sm_S} C^{Jm_J}_{L'm_L Sm_S}}_{\frac{(2J+1)}{(2L+1)} \delta_{LL'}} Y_{Lm_L}(\hat{\mathbf{e}}_q) Y^*_{L'm_L}(\hat{\mathbf{e}}_q). \qquad (3.42)
\end{aligned}$$

Using the relation

$$\sum_{m_L} Y_{Lm_L}(\hat{\mathbf{e}}_q) Y^*_{Lm_L}(\hat{\mathbf{e}}_q) = \frac{1}{4\pi}(2L+1), \tag{3.43}$$

and the fact that spin $s = \frac{1}{2}$ and isospin $t = \frac{1}{2}$ for nucleons, one obtains the final result for the HF self energy in a partial wave decomposition

$$\Sigma^{HF}(k) = \frac{1}{8\pi} \sum_{JSTL} (2T+1)(2J+1) \int \frac{\mathrm{d}^3k'}{(2\pi)^3} \langle q | \, V^{JST}_{LL} \, | q \rangle \, n(k'). \tag{3.44}$$

Exactly the same kind of decomposition applies to the imaginary part of the self energy in T matrix approximation:

$$\begin{aligned} \mathrm{Im}\Sigma^L(k, \omega + \mathrm{i}\eta) \;\; = \;\; & \frac{1}{8\pi} \sum_{JSTL} (2T+1)(2J+1) \int \frac{\mathrm{d}^3k'}{(2\pi)^3} \int_{-\infty}^{+\infty} \frac{\mathrm{d}\omega'}{2\pi} A(k', \omega') \\ & \times \left\langle q | \mathrm{Im} T^{JST}_{LL}(P, \omega + \omega' + \mathrm{i}\eta) | q \right\rangle [f(\omega') + b(\omega + \omega')]. \end{aligned} \tag{3.45}$$

Note that there is an explicit dependence upon the center of mass momentum in the partial wave T matrix elements, which will be discussed in the next Section.

3.4 Solution for the T Matrix

The missing link to form a closed system of equations is the solution of the ladder equation for the retarded T matrix. After the Matsubara summations are carried out and the trivial integrations are performed, the ladder equation, Eq. (2.31), turns into a three-dimensional integral equation. A partial wave decomposition can be applied, however, there is a complication due to the explicit dependence of g^0_{II} upon the single particle momenta $k_1 = |\mathbf{P} + \mathbf{k}'|$ and $k_2 = |\mathbf{P} - \mathbf{k}'|$, $\mathbf{P}$ being the center of mass momentum and $\mathbf{k}'$ the relative momentum of the pair in the intermediate state. Obviously, the exact g^0_{II} depends upon the angle θ between the center of mass momentum and the relative momentum, and this leads to a coupling of partial waves with different values of J [sar96, slr99]. In other words, two-particle scattering processes in the nuclear medium do not conserve

the total angular momentum of the pair. The computational difficulties due to this additional coupling can be circumvented by introducing an angle-averaged approximation to g^0_{II},

$$\bar{g}^0_{\rm II}(P,\Omega+\mathrm{i}\eta,k') = \frac{1}{2}\int\limits_{-1}^{+1} \mathrm{d}\cos\theta\ g^0_{\rm II}(|\mathbf{P}+\mathbf{k}'|,|\mathbf{P}-\mathbf{k}'|,\Omega+\mathrm{i}\eta). \tag{3.46}$$

Replacing the exact propagator g^0_{II} by the angle-approximated $\bar{g}^0_{II}$, the ladder equation for the retarded T matrix can be written as a one-dimensional integral equation for each allowed combination of the total angular momentum J, spin S and isospin T,

$$\begin{aligned}\left\langle q|T^{JST}_{LL'}(P,\Omega+\mathrm{i}\eta)|q'\right\rangle &= \left\langle q|V^{JST}_{LL'}|q'\right\rangle + \sum_{L''}\int\limits_0^\infty \frac{\mathrm{d}k'\,k'^2}{(2\pi)^3}\left\langle q|V^{JST}_{LL''}|k'\right\rangle \\ &\quad\times\bar{g}^0_{\rm II}(P,\Omega+\mathrm{i}\eta,k')\left\langle k'|T^{JST}_{L''L'}(P,\Omega+\mathrm{i}\eta)|q'\right\rangle . \end{aligned}\tag{3.47}$$

Only for the coupled partial waves, a summation over L'' is required. The maximum number of coupled partial waves is $N_c = 2$. All possible channels up to $J = 2$ are listed in Table 3.1.
There have been efforts to estimate the effect of the angle-averaging procedure on the self energy or the total binding energy of the system in Brueckner quasiparticle type calculations, and only moderate deviations from the exact result have been found [sar96, slr99, suz00, fri02]. Beyond the quasiparticle approximation, no calculation without angle-averaging approximation has been published.

Eq. (3.47) is solved by a numerical matrix inversion technique similar to the one described by Haftel and Tabakin in Ref. [haf70]. However, since the dressed two-particle $\bar{g}^0_{\rm II}$ is not divergent, a pole subtraction is not necessary. As a first step, the integration variable k' is discretized, so that the integral is written as a sum,

$$\int\limits_0^\infty \mathrm{d}k'\ h(k') \quad\longrightarrow\quad \sum_{n=1}^{N_I} u_n\, h(k_n). \tag{3.48}$$

In this expression, $h(k_n)$ is the integrand of Eq. (3.47) at the mesh point k_n and u_n is the corresponding integration weight. N_I is the number of integration mesh points and has to be adjusted in such a way that the desired accuracy is achieved.

J	Π	S	T	term symbol	N_c
0	+	0	1	${}^1S_0$	1
	-	1	1	${}^3P_0$	1
1	+	1	0	${}^3S_1 - {}^3D_1$	2
	-	1	1	${}^3P_1$	1
	-	0	0	${}^1P_1$	1
2	+	1	0	${}^3D_2$	1
	+	0	1	${}^1D_2$	1
	-	1	1	${}^3P_2 - {}^3F_2$	2

Table 3.1: Quantum numbers and spectroscopic terms of all channels up to $J = 2$ under the antisymmetry constraint $L + S + T = odd$. Π is the parity of the two-nucleon state, $\Pi = (-1)^L$, and N_c is the number of coupled orbital angular momenta.

In order to reformulate the problem as a matrix equation, the momentum variable q needs to be discretized, too, and the same mesh points must be used. For given values of the total pair momentum P, the total pair energy Ω and the initial relative momentum q, the ladder equation can be written as

$$\begin{aligned}\left\langle k_m|V^{JST}_{LL'}|q\right\rangle &= \sum_{L''}\sum_{n=1}^{N_I}\left[\delta_{mn}\delta_{LL''} - \left\langle k_m|V^{JST}_{LL''}|k_n\right\rangle \bar{g}^0_{\Pi}(P,\Omega+\mathrm{i}\eta,k_n)\,u_n\,k_n^2\right] \\ &\quad\times\left\langle k_n|T^{JST}_{L''L'}(P,\Omega+\mathrm{i}\eta)|q\right\rangle . \qquad (3.49)\end{aligned}$$

The superfluous prime has been omitted. The structure of this equation can be further simplified by introducing multi-indices,

$$N \equiv (n, L'') \quad \text{and} \quad M \equiv (m, L), \qquad (3.50)$$

which are used to define two vectors with N_cN_I components and a complex quadratic $N_cN_I \times N_cN_I$ matrix,

$$\begin{aligned}\mathbb{V}^\alpha_M(q) &= \left\langle k_m|V^{JST}_{LL'}|q\right\rangle \\ \mathbb{T}^\alpha_N(P,\Omega,q) &= \left\langle k_n|T^{JST}_{L''L'}(P,\Omega+\mathrm{i}\eta)|q\right\rangle \\ \mathbb{M}^\alpha_{MN}(P,\Omega) &= \left[\delta_{mn}\delta_{LL''} - \left\langle k_m|V^{JST}_{LL''}|k_n\right\rangle \bar{g}^0_{\Pi}(P,\Omega+\mathrm{i}\eta,k_n)\,u_n\,k_n^2\right]. \qquad (3.51)\end{aligned}$$

The index α denotes the three-tuple (J, S, T). With these abbreviations, the matrix structure of the ladder equation becomes obvious,

$$\mathbb{V}^{\alpha}_{M}(q) = \sum_{N=1}^{N_c \times N_I} \mathbb{M}^{\alpha}_{MN}(P,\Omega)\, \mathbb{T}^{\alpha}_{N}(P,\Omega,q). \tag{3.52}$$

Eq. (3.52) can be solved separately in each channel α by inversion of the matrix $\mathbb{M}$,

$$\mathbb{T}^{\alpha}_{N}(P,\Omega,q) = \sum_{M=1}^{N_c \times N_I} [\mathbb{M}^{\alpha^{-1}}(P,\Omega)]_{MN}\, \mathbb{V}^{\alpha}_{M}(q). \tag{3.53}$$

Finally, the desired diagonal T matrix elements $\left\langle q|\mathrm{Im}\, T^{JST}_{LL}(P,\Omega+\mathrm{i}\eta)|q\right\rangle$ are obtained by interpolation.

The solution of the ladder equation for the T matrix elements is a quite time consuming task in the numerical treatment. The numerical cost for the matrix inversion operation is proportional to the square of the number of integration mesh points, N_I. Therefore, some effort should be spend to keep this number as small as possible. On the other hand, an accurate sampling of the regions around k_0, the position of the quasiparticle peak of the two-particle propagator, is crucial for convergence. Of course, the high momentum region needs to be well sampled, too. To achieve both aims, the integration range is divided into two intervals by introducing a momentum k_X. It is required that k_0 is located in the low momentum interval $[0, k_X]$, so that the location of k_X depends on the position of the quasiparticle peak. Close to k_0, the integrand varies rapidly, but it does not diverge as in a quasiparticle description (cf. Eq. (3.57) in Section 3.5 at the end of this Chapter). Various bins of Gauss-Legendre mesh points are used in the interval $[0, k_X]$. In the vicinity of the quasiparticle peak, a high density of mesh points is applied, and, like in the case of the dispersion integral for $\mathrm{Re}\, g^0_{\mathrm{II}}$, they are distributed symmetrically on both sides, to favor a proper cancellation of contributions with opposite sign. The second interval defines the high momentum region. To achieve a reasonable sampling in this case, the k-interval $[k_X, \infty]$ is mapped to a finite x-interval $[X, 1]$ with $0 < X < 1$, using the transformation

$$k_j = c \tan\left(\frac{\pi}{2} x_j\right), \tag{3.54}$$

where x_j are Gauss-Legendre mesh points within the finite x-interval. The constant c needs to be chosen such that an adequate sampling is guaranteed up to a

momentum region where the potential is suppressed by the cutoff. Above k_X, the Gaussian integration weights w_j must be transformed according to

$$u_j = c\,\frac{\frac{\pi}{2}w_j}{\cos^2\left(\frac{\pi}{2}x_j\right)}. \tag{3.55}$$

$N_I = 50$ integration points are used in the numerical calculation. The T matrix is computed on a three-dimensional mesh in terms of the center of mass momentum P, the total pair energy Ω and the relative momentum of the pair q. The energy mesh contains $N_\Omega = 80$ points, while $N_P = N_q = 30$. The matrix does not depend on the relative momentum q, hence, the computer routine has to carry out $N_{MI} = N_\Omega \times N_P \times N_{JST}$ matrix inversion operations, where N_{JST} is the number of partial waves that contribute. If partial waves up to a total angular momentum of $J = 2$ are included, $N_{JST} = 8$ (cf. Table 3.1) and $N_{MI} \approx 20000$.

The methods that were discussed in this Chapter provide all ingredients for the self-consistent determination of an unknown function of two variables — the spectral function $A(k,\omega)$: in Section 3.2, it was explained how the the two-particle propagator must be constructed from the spectral function. The present Section was devoted to the computation of the T matrix elements, which, in turn, are used to calculate the self energy as reported in Section 3.2. A new spectral function is then obtained from the self energy according to Eq. (3.11) in Section 3.1.
Before the numerical procedure that was developed to find a solution for the self-consistent Green's function is discussed more closely in Section 4.1, two different approximations to the full SCGF approach will be outlined below.

3.5 Quasiparticle Approximations

In the final Section of Chapter 3, two distinct approximative schemes are discussed. In both schemes, the non-trivial spectral functions are replaced by the quasiparticle expression, Eq. (3.12), that was given in Section 3.1,

$$A(k,\omega) = 2\pi\,\delta(\omega - \epsilon(k)).$$

The Dirac function is peaked at the quasiparticle energy and introduces an energy momentum relation to the model. The quasiparticle energy spectrum $\epsilon(k)$ is

determined from the following on-shell condition

$$\epsilon(k) = \frac{k^2}{2m} + \mathrm{Re}\Sigma(k, \epsilon(k)). \tag{3.56}$$

In addition to the kinetic energy, this expression includes the real part of the on-shell self energy, which is interpreted as a momentum dependent quasiparticle potential. In a quasiparticle scheme, self-consistency is established on the level of the quasiparticle spectrum (3.56), which is a function of only one variable. All integrations over ω that contain a spectral function in the integrand become trivial in the quasiparticle picture and can be carried out immediately.

The first approximation is called *quasiparticle* or QPGF scheme in the following. This scheme is an approximation in the spirit of the Green's functions formalism in the sense that the self energy or the propagator can be displayed as a set of Feynman diagrams. It is however not fully consistent, since the off-shell structure of the self energy that is introduced by the ladder diagrams is not refeeded into the single-particle Green's functions in the ladder equation. Self-energy diagrams with self energy insertions, such as the diagrams (k), (l) and (m) in Fig. 2.6 are therefore neglected. In the QPGF picture, the retarded, angle-averaged two-particle propagator takes the simple form

$$\bar{g}_{\mathrm{II}}^{QP}(P, \Omega + \mathrm{i}\eta, q) = \left\langle \frac{1 - f(\epsilon(k_1)) - f(\epsilon(k_2))}{\Omega - \epsilon(k_1) + \epsilon(k_2) + \mathrm{i}\eta} \right\rangle_\theta . \tag{3.57}$$

Note that a zero can appear in the denominator. The corresponding pole requires the application of slightly different techniques than in the case of the dressed propagator. They are discussed Refs. [haf70, ter91, dew00].
The imaginary part of the self energy in ladder approximation is given by

$$\begin{aligned} \mathrm{Im}\Sigma^{QP}(k, \omega + \mathrm{i}\eta) &= \frac{1}{8\pi} \sum_{JSTL} (2T+1)(2J+1) \int \frac{\mathrm{d}^3 k'}{(2\pi)^3} [f(\epsilon(k')) + b(\omega + \epsilon(k')] \\ &\quad \times \left\langle q | \mathrm{Im} T_{LL}^{JST}(P, \omega + \epsilon(k') + \mathrm{i}\eta) | q \right\rangle . \end{aligned} \tag{3.58}$$

The real part of the self energy is obtained from a dispersion relation, as it was described in Section 3.2, and therefore, the full off-shell structure of $\mathrm{Im}\,\Sigma$ must be computed. The QPGF off-shell self energy can be used to compute a non-trivial spectral function in the complete momentum-energy plane. To preclude misunderstandings, it should be emphasized once again that such a QPGF spectral function

cannot be characterized as self-consistent, since only the on-shell information is constrained in a quasiparticle description.
Successful numerical calculations of the QPGF type have been performed by various groups since the late 80's. A comprehensive and very clear description of the method at zero temperature can be found, e.g., in Ref. [ram88]. A selection of other useful references may be given by [ram89, dic92, von93, snl96].

A second approximation of the quasiparticle type is the well-known two hole-line expansion or Brueckner-Hartree-Fock (BHF) scheme. The BHF method was developed in the 50's by Brueckner and collaborators [bru54, bru58] and has been successfully applied in many problems since then. Ref. [day67] is a pedagogical review article on the application of Brueckner theory to nuclear matter.
Strictly speaking, this approximation is not in line with the principles of Green's functions theory, since physical quantities are not expanded in terms of fully-fledged Green's functions. Instead, all propagators are split into two terms proportional to $g^<$ and $g^>$, respectively, and in this way, a time ordering is introduced into the diagrammatical language. Goldstone showed that there exists an expansion of the ground state energy of the system in terms of the time ordered graphs [gol57], which is equivalent to the perturbation expansion of the Green's function [fet71]. A similar expansion for the Gibbs potential of a quantum many-body system was formulated by Bloch and De Dominicis [blo58].
At low densities, the phase space for the forward propagating particles is much larger than the phase space for the holes. Since each internal line is associated with an integration over the respective phase space, it is to some extent justified to retain only those diagrams with a minimal number of hole lines in the expansion of the self energy. And these diagrams are just the self energy diagrams that are composed of ladders of the forward propagating particle-particle contributions and a single hole line that connects two of the four external points.
It is instructive to reformulate Eq. (3.20) in order to see that the dressed, non-interacting two-particle propagator includes both forward and backward contributions,

$$g^0_{\mathrm{II}}(k_1,k_2,\Omega+\mathrm{i}\eta) = \int\limits_{-\infty}^{+\infty}\frac{\mathrm{d}\omega}{2\pi}\int\limits_{-\infty}^{+\infty}\frac{\mathrm{d}\omega'}{2\pi}\frac{g^>(k_1,\omega)\,g^>(k_2,\omega') - g^<(k_1,\omega)\,g^<(k_2,\omega')}{\Omega-\omega-\omega'+\mathrm{i}\eta}. \tag{3.59}$$

If the second term is neglected and quasiparticle spectral functions are assumed,

the particle-particle propagator reduces to the BHF form,

$$\bar{g}_{\mathrm{II}}^{BHF}(P,\Omega+\mathrm{i}\eta,q)=\left\langle\frac{[1-f(\epsilon(k_1))][1-f(\epsilon(k_2))]}{\Omega-\epsilon(k_1)+\epsilon(k_2)+\mathrm{i}\eta}\right\rangle_{\theta}. \tag{3.60}$$

The nominator of Eq. (3.60) is the Pauli operator of a system of quasiparticle in thermodynamic equilibrium, which projects onto two-particle intermediate states. In the zero temperature case, the nominator reduces to $\Theta(k_1-k_F)\,\Theta(k_2-k_F)$. In the framework of the BHF theory, the quasiparticle energy $\epsilon(k)$ is determined by Eq. (3.56) only for the hole states, according to the theorem of Bethe, Brandow and Petschek [bet63]. For the particle states, various prescriptions for $\epsilon(k)$ are in use [son98]. The conventional choice is to ignore the self energy contributions for the particle states completely. The energies for these states are approximated by the kinetic energy only. This choice results in a gap in the spectrum between the holes and the particles, which is why it is also called gap choice. A more natural prescription from the point of view of the theory of Green's functions was suggested in Ref. [jeu76]. In this so-called continuous choice, Eq. (3.56) is used for both particle and hole states, which leads to a continuous spectrum. For the BHF calculations in this Thesis, the continuous choice is adopted.
The ladder equation with the two-particle propagator (3.60),

$$\begin{aligned}\left\langle q|G_{LL'}^{JST}(P,\Omega+\mathrm{i}\eta)|q'\right\rangle &= \left\langle q|V_{LL'}^{JST}|q'\right\rangle+\sum_{L''}\int_0^\infty\frac{\mathrm{d}k'\,k'^2}{(2\pi)^3}\left\langle q|V_{LL''}^{JST}|k'\right\rangle\\ &\quad\times\bar{g}_{\mathrm{II}}^{BHF}(P,\Omega+\mathrm{i}\eta,k')\left\langle k'|G_{L''L'}^{JST}(P,\Omega+\mathrm{i}\eta)|q'\right\rangle,\end{aligned} \tag{3.61}$$

is usually referred to as Bethe-Goldstone equation, and the solution is called the Brueckner G matrix. Since only particle pairs propagate in the intermediate states, the time ordering requires that the BHF self energy graphs must be closed by hole line. Real and imaginary part of the BHF self energy are then given by

$$\begin{aligned}\Sigma^{BHF}(k,\epsilon(k)) &= \frac{1}{8\pi}\sum_{JSTL}(2T+1)(2J+1)\\ &\quad\times\int\frac{\mathrm{d}^3k'}{(2\pi)^3}\left\langle q\right|G_{LL}^{JST}(P,\epsilon(k)+\epsilon(k')+\mathrm{i}\eta)\left|q\right\rangle f(\epsilon(k')).\end{aligned} \tag{3.62}$$

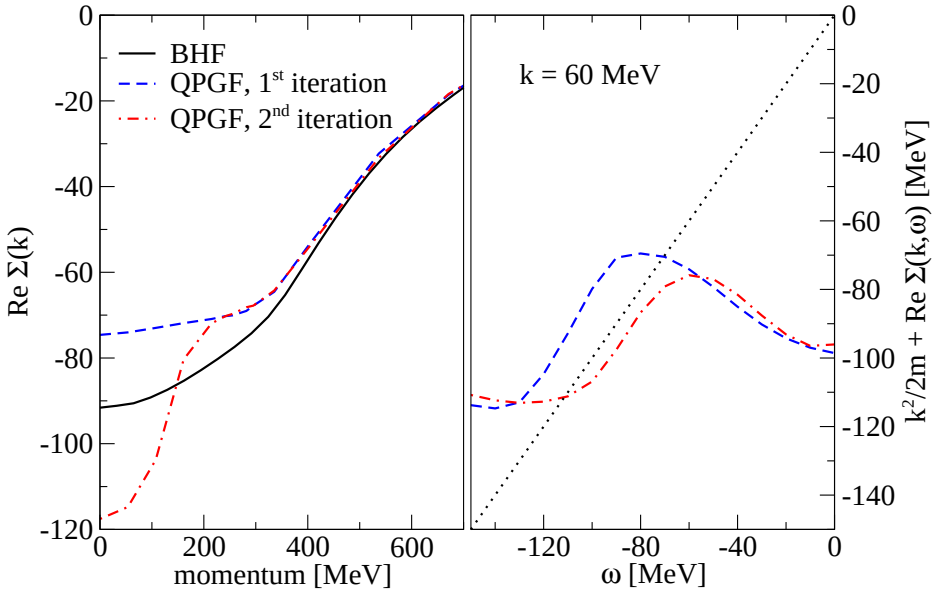

Figure 3.3: *Convergence problems in the QPGF scheme. Left panel: BHF single-particle potential (solid line), real part of the on-shell QPGF self energy after one iteration cycle (dashed line) and after two iteration cycles (dash-dotted line). Right panel: Graphical solution of Eq. (3.56), using the off-shell QPGF self energy. The parameters are* $T = 5\,MeV$ *and* $\rho = 0.17\,fm^{-3}$.

To find the BHF quasiparticle spectrum, Eqs. (3.61), (3.62) and (3.56) need to be solved self-consistently. Unlike for the quasiparticle scheme, it is sufficient to know the on-shell values of the self energy.

The two quasiparticle schemes that were discussed in this Sections are usually solved by iteration. Convergence is achieved as soon as the single-particle spectrum does not change any more. Results of the QPGF and the BHF scheme will be compared to those of the full SCGF approximation in Chapter 4. However, a problem concerning the convergence properties of the QPGF truncation must be mentioned. The left panel of Fig. 3.3 shows the self-consistent BHF on-shell self energy and the first two iterations of the same quantity in the QPGF scheme. The BHF self energy plus the kinetic energy was used as an input spectrum for the QPGF calculation. While the first iteration (dashed line) yields a repulsive effect of nearly 20 MeV with respect to the BHF result (solid line) for the states with low

momenta, the second iteration (dash-dotted line) displays an attraction of more than 40 MeV compared to the first iteration. Further iterations lead to a strange pattern, where $\mathrm{Re}\,\Sigma(0, \epsilon(0))$ seems to jump between two solutions. Obviously, the calculation does not converge for momenta below $k \approx 200\,\mathrm{MeV}$. This curious effect can be understood by a graphical solution of the on-shell condition, Eq. (3.56). For a momentum of $k = 60\,\mathrm{MeV}$, the right hand side (kinetic energy plus real off-shell self energy) is plotted in the right panel of Fig. 3.3. The dotted line is the left hand side. The on-shell solution is given by the intersection point. Using the repulsive spectrum of the first iteration as an input for the second iteration, the dispersive structure in the off-shell self energy is shifted in the positive direction, and this leads to a drastic shift of the intersection point from $\omega \approx -70\,\mathrm{MeV}$ to $\omega \approx -110\,\mathrm{MeV}$.

The same convergence problem was found by Dewulf in Ref. [dew00] using the Reid 93 interaction. Quasiparticle calculations with separable potentials did not show this feature, e.g. [snl96].

Since self-consistent spectra cannot be obtained, the QPGF results that are presented in the following, are first iteration results, using a BHF input spectrum.

Chapter 4

Results

4.1 Iterative Scheme

In Chapter 3, the closed set of equations that determine the Green's function was cast into a form that is ready for a numerical treatment. A main part of the work on this Thesis was spend on the development of a computer code that is able to find a self-consistent solution to the problem. Before the results will be presented in the subsequent Sections, some general remarks on the structure of the code and the way the iteration scheme works will be made.
In Fig. 4.1, the mutual dependence of the various physical quantities is illustrated. The spectral function A, the chemical potential μ, the non-interacting two-particle propagator g^0_{II}, the T matrix and the self energy Σ must be determined in a consistent way from the nuclear two-body potential V, and for a given density ρ and a given inverse temperature β (the dependence on β is not displayed in Fig. 4.1). A solution must be consistent in the sense that, e.g., the spectral function that enters the computation of the self energy in Eq. (3.45) should in turn be reproduced by this self energy in Eq. (3.11) The natural way to tackle such a problem is to assume an initial set of functions that defines the problem completely. Starting with this input, the problem is solved by iteration. Each step in Fig. 4.1 is cycled several times, in the order given in Tab. 4.1, until the output and the input are reasonably close. Depending on the initial guess, around $6-12$ iteration cycles are necessary to establish convergence. To illustrate this process, two numbers that depend on a specific momentum k and a specific energy ω of the particle, namely

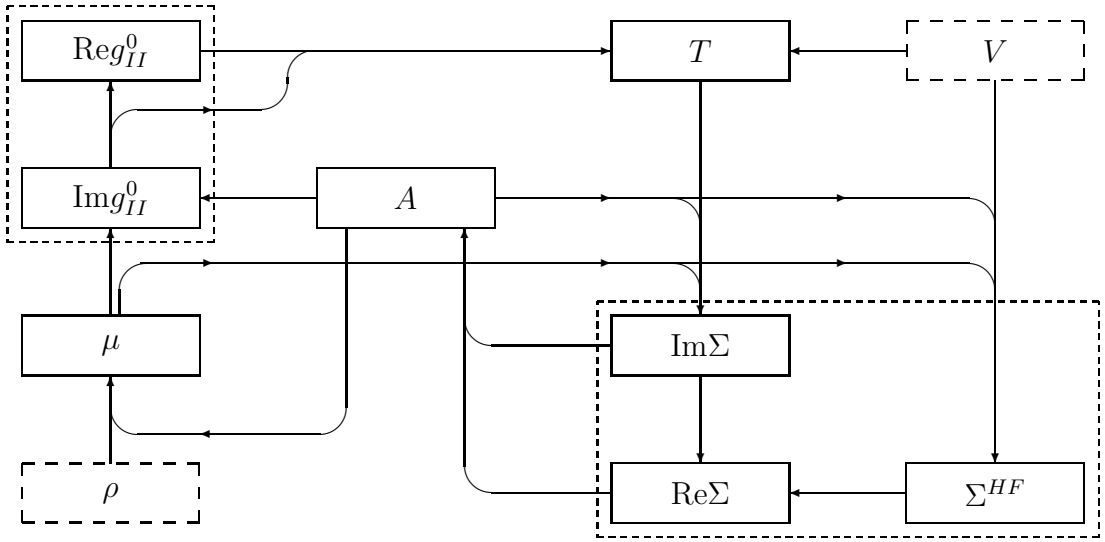

Figure 4.1: *Graphical representation of the coupled system that has to be solved self-consistently. The density ρ and the nuclear potential V are external quantities (long-dashed boxes). The central quantity is the spectral function A, that enters in the computation of the two-particle propagator g^0_{II} and the self energy Σ (large short-dashed boxes). The angle averaging of g^0_{II} is not displayed.*

the real and the imaginary part of the on-shell self-energy at zero momentum and close to the Fermi surface, and two characteristic global numbers, the chemical potential, and the internal energy per particle were monitored during the iteration procedure. They are displayed in Fig. 4.2 and show an excellent convergence behavior. After 7 iteration cycles, for instance, the deviation of μ with respect to the final value after 10 cycles is already less than 0.05%.

For the first calculation that was conducted with the computer code, a spectral function that was obtained from an quasiparticle off-shell self energy was used as an initial guess. Once the first self-consistent result had been obtained, it was found to be most convenient to use it, in turn, as an initial guess for the next calculation at slightly different temperatures and densities. In this way, it is possible to explore a wide range of densities and temperatures with an initial spectral function that is always close to the final result, so that quick convergence is guaranteed.

The computer code for the self-consistent solution of the problem was written in

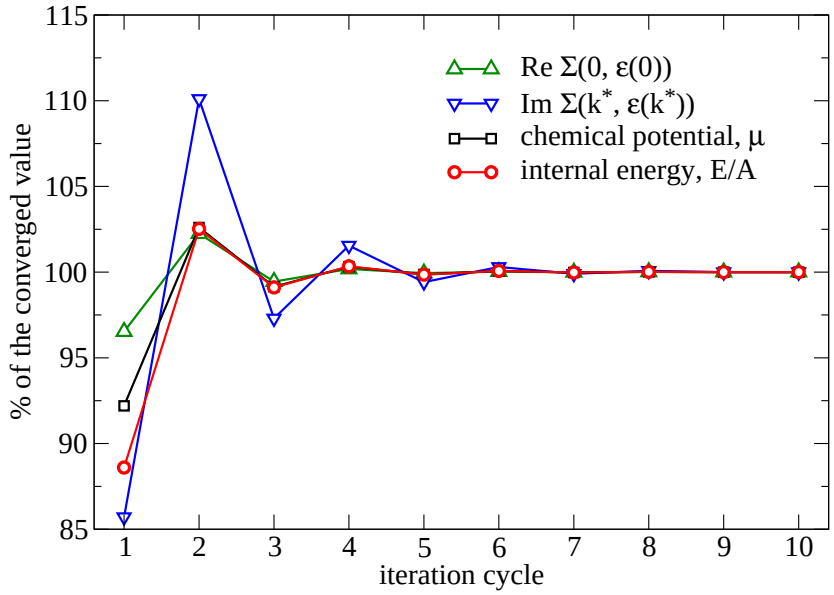

Figure 4.2: *Typical convergence characteristics of the iteration scheme. Four quantities are monitored for 10 iteration cycles. After about 6 cycles, convergence is achieved. The parameters are* $T = 7\,MeV$ *and* $\rho = 0.16\,fm^{-3}$.

MATLAB, which has proven to be an ideal tool to handle large multi-dimensional fields numerically. On a normal workstation, the CPU time for one iteration cycle is about 5 h, so that less than 2 days are needed for a converged calculation at a given density and a given temperature.

It must be emphasized that, with the applied method, self-consistency cannot be achieved in all temperature and density regions for numerical reasons. The system becomes more and more degenerate the higher the density and the lower the temperature is. Thus, the number of mesh points that are necessary to sample the pronounced structures due to the sharpening of the Fermi edge increases strongly. For instance, the width of the spectral functions tends to zero for $T \to 0$, so that the numerical integration in Eq. (3.23) and the subsequent angle-averaging procedure become too tedious and time consuming below a temperature of $T = 3\,\mathrm{MeV}$ (at a density in the range of the central density of ^{208}Pb).

In the following Sections, the self-consistent results that have been obtained within the SCGF scheme are presented and discussed. Most of the calculations in this

	μ	$\mathrm{Im}\, g^0_{II}$	$\mathrm{Re}\, g^0_{II}$	$\bar{g}^0_{II}$	$\mathrm{Im}\, T$	Σ^{HF}	$\mathrm{Im}\, \Sigma^L$	$\mathrm{Re}\, \Sigma^L$	A
Step	1	2	3	4	5	6	7	8	9
Eq.	(3.16)	(3.22)	(3.21)	(3.46)	(3.47)	(3.44)	(3.45)	(3.31)	(3.11)

Table 4.1: Sequence of the numerical steps that are carried out in a single iteration cycle. The numbers of the corresponding equations are given in the last row.

Thesis have been performed using the CDBONN potential [mac96]. In the cases where another potential was used, this is indicated. Numerical checks revealed that, for the imaginary part of the self energy, it is sufficient to include partial waves up to an total angular momentum of $J = 2$ for the pair of colliding nucleons. The generalized HF contribution contains partial waves up to $J = 9$. The T matrix is discussed in Section 4.2. Section 4.3 is devoted to the self energy. An extrapolation method is proposed to explore the temperature region below $T = 3\,\mathrm{MeV}$. Self-consistent spectral functions and momentum distributions are presented in Section 4.4 and Section 4.5, respectively. Finally, the saturation properties of nuclear matter are discussed in Section 4.6.

4.2 The T Matrix and Signals of Pairing

The discussion of the results for the thermodynamical T matrix will be guided by two major points. As a first item, it is useful to illustrate and explain its structure. Many features of the T matrix are imprinted by the structure of g^0_{II}. The off-shell behavior of T for pair energies $\Omega \to -\infty$ and the fingerprints of the phase space restrictions imposed by the Pauli principle will be discussed. Qualitative distinctions between the quasiparticle scheme and the SCGF solution can be pinpointed. Secondly, at low temperatures, the effects of the NN pairing and the formation of bound states become apparent in the T matrix [sch90, von90]. The Green's functions formalism that was outlined in the previous Chapters is not capable to describe phenomena that are associated with the transition to a superfluid system. However, precursor effects that indicate a possible phase transition in a tempera-

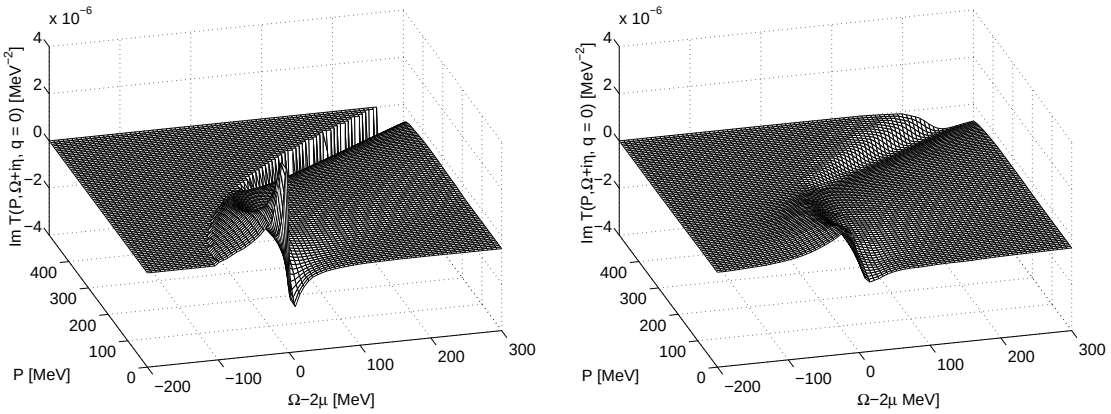

QPGF scheme SCGF scheme

Figure 4.3: *Comparison between the quasiparticle approach (left panel) and the full scheme (right panel) on the level of the T-matrix. The dependence upon the center of mass momentum P and the pair energy Ω is displayed, while the relative pair momentum q is set to zero. The density is $\rho = 0.16\,fm^{-3}$ and the temperature is chosen to be $T = 5\,MeV$.*

ture regime that cannot be covered in this work are visible in the structure of the T matrix and will be discussed.

In Fig. 4.3, the imaginary part of the thermodynamic T matrix in the SCGF scheme, and the same quantity — obtained with a non-trivial g^0_{II} obtained in the full SCGF scheme — are compared. The calculations were performed at a density of $\rho = 0.16\,\mathrm{fm}^{-1}$. This number corresponds to the so-called saturation density ρ_0 of nuclear matter and it can be derived from an extrapolation of electron scattering data on heavy nuclei. The T matrix depends on three variables, P, Ω and q, but since only two of them can be displayed in a three-dimensional plot, the relative momentum of the pair, q, is set to zero. In the left panel of Fig. 4.3, it can be observed that the quasiparticle T matrix has no imaginary part for pair energies Ω below a sharp line in the $\Omega - P$ plane. This property of the quasiparticle ansatz will be explained in the following. Using the identity (3.9), and the quasiparticle propagator that was given in Section 3.5, the right hand side of the ladder equation, Eq. (3.47), can be split into two pieces. The second one includes a Dirac

function,

$$\left\langle q|T^{JST}_{LL'}(P,\Omega+\mathrm{i}\eta)|q'\right\rangle = [\cdots] - \mathrm{i}\pi \sum_{L''} \int_0^\infty \frac{\mathrm{d}k'\, k'^2}{(2\pi)^3}\, \delta(\Omega - \langle \epsilon(k_1)+\epsilon(k_2)\rangle_\theta) \times \left\langle q|V^{JST}_{LL''}|k'\right\rangle \langle [1-f(\epsilon(k_1))-f(\epsilon(k_2))]\rangle_\theta \left\langle k'|T^{JST}_{L''L'}(P,\Omega+\mathrm{i}\eta)|q'\right\rangle . \quad (4.1)$$

Note that k_1 and k_2 were taken as a shorthand notation for $|\mathbf{P}+\mathbf{k}'|$ and $|\mathbf{P}-\mathbf{k}'|$. The quasiparticle T matrix can have an imaginary part only if the argument of the Dirac function — the denominator of the quasiparticle propagator — has a node at any point within the integration range, i.e., only if there is a combination of P, Ω and any value of the integration variable k', such that

$$\Omega = \langle \epsilon(|\mathbf{P}+\mathbf{k}'|) + \epsilon(|\mathbf{P}-\mathbf{k}'|)\rangle_\theta . \quad (4.2)$$

A quite reasonable assumption is an effective mass parameterization of the quasiparticle energy spectrum,

$$\epsilon(k) = \frac{k^2}{2m^*} + U_0. \quad (4.3)$$

This analytic expression will be adopted in the following discussion for the sake of simplicity. The parameters are the effective mass, m^*, and the potential depth, U_0. For a fixed center of mass momentum P, it follows that the condition for a vanishing imaginary part is

$$\Omega < 2\epsilon(P). \quad (4.4)$$

The edge in the left panel of Fig. 4.3 is therefore given by the threshold energy that can be approximated by $\Omega_{min}(P) = 2\epsilon(P)$. In the full SCGF scheme, where off-shell propagation is taken into account, no sharp signature can be observed and the imaginary part extends to much higher negative energy values. This is an interesting point, because the properties of the negative energy tail of $\mathrm{Im}\, T$ are reflected in the negative energy tail of the spectral function (cf. Section 4.4).
Some details of the structure of the T matrix are closely related to the phase space restrictions imposed by the fermionic nature of the colliding nucleons. This can be studied most easily in the quasiparticle picture, too. Using again the quadratic parameterization of the quasiparticle spectrum, Eq. (4.3), the pole of the two-particle propagator can be written as an analytic function in terms of Ω and P,

$$k_0 = \sqrt{m^*[\Omega - \Omega_{min}(P)]}. \quad (4.5)$$

This expression is only reasonable above the threshold energy $\Omega_{min}(P)$, which is given by

$$\Omega_{min}(P) = \frac{P^2}{m^*} + 2U_0. \tag{4.6}$$

Taking advantage of the Dirac function, the integral in Eq. (4.1) can be evaluated,

$$\begin{aligned}\left\langle q|T^{JST}_{LL'}(P,\Omega+\mathrm{i}\eta)|q'\right\rangle = [\cdots] - \mathrm{i}\pi\frac{m^*k_0}{(2\pi)^3}\sum_{L''}\left\langle q|V^{JST}_{LL''}|k_0\right\rangle \\ \times\left\langle k_0|T^{JST}_{L''L'}(P,\Omega+\mathrm{i}\eta)|q'\right\rangle \underbrace{\langle[1-f(\epsilon(|\mathbf{P}+\mathbf{k}_0|))-f(\epsilon(|\mathbf{P}+\mathbf{k}_0|))]\rangle_\theta}_{\text{Pauli factor}}.\end{aligned} \tag{4.7}$$

It can be shown that the imaginary part of the T matrix is proportional to the Pauli factor in Eq. (4.7). This factor is a function of Ω and P. It is shown in Fig. 4.4 and should be related with the left panel of Fig. 4.3, where the same chemical potential and the same parameter ranges for Ω and P were assumed. In the region that is defined by $\Omega < \Omega_{min}(P)$, the value of the Pauli factor has been set to zero arbitrarily. This region is irrelevant for the the study of the fingerprints of the Pauli factor in the T matrix, since there, the imaginary part of the T matrix is zero because the two-particle propagator has no pole, as was pointed out in connection with Eq. (4.5). In the region defined by $\Omega > \Omega_{min}(P)$, the shape of ImT shows clear signatures of the Pauli phase space factor. The absolute values of the gradients in both plots are similar in major regions of the $\Omega - P$ plane. The stretched hump in the vicinity of the deep valley, e.g., reflects the reduction of the Pauli factor in this kinematic region. Also the sign change of ImT at $\Omega = 2\mu$ is a consequence of the sign change of the Pauli factor. Note that for arbitrary energy variables ω and ω', the Pauli operator can be written as [sch90]:

$$1 - f(\omega) - f(\omega') = b^{-1}(\omega+\omega')f(\omega)f(\omega'). \tag{4.8}$$

By writing the Pauli factor in this way, it becomes obvious how the apparent divergence of the integrand of Eq. (3.32) at $\Omega = 2\mu$, being introduced by the Bose function, is exactly canceled by the inverse of this function.
It is instructive to study the onset of pairing effects in the T matrix of the nuclear many-body system. Under a broad range of physical conditions, charged fermion many-body systems undergo a phase transition to a superconducting state below a critical temperature T_C. The new state possesses different symmetry properties

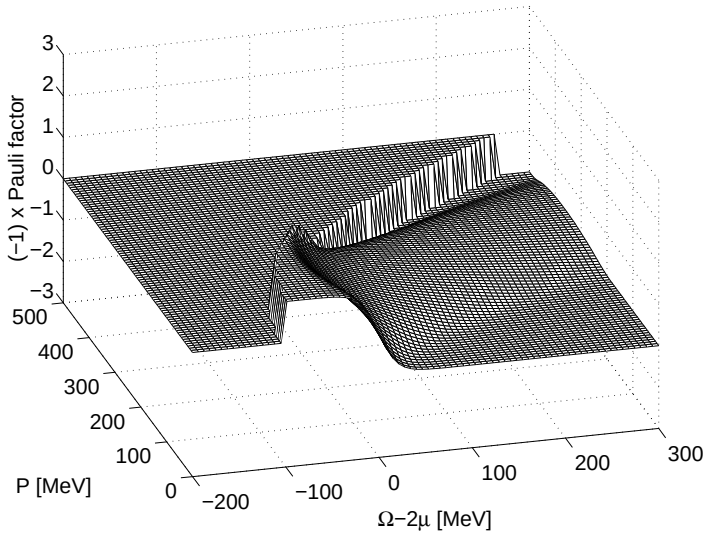

Figure 4.4: *The Pauli factor for a quasiparticle pair in the $\Omega - P$ plane. The relative momentum k_0 of the pair is fixed by the condition that $g^0_{II}(P, \Omega, k_0)$ must be singular. An effective mass parameterization was used. The parameters, $m^* = 670\,MeV$ and $U_0 = -90\,MeV$, were fitted to the quasiparticle energy spectrum that was used for the calculation in the left panel of Fig. 4.3. Also ρ and T were taken from there.*

and can be understood as a superposition of NN pairs with particles of opposite spin and momentum. Unfortunately, the pair condensation process cannot be described in the framework of the type of 'normal' Green's functions that were considered here. The reason is, that below T_C, the perturbation expansion for the propagator becomes instable. An illustrative discussion concerning this breakdown, which is referred to as pairing instability, can be found in Ref. [mat67]. The breakdown of the propagator expansion at T_C is signaled by the formation of a pole in the T matrix at $\Omega = 2\mu$ for pairs with opposite momentum. Decreasing the temperature from above T_C, the critical temperature is reached, if the condition

$$\det\left[\mathbb{M}^{\alpha}(P = 0, \Omega = 2\mu)\right] = 0 \tag{4.9}$$

is fulfilled in any channel $\alpha = JST$ (the notation of Section 3.4 was applied). Eq. (4.9) is the so-called Thouless criterion for the transition temperature of the

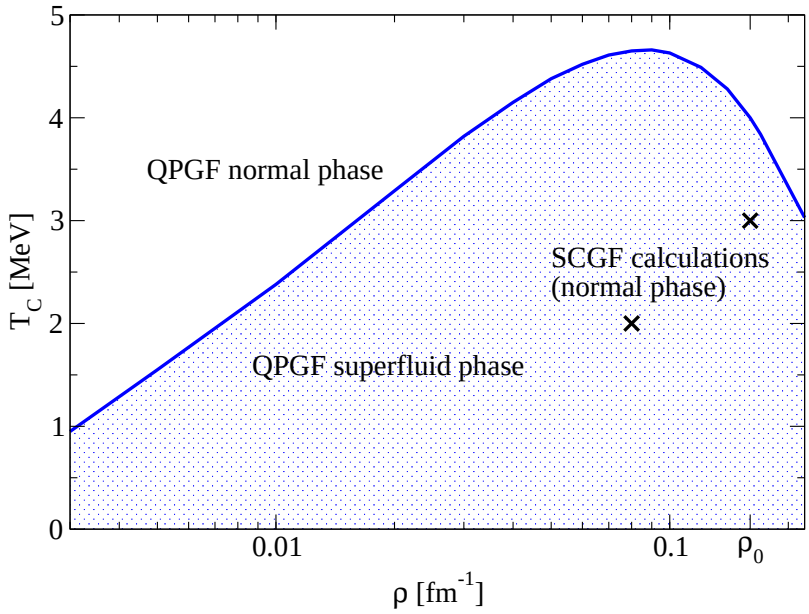

Figure 4.5: *The critical temperature T_C in the ${}^3S_1 - {}^3D_1$ channel in symmetric nuclear matter. T_C is obtained from the Thouless condition (4.9), using a quasiparticle T matrix. The crosses indicate that calculations in the full SCGF scheme are still possible in the normal phase below the transition temperature deduced from the quasiparticle scheme.*

normal phase to the superfluid phase [tho60]. In a nuclear system around saturation density, proton-neutron pairing will preferentially occur in the ${}^3S_1 - {}^3D_1$ (deuteron) channel. Fig. 4.5 shows the critical temperature in this channel as derived from Eq. (4.9), using a QPGF type g^0_{II}.

As pointed out already, it is conceptually impossible to study the superconducting phase within the formalism adopted for this Thesis, at least without an extension of the Green's function theory to anomalous propagators [gor58, nam60, abr75]. However, a precursor structure of the pole in the T matrix can be observed in the temperature range well above T_C. This was studied in a quasiparticle scheme in Ref. [alm96]. In Fig. 4.6, the real part of the T matrix is displayed for two different temperatures. At low temperature, a strong enhancement of the attraction of pairs with opposite momentum and pair energies around $\Omega = 2\mu$ is visible. In all other parameter regions, the two graphs look very similar. Inspecting once again Fig. 4.3, the dispersive structure in the imaginary part of the quasiparticle

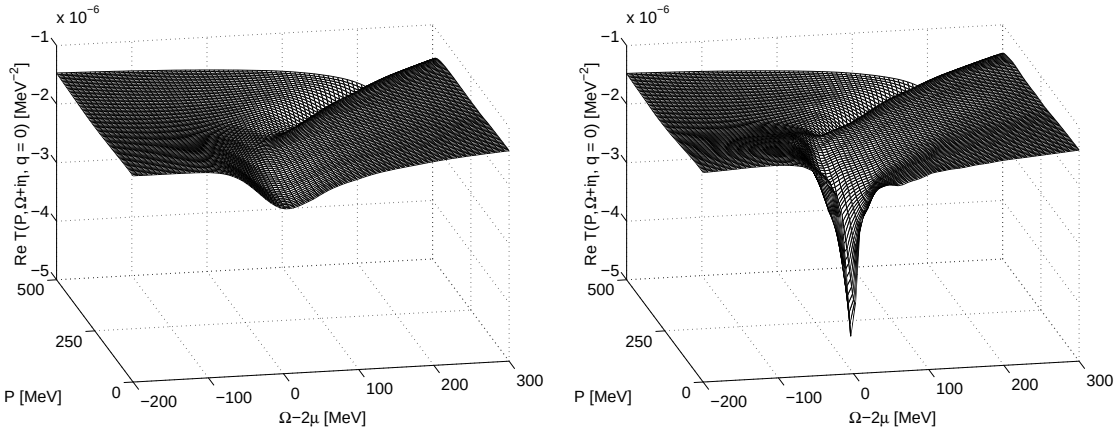

high temperature low temperature

Figure 4.6: *Precursor effect of the transition to the superconducting phase in the SCGF scheme. The real part of the T matrix is displayed for a high temperature of $T = 20\,MeV$ (left panel) and a low temperature of $T = 3\,MeV$ (right panel). For pair energies of $\Omega = 2\mu$, the low temperature T matrix is very attractive for pairs with zero center of mass momentum. The relative momentum is set to zero, and the density is $\rho = 0.16\,fm^{-3}$.*

T matrix at low values of P can also be interpreted as the precursor structure of the pole.

The effect is significantly reduced in the full scheme, where the depletion of the Fermi sea due to short-range correlations, in addition to the temperature-induced reduction of occupation at the Fermi surface, weakens the pairing correlations. Thus, the critical temperature in a full SCGF calculation should be lower than for a system of quasiparticles. The fact that it is possible to perform a self-consistent calculation at saturation density and a temperature of $T = 3\,\mathrm{MeV}$ in the normal phase demonstrates that T_C is overestimated in a quasiparticle scheme (cf. Fig. 4.5). A similar reduction of T_C has also been observed in Ref. [boz99], using a simple separable potential of rank one, as well as in finite nuclei [hei95].

4.3 Self Energy and an Extrapolation to Zero Temperature

Once the T matrix is obtained on the (P, Ω, q)-mesh, a three-dimensional interpolation has to be applied in order to perform the transformation to the integration variables that appear in the energy-momentum integrals for the imaginary part of the self energy in Eq. (3.45). The three-dimensional integral over $\mathbf{k}'$ is carried out in spherical coordinates (remember that $q = \frac{1}{2}|\mathbf{k} - \mathbf{k}'|$). Without loss of generality, $\mathbf{k}$ can be chosen along the z axis. The ϕ' integration is trivial and yields a factor 2π, and so the remaining integration variables are k', θ' and ω'. Since it is not meaningful to define a Fermi momentum in a hot system, the quantity k^* is introduced for a density ρ,

$$k^* = \left(\frac{3\pi^2\rho}{2}\right)^{\frac{1}{3}}. \tag{4.10}$$

This is the Fermi momentum of a free Fermi sea at zero temperature. For some densities, the corresponding k^* is listed in Tab. 4.2. In principle, the k' integration must be carried out up to infinity, in practice, momenta k' up to about four to five times k^* contribute.

Fig. 4.7 displays $\mathrm{Im}\Sigma(k = 0, \omega)$ for a temperature of 3 MeV and $\rho = 0.16\,\mathrm{fm}^{-3}$. One can observe that the imaginary part has a global minimum around $\omega = 200\,\mathrm{MeV}$. For positive values of ω, it decays very slowly and extends to more than 100 GeV (which cannot be seen on the plot any more). For negative values of ω, there is a local minimum at $\omega = -90\,\mathrm{MeV}$, below which $\mathrm{Im}\Sigma$ tends to zero within some hundreds of MeV's.

The qualitative behavior of the self energy in in the vicinity of the chemical potential, between the two minima, can be understood with Fig. 4.8. For a nucleon with zero momentum k, the composition of the self energy is studied for $\omega = \mu - \delta$ (top row), $\omega = \mu$ (middle row) and $\omega = \mu + \delta$ (bottom row). The parameter δ is set to

ρ	[fm^{-3}]	0.08	0.1	0.16	0.2	0.3	0.4	0.5
k^*	[MeV]	209	225	263	283	324	357	385

Table 4.2: *Conversion between the density and the Fermi momentum of a system at zero temperature.*

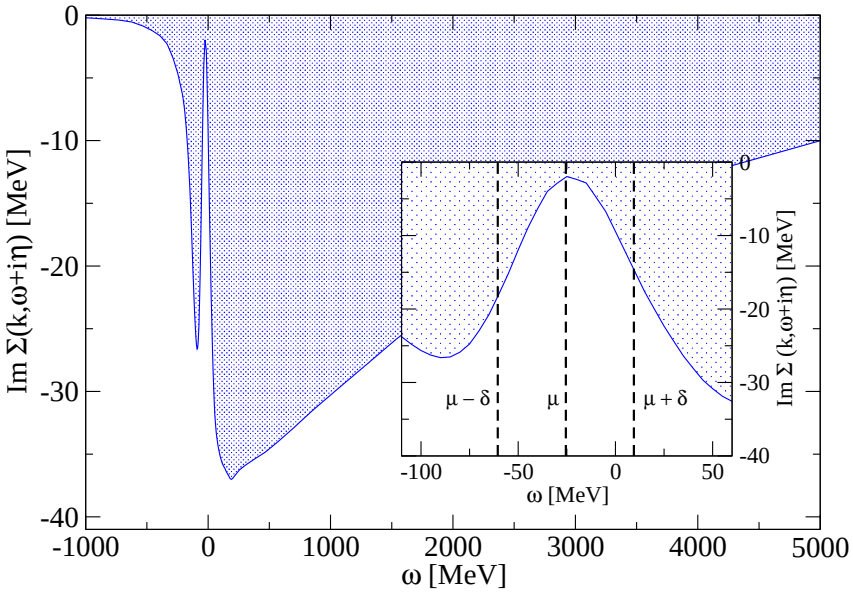

Figure 4.7: *Imaginary part of the retarded self energy for a nucleon with zero momentum. The region close to* $\omega = \mu$ *is displayed separately in the inset. The parameters are* $T = 3\,MeV$ *and* $\rho = 0.16\,fm^{-3}$.

35 MeV. The three factors contributing to ImΣ in the integrand of Eq. (3.32),

$$I(k',\omega') = \langle \mathbf{kk}'|\mathrm{Im}T(\omega+\omega'+\mathrm{i}\eta)|\mathbf{kk}'\rangle_A \times A(k',\omega') \times [f(\omega')+b(\omega+\omega')], \quad (4.11)$$

are displayed separately, as well as their product, as a function of ω', for three momenta k' in the vicinity of k^*. This is a (momentum) domain where large contributions are to be expected in the momentum integration. Each of the four curves are rescaled to arbitrary units in order to compare all of them in a single plot. The dashed line is proportional to $\langle \mathbf{0k}'|\mathrm{Im}T(\omega+\omega'+\mathrm{i}\eta)|\mathbf{0k}'\rangle_A$. This contribution crosses zero at $\omega' = 2\mu - \omega$. The solid line is the spectral function, $A(k',\omega')$, and the hatched area denotes the energy domain where the phase space factor, $[f(\omega')+b(\omega+\omega')]$, is different from zero. The ω'-integral over the product of the three contributions is given by the shaded area. In the upper row, the phase space factor describes the thermally unoccupied phase space from $\omega' \simeq \mu$ up to $\omega' \simeq \mu + \delta$. The upper limit guarantees that the total energy of the process $\omega + \omega' < 2\mu$, such that the process describes scattering of backward propagating intermediate states. In the bottom row, the phase space factor covers the thermally occupied region down to an energy of $\omega' \simeq \mu - \delta$ and so the total energy

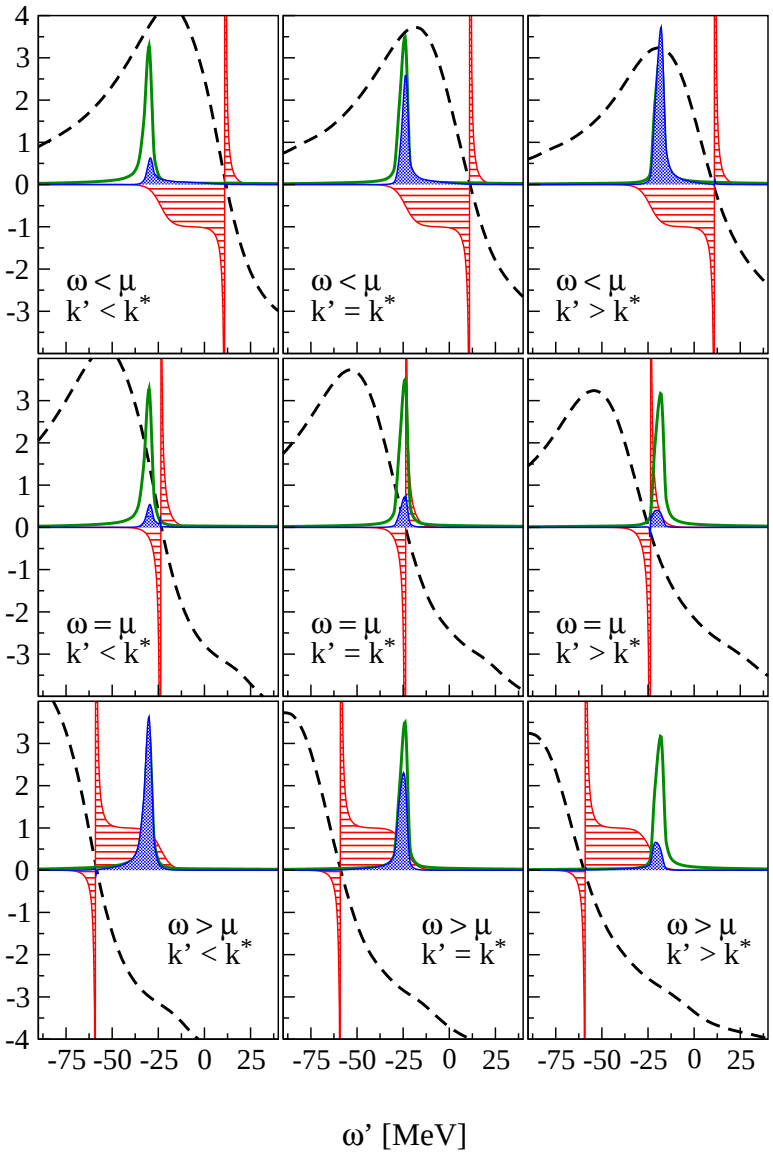

Figure 4.8: *Contributions to the integral of* $\mathrm{Im}\Sigma(k = 0, \omega + \mathrm{i}\eta)$ *as a function of the integration variable* ω'*, for three distinct values of* ω *(*$\omega = \mu - 35\,MeV$*,* $\omega = \mu$ *and* $\omega = \mu + 35\,MeV$*) and for three distinct values of the integration variable* k' *(*$k' = k^* + 20\,MeV$*,* $k' = k^*$ *and* $k' = k^* - 20\,MeV$*). The dashed line is proportional to* $\mathrm{Im}T(\omega + \omega' + \mathrm{i}\eta)$*, the solid line represents the spectral function (in arbitrary units) and the hatched area marks a phase space factor that is different from zero. The shaded area is the product of all three curves and it is proportional to the contribution to the self energy at the respective value of* k'*.*

is $\omega + \omega' > 2\mu$. Note that in all nine figures, the pole of the phase space factor at $\omega' = 2\mu - \omega$ is canceled by the zero in the matrix element as discussed in Section 4.2.

To get a rough estimate of the relative size of ImΣ at the respective energy ω, one should 'integrate' by eye over the size of the shaded areas of all three plots in each row. One can observe that in the first row, at $\omega = \mu - \delta$, this integrated result is large, with a dominant contribution to ImΣ from states that are characterized by $k' > k^*$, the so-called particle states (see upper right plot). Only for these states, the peak of the spectral function is located in a region with a sizeable phase space factor. The contrary effect can be observed for $\omega > \mu$. There, the main contribution is from hole states (bottom left plot). For $\omega = \mu$ (middle row), the phase space factor extends to $\mu \pm \epsilon(T)$, where $\epsilon(T)$ goes to zero at zero temperature. It is this vanishing phase space that brings Im$\Sigma(k, \omega = \mu)$ to zero at $T = 0$. Fig. 4.8 corresponds to a temperature of $T = 3\,\mathrm{MeV}$, and so the integral over k' yields a small but finite contribution.

The momentum k has been set zero in Fig. 4.8, but the behavior of Im $\Sigma(k, \omega)$ does not change qualitatively for other momenta. The only dependence upon k is contained in the matrix element, however, the position of the node at $\omega' = 2\mu - \omega$ is independent of k.

The energy dependence of Im$\Sigma(k = k^*, \omega)$ in the two tail regions is displayed in Fig. 4.9 for various densities. In the right panel, one can observe a rather linear dependence of ImΣ upon the density. To understand this behavior, it is again instructive to inspect Eq. (4.11) and Fig. 4.8. For an arbitrary momentum k, and $\omega > \mu$, the dominant contribution to Im$\Sigma(k, \omega)$ comes from occupied states, most of which are located below k^* (although there is of course a finite occupation of high momentum states due to correlations and temperature). A larger Fermi sea will therefore increase Im$\Sigma(k, \omega)$. The dependence of the matrix element, $\langle \mathbf{k}^* \mathbf{k}' | \mathrm{Im}T(\omega + \omega' + \mathrm{i}\eta) | \mathbf{k}^* \mathbf{k}' \rangle_A$, upon the integration variables k' and ω' is shown in Fig. 4.10 for the same densities. Obviously, the T matrix is only weakly density dependent in the high frequency limit and this explains that the self energy is proportional to the density for $\omega \gg \mu$. This behavior is in line with the argument that an integration over a hole line yields a factor that is proportional to the density (cf. the paragraph about Brueckner in the Introduction of this Thesis).

The situation is different for the opposite tail region, which is shown in the left panel of Fig. 4.9. For $\omega < \mu$, the main contribution to ImΣ is due to the momentum integration over states with $k' > k^*$, so that there is no upper bound

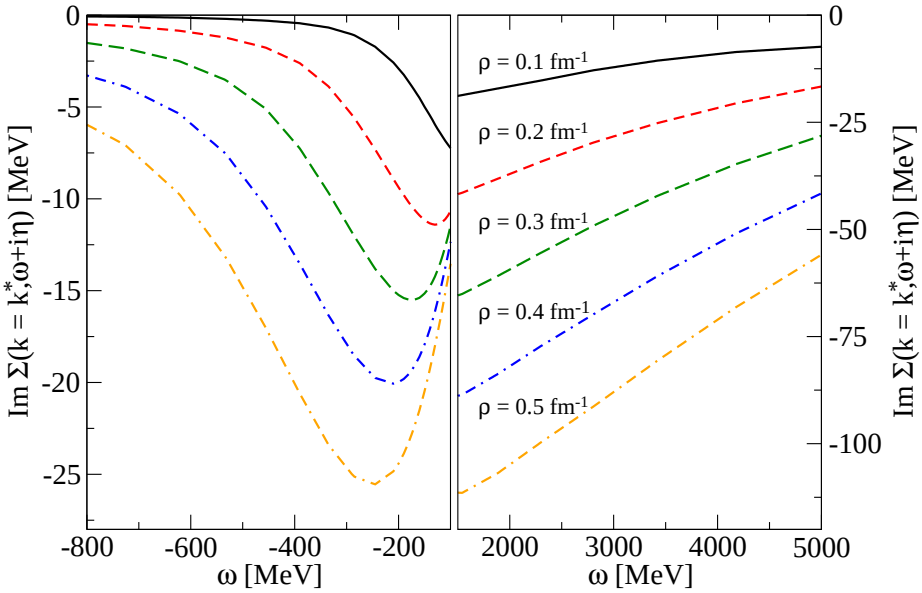

Figure 4.9: *Density dependence of the energy tails of the retarded self energy at $k = k^*$. The five densities are indicated in the right panel. The temperature is $T = 10$ MeV.*

for the integration variable k'. The size of ImΣ is limited by the attenuation of $\langle \mathbf{k}^*\mathbf{k}'|\mathrm{Im}T(\omega+\omega'+\mathrm{i}\eta)|\mathbf{k}^*\mathbf{k}'\rangle_A$. Although the negative energy tail region ($\omega < 0$) is not very well resolved in Fig. 4.10, one can see that both for high values of k' and for $\omega + \omega' \to -\infty$, the matrix element goes to zero. The decay of the T matrix element is strongly density dependent: at higher densities, the matrix element extends to higher negative values of ω' and up to higher momenta k'. Also, the maximum value of the matrix element increases with ρ. This is the reason that the negative energy tail of ImΣ has a very strong density dependence.

It has been mentioned in Section 4.1 that no calculations can be performed at zero temperature with the implemented scheme. Nevertheless, it would be very interesting to have information about the self energy or also the spectral function at zero temperature, since the nuclei that can be studied in experiments are usually zero temperature systems. Therefore, a method was developed that allows an extrapolation of the imaginary part of the self energy to zero temperature. Self consistent results for ImΣ were computed at a number of different temperatures and stored on a (k, ω) mesh. For each k and ω, a second order polynomial was fitted

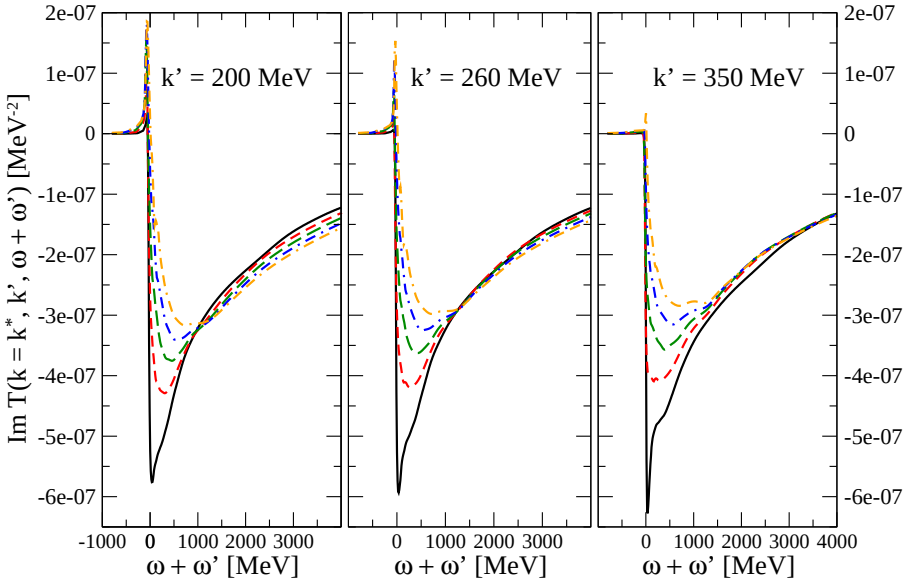

Figure 4.10: *Density dependence of the high energy tails of the retarded T matrix. The temperature and the five densities values are the same as in Fig. 4.9.*

to the stored values. From this polynomial, an extrapolated or interpolated value can be obtained at a desired temperature. The chemical potential at $T = 0\,\mathrm{MeV}$ was also derived as an extrapolation of the finite T values. Following the phase space argument of Luttinger [lut61], a parabolic shape of $\mathrm{Im}\Sigma$ was assumed in the vicinity of the chemical potential,

$$\mathrm{Im}\Sigma(k,\omega) = a(\omega - \mu)^2. \tag{4.12}$$

The curvature a was extrapolated from the curvatures of the self-consistent results, too. In Fig. 4.11, the extrapolated zero temperature self energy at saturation density is compared to the various self-consistent finite temperature results for two different momenta, $k = 0$ and $k = k^*$. A smooth behavior is found, and it appears that this is a promising way to derive information for a zero temperature system from SCGF calculations at finite temperature. However, one remark should be added: Although it has been shown in Section 4.2 that the pairing correlations that lead to a superconducting state are weakened in the full T matrix approach, a transition temperature $T_C > 0$ is possible below the temperature region that can be covered by the calculations. Of course, the extrapolated result cannot provide

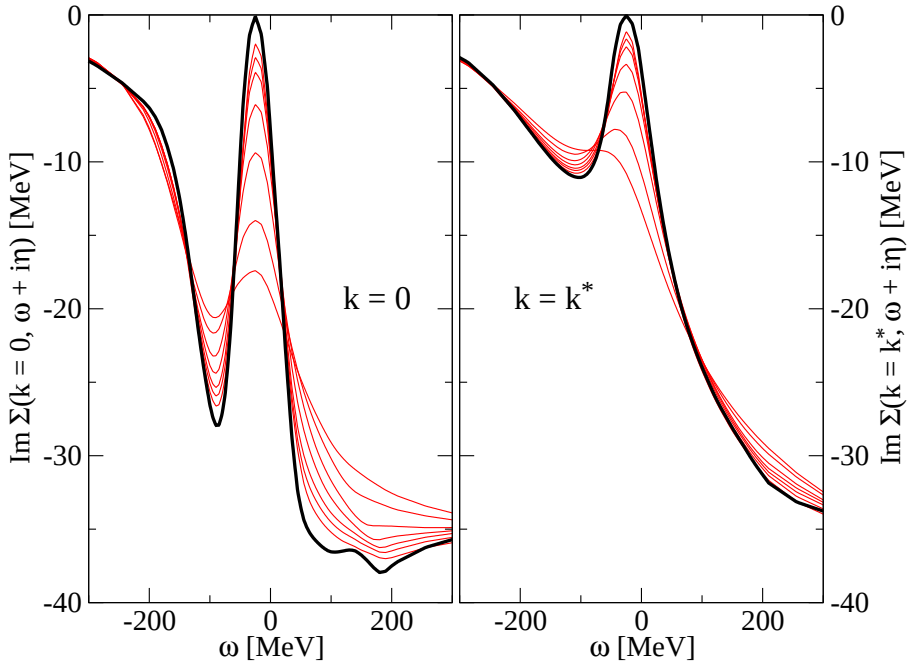

Figure 4.11: *Extrapolation of* $\mathrm{Im}\Sigma(k, \omega + \mathrm{i}\eta)$ *to zero temperature (bold solid line) at two different momenta,* $k = 0$ *and* $k = k^*$*. The self consistent results at* $T = 3, 4, 5, 7, 10, 15$ *and* 20 *MeV are displayed for comparison (thin solid lines).*

any information about such a superconducting state.

The real part of the self energy is the sum of the generalized HF self energy and a dispersive contribution. The dispersive part of $\mathrm{Re}\Sigma$ is determined by means of a straightforward evaluation of the principal value integral, Eq. (3.31),

$$\mathrm{Re}\,\Sigma(k,\omega) = \Sigma^{HF}(k) - \frac{\mathcal{P}}{\pi}\int_{-\infty}^{+\infty} \mathrm{d}\lambda\, \frac{\mathrm{Im}\,\Sigma(k,\lambda+\mathrm{i}\eta)}{\omega-\lambda}. \tag{4.13}$$

To obtain the full real part, the energy independent Hartree-Fock self energy must be added, using the correlated momentum distribution that is derived from the non-trivial spectral function. The real part of the extrapolated self energy is obtained in the same way as in the finite temperature case. For the Hartree-Fock part, another extrapolation to zero temperature must be applied. In this case, the temperature dependence is only very weak, which was already visible in Fig. 2.9.

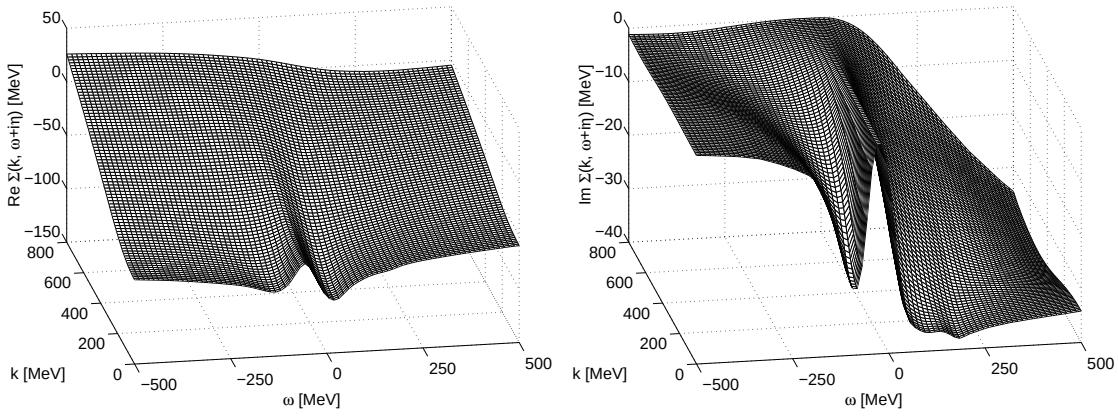

Figure 4.12: *Full momentum and energy dependence of the self energy. Real and imaginary part of* $\Sigma(k, \omega + \mathrm{i}\eta)$ *are shown at zero temperature and saturation density.* $\mathrm{Im}\Sigma(k, \omega + \mathrm{i}\eta)$ *was obtained by an extrapolation technique that is explained in the text.*

The full momentum and energy dependence of the real and the imaginary part of the self energy at zero temperature and saturation density is displayed in Fig. 4.12. Note that the relative importance of the energy dependence is reduced in the real part, which is due to the large energy independent Hartree-Fock contribution that was added.

The on-shell value of Σ is obtained by Eq. (3.24), in the same way as the HF or the BHF single-particle potential. Although $\Sigma(k, \epsilon(k))$ does not play the same role in the SCGF approximation in the sense that is is possible to compute the internal energy from it, the full result can be compared to the results for the single-particle potentials that are obtained in the other truncation schemes. In the left panel of Fig. 4.13, one can observe that the BHF result yields about 40 MeV more attraction than the HF result. This is the well-known effect of short range correlations — incorporated both in the G matrix and the T matrix — that keep the nucleons from penetrating their repulsive cores. Comparing the two approaches that include correlation effects, the BHF self energy is 20 MeV more attractive than the SCGF result for low momenta. A similar effect has also been observed in calculations, where hole-hole scattering is taken into account on a quasiparticle level [alm96, fri02]. Obviously, hole-hole scattering in intermediate states is a repulsive process that makes the single-particle spectrum shallower for

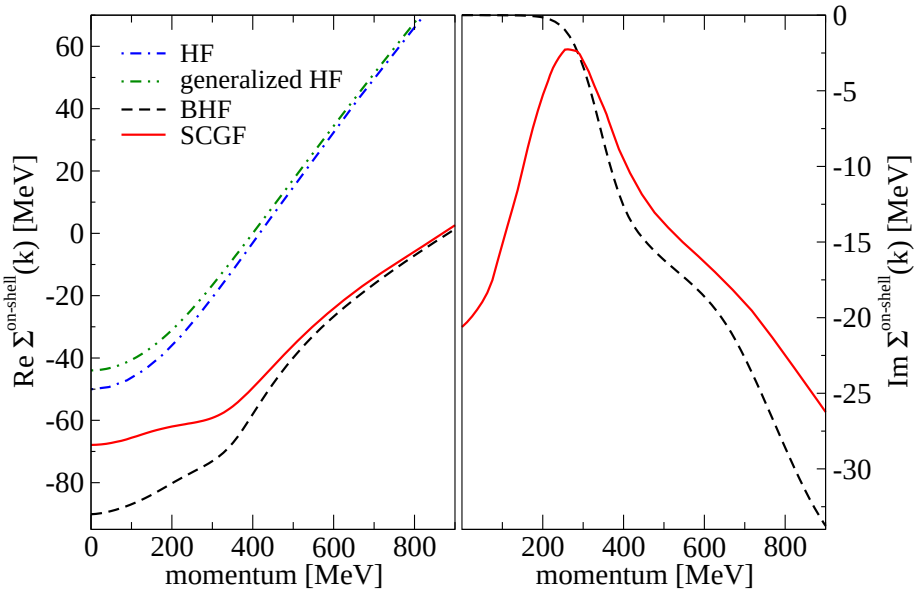

Figure 4.13: *On-shell behavior of the SCGF self energy (solid lines). The real part (left panel) is compared to the BHF and the HF single-particle potential (dashed line and dash-dotted line). The generalized HF contribution is also reported. The imaginary part is compared to the imaginary part of the BHF potential (right panel). The parameters are* $\rho = 0.16\,fm^{-3}$ *and* $T = 5\,MeV$.

the hole states.

It would be interesting to judge the effect of the dressing of the ladders on the on-shell self energy, by comparing the SCGF and the QPGF results. For reasons that were explained in Section 3.5, it is not possible to derive a fully converged single-particle spectrum within the QPGF scheme and therefore, a quantitative comparison of the on-shell self energies would be questionable. However, it is possible to compare the energy-independent contributions. The difference between the simple HF result and the generalized HF contribution to the real part of the full SCGF self energy is only moderate. This indicates, at least for the energy-independent part, that the effect of dressing on the on-shell self energy is not very important [fri04].

In the right panel of Fig. 4.13, the imaginary part of the on-shell self energy is displayed. In the BHF approximation, $\mathrm{Im}\,\Sigma(k, \epsilon(k))$ is interpreted as an optical

potential that describes the absorption of a particle state with momentum k. In the SCGF picture, $\mathrm{Im}\,\Sigma(k, \epsilon(k))$ is connected to the on-shell width of a general (particle or hole) state k,

$$\Gamma(k) = -2\mathrm{Im}\,\Sigma(k, \epsilon(k)). \tag{4.14}$$

Whereas the BHF on-shell width goes to zero for the hole states, because the G matrix does not include hole-hole propagation, a local maximum of the SCGF width can be observed for the deepest bound states. The width assumes a minimum at the Fermi surface that is located around $k = 260\,\mathrm{MeV}$. Above, the BHF result and the SCGF result are qualitatively similar. The dependence of the width upon the temperature and the density will be further discussed in Section 4.4.

4.4 Spectral Functions

In this Section, the results for the nucleon spectral functions will be presented and discussed. A first interesting point is to clarify in which way the self-consistent solution differs from the quasiparticle result. Secondly, the temperature and density dependence is discussed, and finally, the theoretical spectral functions are compared to experimental results that were recently obtained for the ^{12}C nucleus.
The solid lines in Fig. 4.14 represent the self-consistent spectral function for a temperature of $10\,\mathrm{MeV}$ and a density of $0.16\,\mathrm{fm}^{-1}$, at three different momentum states, $k = 0$, $k = k^*$ and $k = 2k^*$. The position of the global maximum of the spectral function, the quasiparticle peak, is located at the quasiparticle energy, $\epsilon(k)$. At $k = k^*$, the quasiparticle energy coincides with the chemical potential, $\epsilon(k) = \mu$ (middle panel). Correlations between nucleons are responsible for the fragmentation of the strength distribution over a very large energy domain. Recall that in Section 3.1, a probabilistic interpretation was given for either of the two contributions to the spectral function, the correlation functions $g^<$ and $g^>$.
To illustrate the effect of self-consistency, the full SCGF result is compared to the QPGF spectral function (dashed line). Especially for the deeply bound states (left panel), the self-consistent spectral function displays a negative energy tail that is much more pronounced than in the quasiparticle approach. This behavior can be traced back to the structure of the imaginary part of the quasiparticle T matrix at negative pair energies (cf. Fig 4.3), which is zero below a threshold energy. At high momentum values (right panel), the spectral function looks quite similar in

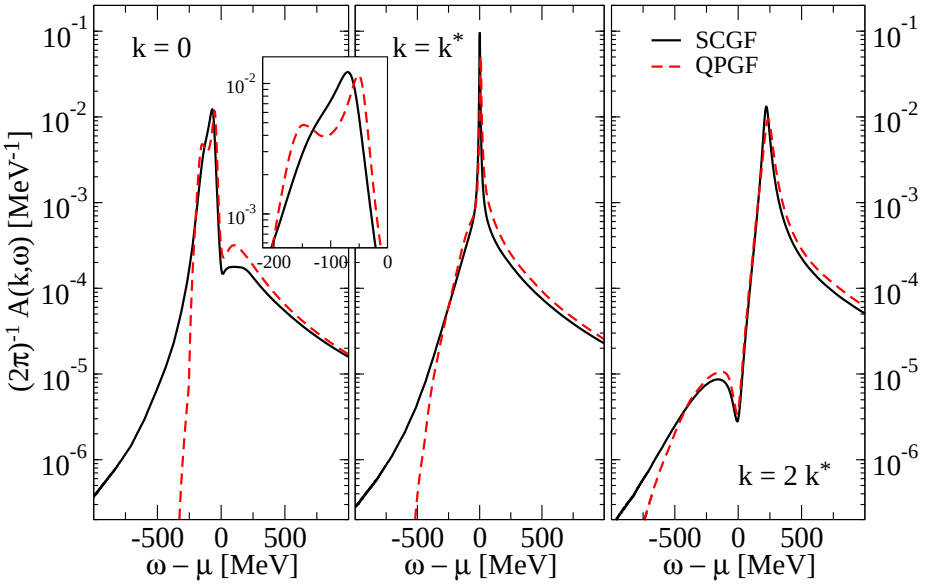

Figure 4.14: *Comparison between a self consistent spectral function (solid line) and a quasiparticle spectral function (dashed line) for three different momenta. The inset shows the region of the quasiparticle peak for zero momentum states. The parameters are* $\rho = 0.3\,fm^{-3}$ *and* $T = 10\,MeV$.

both pictures.

The blow up in the inset of Fig. 4.14 shows a quasiparticle spectral function with a double-hump structure. One peak is located at $\omega = \mu - 50\,\mathrm{MeV}$ and a second one at $\omega = \mu - 150\,\mathrm{MeV}$. The first of the two maxima corresponds to the quasiparticle peak. The breakdown of the quasiparticle picture that was described in Section 3.5 is connected to the appearance of the second maximum. Either of the two peaks represents a possible solution for the quasiparticle energy, Eq. (3.56). The fragmentation signals a strong coupling of one-hole states to two-hole one-particle excitations in the quasiparticle description. This effect is reduced by a self-consistent dressing of the Green's function.

The temperature dependence of the SCGF result at saturation density is shown in Fig. 4.15. Spectral functions at four different temperatures, $T = 0\,\mathrm{MeV}$, $T = 3\,\mathrm{MeV}$, $T = 10\,\mathrm{MeV}$ and $T = 20\,\mathrm{MeV}$, are compared at the same momentum values as in Fig. 4.14. All finite temperature results have been obtained from self-consistent calculations. The zero temperature curve (solid line) has been computed with the extrapolation routine that was explained in Section 4.3, based on

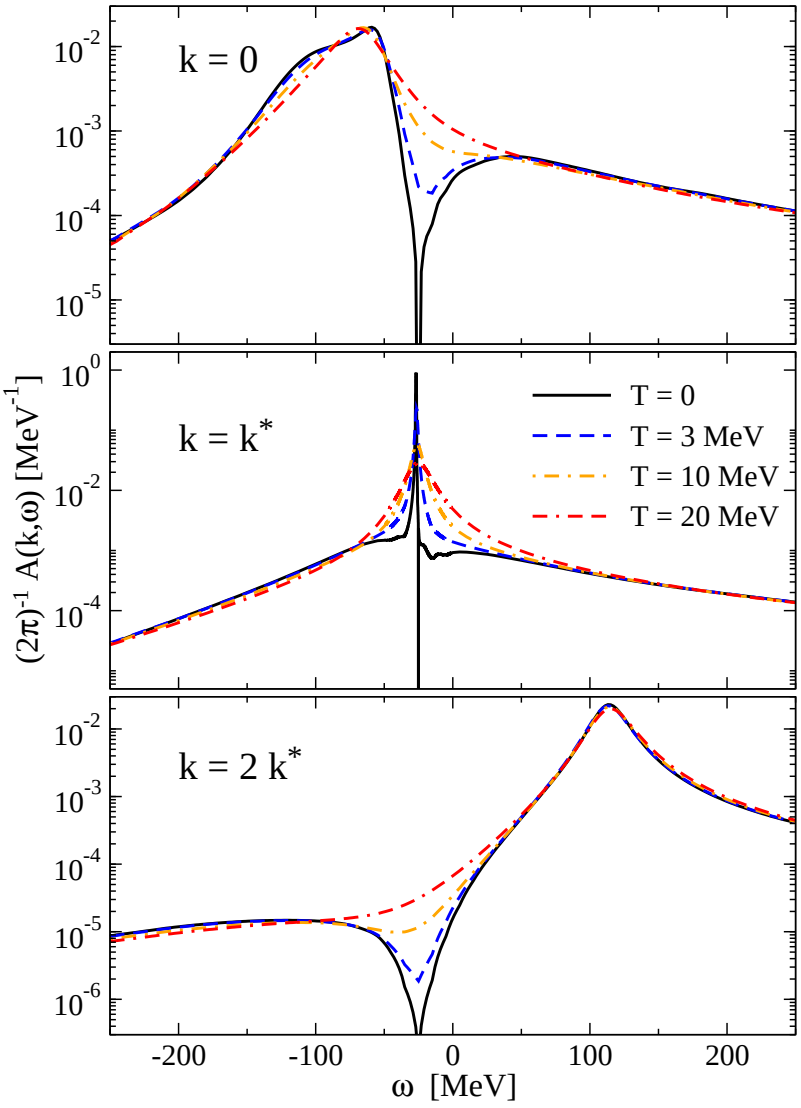

Figure 4.15: *Temperature dependence of the spectral function. The spectral function is displayed for four different temperatures, $T = 0$, $T = 3\,MeV$, $T = 10\,MeV$ and $T = 20\,MeV$. The momenta are $k = 0$ (top), $k = k^*$ (middle) and $k = 2k^*$ (bottom). All calculations were performed at saturation density.*

T [MeV]	$\Gamma(0)$ [MeV]	$\Gamma(k^*)$ [MeV]	$\Gamma(2k^*)$ [MeV]
3	44.2	2.5	29.0
4	42.4	3.5	28.9
5	41.2	4.5	28.9
7	39.9	6.9	29.3
10	39.1	10.8	30.1
15	38.6	16.9	31.2
20	39.1	22.2	32.3

Table 4.3: *Temperature dependence of the on-shell width of the spectral function at zero momentum, k^* and $2k^*$. The calculations were performed at saturation density.*

independent calculations between $T = 3\,\mathrm{MeV}$ and $T = 20\,\mathrm{MeV}$. The extrapolated result displays the correct limit behavior and vanishes at $\omega = \mu$, so that the hole and the particle part of the spectral function are separated from each other. A separation of a particle part and a hole part is no longer visible at finite temperature; the correlation functions $g^<$ and $g^>$ are both defined below and above $\omega = \mu$. The zero temperature spectral function has a very narrow peak at $\omega = \mu$ for momentum states close to the Fermi surface. This peak is broadened already at $T = 3\,\mathrm{MeV}$, and, in the temperature range up to $20\,\mathrm{MeV}$, the width of the peak of the spectral function increases strongly for these loosely bound states. In contrast, the spectral functions are relatively weakly temperature dependent outside a region defined by the interval $[\mu - 50\,\mathrm{MeV}, \mu + 50\,\mathrm{MeV}]$. The widths of the deeply bound hole states and the high momentum particle states are hardly influenced by an increasing thermal motion. In Tab. 4.3, the on-shell widths are reported for different temperatures.
The density dependence of the spectral function is shown in Fig. 4.16. Self-consistent spectral functions are plotted at five different densities between $\rho = 0.1\,\mathrm{fm}^{-3}$ and $\rho = 0.5\,\mathrm{fm}^{-3}$. Again, the momenta are the same as in Fig. 4.14. The negative energy tails of the low density spectral functions are suppressed, which is due to the suppression of $\mathrm{Im}\,\Sigma$ in this region (cf. Fig. 4.9). Due to the same effect, the quasiparticle peaks of the deeply bound states broaden with increasing density. A broadening can also be observed for the widths of the quasiparticle peaks at high momenta. However, the situation is vice versa for the weakly bound states with a peak close to $\omega = \mu$. In Section 4.3, it was illustrated that at $\omega = \mu$, the

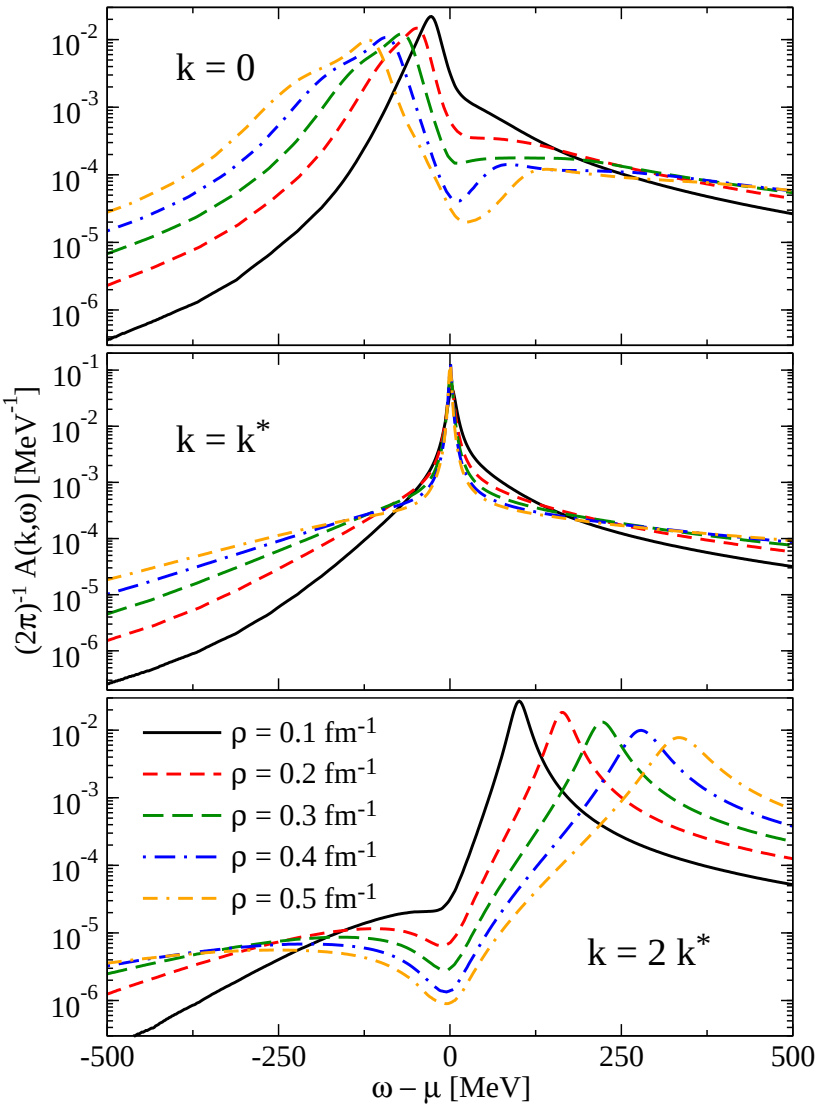

Figure 4.16: *Density dependence of the spectral function. The spectral function is displayed at five different densities, from* $\rho = 0.1\,fm^{-3}$ *to* $\rho = 0.5\,fm^{-3}$*, in equidistant steps. The momenta are* $k = 0$ *(top),* $k = k^*$ *(middle) and* $k = 2k^*$ *(bottom). The temperature for all calculations is* $T = 10\,MeV$*.*

ρ [fm^{-3}]	$\Gamma(0)$ [MeV]	$\Gamma(k^*)$ [MeV]	$\Gamma(2k^*)$ [MeV]
0.1	29.1	13.6	23.8
0.2	44.7	9.2	34.9
0.3	54.8	6.5	48.6
0.4	62.4	4.9	64.7
0.5	68.0	4.2	82.7

Table 4.4: *Density dependence of the on-shell width of the spectral function at zero momentum, k^* and $2k^*$. The temperature for all calculations is $T = 10\,MeV$.*

imaginary part of the self energy goes to zero in a completely degenerate system, because there is no phase space available for excitation processes. Comparing two Fermi systems at the same (finite) temperature and different densities, the Fermi surface of the one with the higher density is more degenerate. Therefore, it is not surprising that the width of the quasiparticle peak in this region decreases with increasing density. The density-dependence of the on-shell widths is summarized in Tab. 4.4 for the three momenta.

Because the cross sections for knock-out reactions, such as (e,e′p) or (p,2p), and pick-up reactions, such as (p,d) or (d,^{3}He), are proportional to the (zero temperature) spectral function, it is clear that this quantity is not only interesting for theoretical physicists, but it is also useful for experimentalists. The cross section for an (e,e′p) reaction, for instance, can be written as [bat01],

$$\frac{\mathrm{d}^6\sigma}{\mathrm{d}E_{e'}\mathrm{d}\Omega_{e'}\mathrm{d}E_{p'}\mathrm{d}\Omega_{p'}} = K\,\sigma_{ep}\,A(k,-E). \tag{4.15}$$

$E_{e'}$, $\Omega_{e'}$, $E_{p'}$ and $\Omega_{p'}$ denote the energy and the solid angle of the out-going particles, K is a kinematical factor, and $A(k,-E)$ is the hole part of the spectral function. The missing energy E (> 0) must be reconstructed from the energy transfer and the kinetic energies of the out-going fragments, and k is determined by the momentum transfer and the momentum $k_{p'}$ of the detected proton. Unfortunately, σ_{ep}, the off-shell electron-proton cross section is experimentally non-accessible and must be calculated from a theoretical model. There exist several choices that produce different results, especially in the interesting region at high k and E.
One method to constrain a theoretical spectral function for a finite nucleus by experimental data from an (e,e′p) process would be to calculate the cross section of

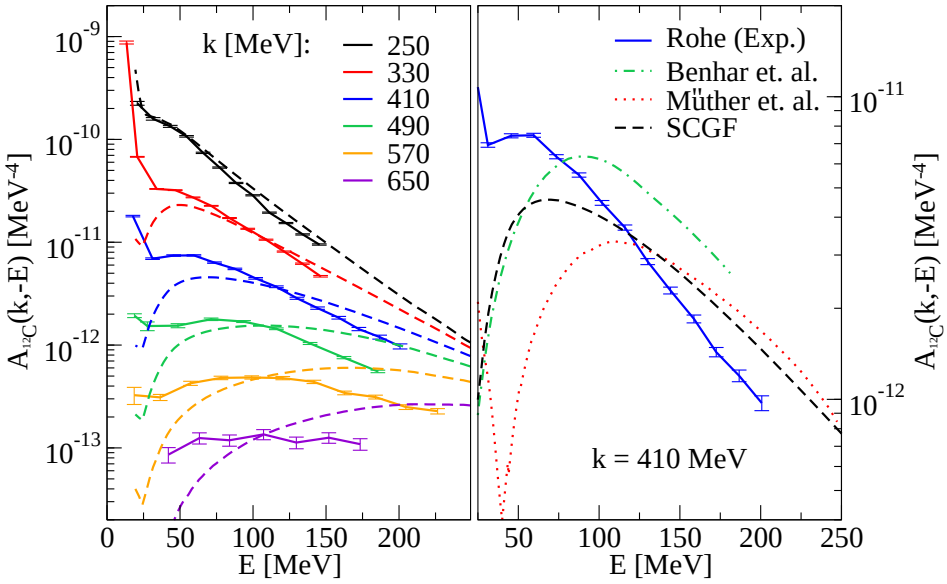

Figure 4.17: *Spectral function in the* ^{12}C *nucleus. Left panel: Experimental result for several momenta above the Fermi momentum (solid lines with error bars). The data are similar to those presented in Ref. [roh03], but the choice cc was used for* σ_{ep} *instead of cc*1*. The dashed lines represent the SCGF nuclear matter spectral function at a density of* $\rho = 0.08\,fm^{-3}$*. To compare the nuclear matter spectral function with the experimental result, it must be multiplied by a normalization factor of* $4Z(2\pi)^{-4}\rho^{-1}$*. Right panel: A comparison between the experimental result at* $k = 410\,MeV$ *(solid lines with error bars), the theoretical spectral functions for a finite system by Benhar et. al. [ben94] (dashed line) and Müther et. al. [mut95] (dotted line), and the SCGF result (solid line).*

the knock-out reaction according to Eq. (4.15) and to compare the result with the experiment. Another possibility is to proceed the other way round. Recently, Rohe has carried out (e,e′p) experiments on the nuclei C, Al, Fe and Au [roh03]. Starting from the measured cross section of the reaction, she extracted the experimental spectral function for carbon, $A_{^{12}C}(k,\omega)$. Of course, this quantity is also biased by the uncertainties of the off-shell electron-proton cross section σ_{ep}. In the analysis, particularly the high momentum and high energy region up to $k = 650\,\mathrm{MeV}$ and $E = 500\,\mathrm{MeV}$ was explored. In the energy region above $E \approx 150 - 250\,\mathrm{MeV}$, there are contaminations due to inelastic excitations of nucleons and final state

interactions of the out-going nucleon with the residual nucleus. Such processes are not considered in the Green's function description of the spectral functions and therefore, this region is not suitable for a comparison between theory and experiment. Only below $E \approx 150 - 250\,\mathrm{MeV}$, it is possible to describe the measured spectral functions by the kind of physical processes that are taken into account in a T matrix description.

The direct comparison between $A_{^{12}C}$ and a spectral function for infinite nuclear matter is problematic, because the latter cannot account for the finite size effects of a nucleus. Anyway, to give a qualitative orientation, the ^{12}C spectral function in the high-momentum region is shown in the left panel of Fig. 4.17, together with a nuclear matter spectral function that was calculated at the mean density of the ^{12}C nucleus, $\rho \approx 0.08\,\mathrm{fm}^{-3}$, and the lowest feasible temperature of $T = 2\,\mathrm{MeV}$. The normalization of $A_{^{12}C}$ is given by

$$Z = \int \mathrm{d}^3k \int_{-\infty}^{\mu} \mathrm{d}\omega A_{^{12}C}(k,\omega). \tag{4.16}$$

$Z = 6$ is the charge number. Note that in Fig. 4.17, the spectral functions are plotted as a function of the missing energy, so that the negative energy tail extends into the direction of positive missing energies. At low momenta, the calculation is in good agreement with the data, but the agreement gets worse with increasing momentum. The theoretical spectral function tends to overshoot at high momenta and high energies. The missing strength at low momentum is probably due to long-range low-energy excitations that are not treated satisfactorily in the theory (cf. Section 2.4). In the low energy region, major effects must also be expected from the finite size of the ^{12}C nucleus.

A local density approximation for finite nuclei, derived from nuclear matter spectral functions in the CBF approach was presented by Benhar *et. al.* in Ref. [ben94]. An explicit calculation of a spectral function in ^{16}O, using a Green's functions approach, was published by Müther *et. al.* in Ref. [mut95]. These calculations were derived using completely different many-body theories, but in both cases, the hole-hole scattering was treated in a perturbative way. For a single momentum, $k = 410\,\mathrm{MeV}$, the theoretical predictions for the finite systems (rescaled to ^{12}C) are compared with the experimental result and the SCGF nuclear matter result in the right panel of Fig. 4.17. It is surprising that the nuclear matter spectral function is closer to the experimental result than the calculations for the finite system. In particular, the peak of the background distribution is shifted to lower

missing energies and the slope at high energies is better reproduced. This could be a sign that a sophisticated treatment of hole-hole scattering, as it is done in the T matrix approach, is indeed important to describe correlations in nuclear systems correctly. To finally answer this question, a calculation in a finite nucleus should be performed.

4.5 Momentum Distributions

Momentum distributions are computed from the spectral functions according to Eq. (3.14). *Correlated* momentum distributions at *finite temperature* are distorted by two different effects with respect to the box-like distribution of the uncorrelated zero-temperature case. Both effects, the temperature effect and the correlation-induced effect, were illustrated separately in Fig. 3.2. One of the questions to be addressed in this Section is whether they can be disentangled from each other.
In Fig. 4.18, the temperature dependence and the density dependence of the momentum distributions are shown. Fig. 4.18 (a) displays the temperature dependence for a single density. The momentum distribution at $T = 0$ is computed from the self energy extrapolation. NN correlation lead to a constant depletion of the low momentum states, and a discontinuity is formed at k_F. With increasing temperature, the Fermi surface is smeared out, but for not too high temperatures, the finite temperature results merge into the extrapolated zero temperature curve in the high momentum region. This indicates that the information contained in the correlation-induced occupation of high momentum states is independent of the temperature.
Fig. 4.18 (b) shows the depletion of deeply-bound zero momentum states at saturation density, as a function of the temperature. Above $T = 10\,\mathrm{MeV}$, the depletion increases strongly with temperature. Below $T = 5\,\mathrm{MeV}$, the depletion becomes temperature independent, which means that it is induced solely by NN correlations. The extrapolated value for the depletion of zero momentum states at $T =$ MeV is $d(0) = 10.6\%$. This corresponds to a partial occupation of 89.4%.
Momentum distributions derived from different realistic NN potentials have been calculated by several authors, using different many-body techniques. Fantoni and Pandharipande showed that tensor components in the two-body force account for a large fraction of the depletion [fan84]. Potentials with strong tensor components are therefore likely to produce more depletion. Benhar, Fabrocini and Fan-

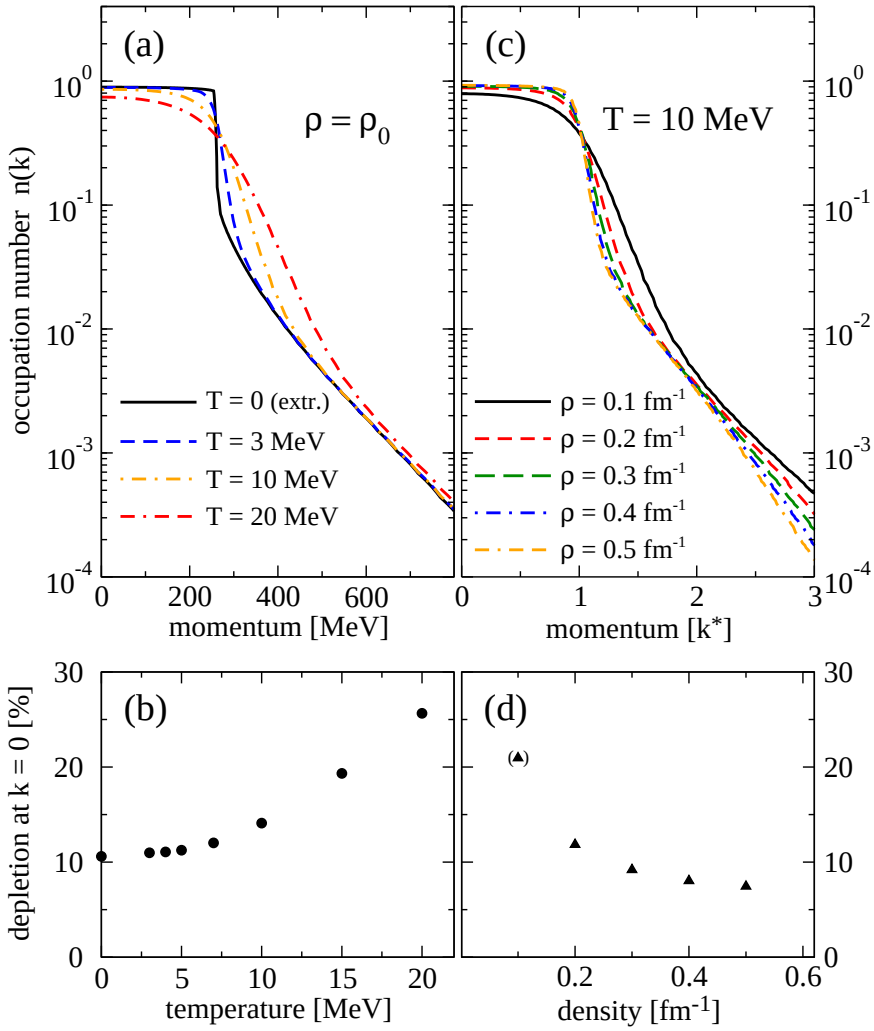

Figure 4.18: *Momentum distributions and depletion of deeply bound states. (a) Temperature dependence of the momentum distribution at saturation density. The solid line is the zero temperature momentum distribution, obtained from an extrapolated spectral function. (b) Temperature dependence of the depletion of the zero momentum states. (c) Density dependence of the momentum distributions at a constant temperature of $T = 10\,MeV$. To obtain comparable results, all curves have been divided by the respective k^*. (d) Density dependence of the depletion for deeply bound states. The first value is given in brackets, since the high depletion at $\rho = 0.1\,\mathrm{fm}^{-3}$ is predominantly a temperature effect.*

toni used perturbation theory in a correlated basis (CBF) [ben89, ben90]. With the Urbana V14 interaction plus a three-nucleon force, they found $n(0) = 0.83$. An advanced hole-line calculation by Baldo and collaborators that includes some higher order diagrams with respect to the BHF approximation yields 0.87 for the same potential [bal90]. The result of the Paris potential, having a stronger tensor part, is $n(0) = 0.82$ in this type of Brueckner calculation. The Green's function approach by Vonderfecht *et. al.* is similar to the QPGF approximation described in Section 3.5, but a somewhat different choice for the energy spectrum was used [von91, von93]. An occupation of 0.83 is obtained for the Reid 68 potential [rei68]. Dewulf and Van Neck used a discrete parameterization of the Green's function that goes beyond a quasiparticle description [dew02]. They found an occupation of 0.88 for the updated version of the Reid potential [sto94], in which the tensor force is not as strong as in the older Reid 68 potential. Bożek used a separable version of the Paris potential in a self-consistent Green's functions approach and obtained 0.87 [boz02a].
If one compares only the Green's functions calculations, it seems that the QPGF approximation overestimates the depletion. This trend can also be observed in Fig. 4.19, where a QPGF momentum distribution is compared to the full SCGF result. While above k^*, the partial occupation is higher than for the SCGF result, it is reduced by about four percentage points for low momenta. The reduction of the depletion is due to the dressing of the propagators in the intermediate states. Since the occupation of low momentum states is less than unity in the SCGF ladder equation, nucleons can also be scattered in these normally occupied states and the depletion effect is softened as a direct effect of self-consistency.
Generally, Green's functions results that include dressing of the intermediate states yield less depletion than the results that are derived from CBF or Brueckner theory. The soft tensor components of the CDBONN potential account for the remarkably low depletion in the SCGF calculation in this Thesis. This is corroborated by a calculation with the stiffer Argonne V18 potential, which reduces the occupation number by two percentage points.
The occupation numbers of the deeply bound states can be compared to the spectroscopic factors for low-lying single-particle states in ^{208}Pb. Because the depletion of these states is due to SRC, the finite size of the nucleus should not play an important role. Experimental numbers have been derived from an analysis of (e,e'p) scattering experiments [bat01]. A statistically weighted average of the spectroscopic factors of the five deepest bound proton orbits, $1s_{1/2}$, $1p_{1/2}$, $1p_{3/2}$,

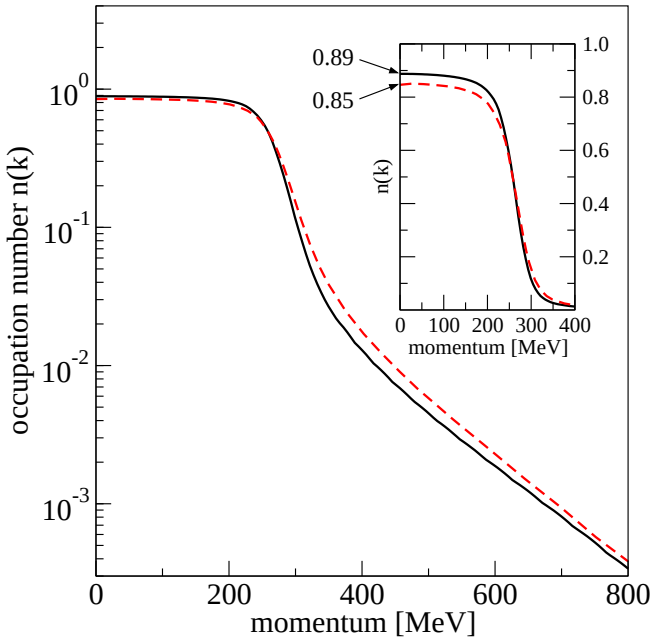

Figure 4.19: *Comparison between a quasiparticle momentum distribution and the full momentum distribution at a temperature of $T = 5$ MeV and saturation density. The inset displays the depletion of the bound states in both schemes.*

$1d_{3/2}$ and $1s_{5/2}$, yields a mean value of $Z_{deep} = 0.78 \pm 0.08$, which means that the experimentally observable strength is significantly lower than the self-consistent Green's functions results. The analysis is based on a model for a state-dependent fragmentation of strength and partly, the error bars are due to the rather large model-dependence. Furthermore, the spectroscopic factors for the individual states are quite different. Considering only the $1s_{1/2}$ or only the $1p$ protons, the spectroscopic factor is $Z_{1s} = 0.87 \pm 0.12$ and $Z_{1p} = 0.81 \pm 0.13$, respectively.
The density-dependence of $n(k)$ is discussed in the subsequent part of this section. Calculations were performed for five different densities, assuming a temperature of $T = 10$ MeV. In Fig. 4.18 (c), the results are shown as a function of k/k^*. It is clear from the discussion of the temperature dependence that information related to the correlation induced effects should be extracted from the high-momentum region or the the deeply bound states. However, one must be careful with that argument in the low density regime. A temperature of 10 MeV at the lowest den-

ρ [fm^{-3}]	T [MeV]	a [fm^{-5}]	b [fm]
0.1	10	4.61	2.02
0.16	0	12.1	1.71
0.16	10	12.1	1.71
0.2	10	16.0	1.63
0.3	10	19.4	1.58
0.4	10	21.0	1.55
0.5	10	20.7	1.55

Table 4.5: *Parameterization of the momentum distribution in the range between $2k^*$ and $3k^*$. The Table lists the fitting constants a and b that are defined in Eq. (4.17). The temperature at which the respective calculation was performed is also given.*

sity of $\rho = 0.1\,\mathrm{fm}^{-3}$ causes already quite a strong distortion (compare the solid line in Fig. 4.18 (c) with the temperature dependent curves in Fig. 4.18 (a)). The momentum distributions at higher densities are more degenerate.
In the high momentum region, between $2k^*$ and $3k^*$, an exponential of the form

$$n(k) = \frac{{k^*}^5}{a} e^{-bk} \tag{4.17}$$

was fitted to the tail of the momentum distributions, following a suggestion of Baldo and collaborators for a density-independent parameterization of the high-momentum tail in an advanced Brueckner type calculation [bal90]. The fitting constants a and b are given in Tab. 4.5. The parameterization is applicable and the density independence is rather well fulfilled at high densities, whereas the low density results show a strong deviation. Note that the extrapolated result at zero temperature follows this trend. This shows that the effect is not due to the incipient temperature distortion — the parameters a and b are just not density-independent in the SCGF approach. The mean values for the three highest densities are $a = 1.56\,\mathrm{fm}^{-5}$ and $b = 20.3\,\mathrm{fm}$. Baldo *et. al.* obtained $a = 1.6\,\mathrm{fm}^{-5}$ and $b = 7\,\mathrm{fm}$ for the Paris interaction.
A decrease of correlation induced depletion of the zero momentum states with increasing density can be inferred from Fig. 4.18(d). Around three times saturation density, the occupation of zero momentum states is 92.6%. Remember that the zero temperature result at ρ_0 was almost three percentage points less. This is a

surprising result, because intuitively, one would expect the importance of correlations and correlation-induced depletion to increase with density. In particular, $n(0)$ should tend to unity for $\rho \to 0$. The calculations that can be found in literature provide an ambiguous picture. A CBF calculation at nuclear matter densities below ρ_0 was performed by Benhar *et. al.* in Ref. [ben94]. They found a roughly density-independent depletion at low momenta and assigned this behavior to the attractive components in the nuclear interaction. The attraction leads to the formation of correlated pairs or in-medium deuterons. Since the deuteron formation is favored at low densities, it could explain the strong depletion at densities below ρ_0. In the quasiparticle Green's functions calculation presented in the thesis of Schnell [snl96], a simple non-realistic potential was used. Like in the present work, a decrease of the depletion in the range between $0.5\rho_0$ and $1.5\rho_0$ was found. These results are in contrast to the findings of Ramos *et. al.* [ram89]. In their quasiparticle Green's functions calculation, a noticeable increase of the depletion was observed at densities above ρ_0. It is interesting to comment on the fact that a truncated potential was applied in this work. To prevent pairing effects that would lead to the kind of instabilities that have been described in Section 4.2, only the central components of the Reid 68 potential were taken into account, and only S-waves were kept. The resulting interaction is purely repulsive and does not yield a bound two-nucleon state any more.
At three times nuclear matter saturation density, deuteron formation is not very likely. The density dependence of the depletion should therefore be further investigated.

4.6 Nuclear Matter Saturation

It is impossible to determine the properties of symmetric nuclear matter from a direct experiment, because a homogeneous system of an equal number of protons and neutrons (and electrons, that are necessary to guarantee charge neutrality) is unstable against weak electron capture. Due to its simple structure, nuclear matter has nevertheless been a popular testing ground for nuclear many-body calculations for more than 50 years, and therefore, nuclear matter 'observables' that can be compared with the results of theoretical calculations have been deduced by other means. A semi-empiric number can be extracted from experimentally determined binding energies in finite nuclei: since in nuclear matter, the coulomb repulsion

is turned off and there are no surface or asymmetry effects present, the binding energy per nucleon must be equal to the coefficient of the volume term in the Bethe-Weizsäcker mass formula [bet36, wei36]. The coefficients in this empirical relation have been fitted to the binding energies of all stable nuclei. The size of the volume term is:

$$\frac{E_0}{A} = a_V = -15.67\,\mathrm{MeV}. \tag{4.18}$$

Electron scattering experiments on nuclei are sensitive to the proton charge distribution, from which the nuclear density profile of can be deduced [fro77]. The central density of the heavy nuclei is only very weakly dependent on the mass number A, and the density of nuclear matter is obtained by extrapolating to $A \to \infty$,

$$\rho_0 = 0.16\,\mathrm{nucleons} \times \mathrm{fm}^{-3}. \tag{4.19}$$

The central density of ^{208}Pb amounts to more than 90% of that value. The constant density is a characteristic property of a saturating system that can be found in all liquids. Apart from surface effects, the density of water inside a tiny drop, e.g., is the same as in an ocean. Both in a nuclear system and in chemical liquids, there are short-range attractive forces that are counterbalanced by very strong and even shorter-range repulsive forces. Unlike for the infinite-range electromagnetic or gravitational potentials, the attractive components of the individual constituents cannot add up to overcompensate the repulsion and will never cause to a collapse when the system size grows. Instead, an equilibrium is realized. The binding energy per nucleon, E_0/A, and the nuclear saturation density, ρ_0, define the nuclear saturation point, which is a free energy minimum for zero temperature. Density fluctuations around the saturation density ρ_0 reduce the binding energy: an additional compression leads to an enhanced repulsion due to the overlapping core regions, and when the system is diluted, the particles do not feel their mutual attraction any more.
The semi-empirical nuclear saturation point is an important observable to be compared with the results of nuclear matter calculations. In a computer code, ρ serves as an input parameter that can be easily varied in a certain range to find out whether the system saturates at the correct density. The relation between density and nuclear binding energy is often referred to as equation of state. It is a well-known problem that, up to now, all non-relativistic nuclear many-body calculations fail to reproduce the correct saturation point, no matter what two-body potential

is used as an input. Stiff potentials, that are characterized by a strong repulsive core, usually saturate around the correct density, but do not produce enough binding energy. In contrast, potentials like the CDBONN potential provide enough or even too much binding energy, but their soft cores yield too dense systems. In this way, an increase in binding energy is accompanied by an increase of the saturation density, as was first pointed out by Coester and collaborators [coe70]. An improved description of the saturation properties using two-body forces only, has been achieved with relativistic Dirac-Brueckner-Hartree-Fock calculations [mac89]. By introducing a three-body force that provides additional attraction in dilute systems and repulsion at high densities, the nuclear saturation point can also be met [wir88, gra89]. It is nevertheless important to study the saturation properties of the sophisticated non-relativistic SCGF many-body approach that is based on a two-body Hamiltonian.
In the finite temperature Green's functions theory approach, the internal energy for symmetric nuclear matter in thermodynamic equilibrium can be calculated from the spectral function with Koltun's sum rule [fet71],

$$\frac{E_{SCGF}}{A} = \frac{\gamma}{\rho} \int \frac{\mathrm{d}^3k}{(2\pi)^3} \int_{-\infty}^{+\infty} \frac{\mathrm{d}\omega}{2\pi} \frac{1}{2} \left(\frac{k^2}{2m} + \omega \right) A(k,\omega) f(\omega). \tag{4.20}$$

$\gamma = 4$ is the spin-isospin degeneracy factor. The BHF result for the internal energy per particle is

$$\frac{E_{BHF}}{A} = \frac{\gamma}{\rho} \int \frac{\mathrm{d}^3k}{(2\pi)^3} \frac{1}{2} \left(\frac{k^2}{2m} + \epsilon(k) \right) f(\epsilon(k)). \tag{4.21}$$

This expression is obtained from Koltun's sum rule, Eq. (4.20), using the quasiparticle form of the spectral function (the Delta spike) and the definition of the BHF quasiparticle energy,

$$\epsilon(k) = \frac{k^2}{2m} + \Sigma^{BHF}(k). \tag{4.22}$$

In Fig. 4.20, the internal energy per particle is plotted vs. the density between $\rho = 0.1\,\mathrm{fm}^{-3}$ and $\rho = 0.5\,\mathrm{fm}^{-3}$. The results of the full SCGF calculation, computed at a temperature of $T = 10\,\mathrm{MeV}$, are indicated by the circles that are connected by a solid line. Two curves from a continuous choice BHF calculation are given: at the same temperature, and — to illustrate the size of the temperature effect

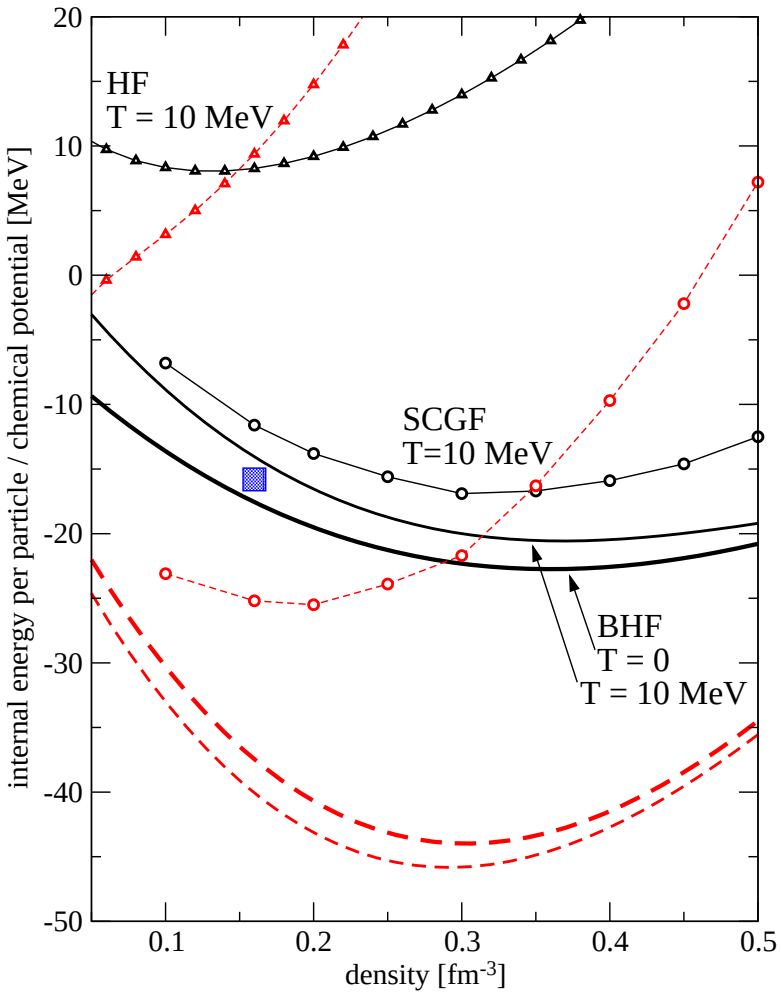

Figure 4.20: *The internal energy per nucleon (solid lines) and the chemical potential (dashed lines) as a function of the density of the system at a temperature of* 10 *MeV. The full SCGF calculation (circles) is compared to BHF calculations (thin solid lines). To illustrate the size of the temperature effect, the zero temperature BHF result is also given (thick solid lines). The result of a HF calculation is reported, too (lines with triangles). The semi-empirical saturation point is indicated by the big square. Note that the Hugenholtz-Van Hove theorem is well fulfilled in the HF and the SCGF approximation, while it is badly violated in the BHF approach.*

— at $T = 0$. The BHF results are indicated by the thick and the thin solid lines, respectively. For comparison, the HF result is also reported (triangles and solid line). The empirical saturation point is given by the big square.
An overall repulsive effect in the full T matrix calculation, compared with the BHF calculation at the same temperature can be observed. The repulsive effect increases with density. It can be assigned to the hole-hole scattering contributions that are neglected in the BHF approximation. The relative importance of the hole-hole scattering terms to the total energy grows, because the accessible phase space for the holes increases with density. Due to this effect, the saturation density in the SCGF approximation, $\rho_{sat} = 0.31\,\mathrm{fm}^{-3}$, is slightly smaller than the saturation density in the BHF approach. However, this value is still almost twice as large as the empirical saturation density ρ_0.
It was argued in Ref. [dew03] that the repulsive effect due to the inclusion of the hole-hole scattering might be able to shift the saturation point close to the empirical value. An obvious, although not the only possible interpretation of this statement is, that short-range correlations alone — because they are taken into account most efficiently by the ladder approximation — are able to describe the mechanism of nuclear saturation correctly. Although one has to keep in mind that the results that are displayed in Fig. 4.20 are calculated at finite temperature, they show that such a statement is much too strong for the CDBONN potential. The findings of Bożek and Czerski [boz03], who use a separable version of the CDBONN potential point into the same direction. Dewulf and Van Neck used an iterative scheme in which the energy dependence of the spectral function $A(k, \omega)$ for a given momentum k is approximated by three Dirac functions [dew02]. They carried out an analysis for different NN potentials and found a systematic, but only moderate reduction of the saturation density.
It must be emphasized that there is a variety of effects that are not considered on the level of the T matrix approximation. Some of these effects will probably alter the saturation properties presented here. Other classes of self energy diagrams, like the ring diagrams, some of which are shown in Fig. 2.6, excitations of internal nuclear degrees of freedom like the $\Delta(1232)$, relativistic extensions to the theory or genuine three-body forces should be included in a full picture of nuclear matter saturation. Much more work needs to be done to settle the issue of reproducing the nuclear saturation point.
A nice property of the SCGF approach is its thermodynamic consistency. In particular, it fulfills the Hugenholtz-Van Hove theorem, which states, that whenever a

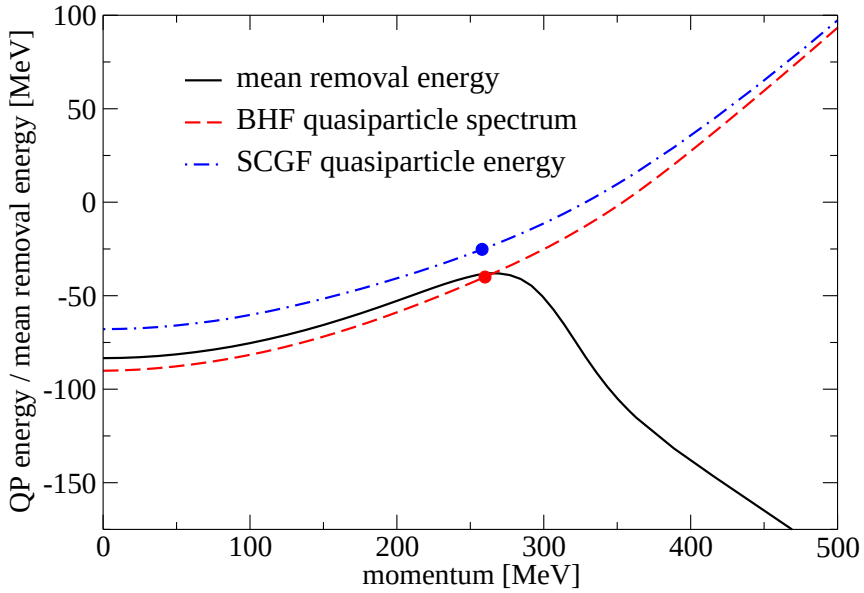

Figure 4.21: *Mean removal energy (solid line) vs. BHF quasiparticle energy (dashed line). The dash-dotted line is the SCGF quasiparticle spectrum. Note the kink in the mean removal energy for momenta greater than k^*. The dots indicate the chemical potentials. The calculation was performed at $T = 5\,MeV$ and $\rho = 0.16\,fm^{-3}$.*

further nucleon is added to the nuclear system in equilibrium, i.e. at the saturation point, the energy gain is exactly the binding energy of a nucleon [hug58],

$$\mu = \frac{E_{sat}}{A}. \tag{4.23}$$

Strictly speaking, this theorem is only valid at zero temperature, where the Fermi surface is well defined. In Fig. 4.20, the chemical potentials, that correspond to the three binding curves discussed above, are given by the dashed lines. The violation of the theorem in the zero temperature continuous choice BHF calculation amounts to about 20 MeV, and is exceeded by about 10% at a temperature of 10 MeV. The SCGF calculation shows only a small violation. Although a zero temperature calculation was not performed, one can conclude that a good thermodynamic consistency is achieved. This findings agree with the results that were obtained in the Krakow group [boz01] and the Gent group [dew02].
To understand the drastic difference between the chemical potential in the two

	k^*	$2k^*$	$3k^*$	$4k^*$	$5k^*$
E_{tot}/A	84	95	99.8	100.1	100.0
E_{kin}/A	44	80	93.6	99.0	99.9
E_{pot}/A	56	84	95.5	99.3	99.9

Table 4.6: *Contributions to the internal energy, the kinetic energy and the potential energy per particle. The numbers represent the fractions of the final value (in %) for a given upper integration limit.* k^* *is* $263\,MeV$. *The temperature is* $T = 5\,MeV$ *and the density is* $\rho = 0.16\,fm^{-3}$.

pictures, while the binding energy differs by only a few MeV, we have to examine the mechanism of saturation in nuclear matter in more detail. It was pointed out in Section 4.3, that the internal energy in the SCGF approach cannot be calculated from the quasiparticle energy. Instead, by defining the mean removal energy [boz02b],

$$\bar{\omega}_r(k) = \frac{1}{n(k)} \int_{-\infty}^{+\infty} \frac{\mathrm{d}\omega}{2\pi}\, \omega A(k,\omega) f(\omega), \tag{4.24}$$

Koltun's sum rule, Eq. (4.20), can be reformulated in the following way,

$$\frac{E_{SCGF}}{A} = \frac{\gamma}{\rho} \int \frac{\mathrm{d}^3k}{(2\pi)^3} \frac{1}{2} \left(\frac{k^2}{2m} + \bar{\omega}_r(k) \right) n(k). \tag{4.25}$$

It is the mean removal energy that determines the binding energy in the SCGF picture. $\bar{\omega}_r$ is plotted, together with the SCGF and the BHF quasiparticle energies, in Fig. 4.21. For small momenta, $\bar{\omega}_r$ is more repulsive than the corresponding BHF spectrum, but much more attractive than the SCGF quasiparticle spectrum. Above k^*, it displays a noticeable kink and goes to very negative values. In this way, the binding energies in the BHF and the SCGF picture differ by only 2 MeV at $T = 5\,\mathrm{MeV}$ and $\rho = 0.16\,\mathrm{fm}^{-3}$. In contrast, in both pictures, μ is determined by the quasiparticle energy, as can be seen from the denominator of Eq. (3.11). The chemical potentials are indicated by the two dots in Fig. 4.21. They have a distance of about 15 MeV. This shows why the Hugenholtz-Van Hove theorem can be fulfilled.

The strongly attractive mean removal energy above k^* and the finite occupation of high-momentum states suggest that there are non-negligible contributions to the

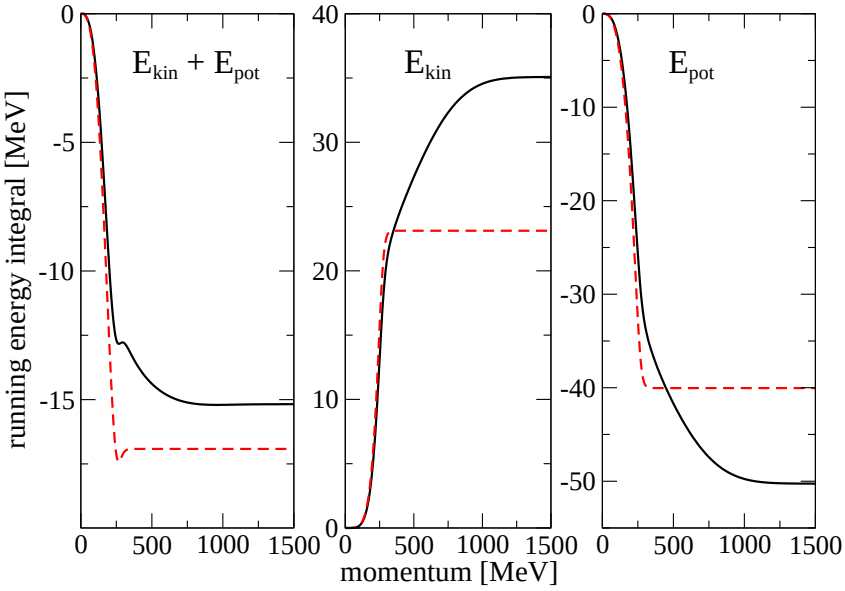

Figure 4.22: *The running integral illustrates the saturation of the kinetic energy, the potential energy and the binding energy per particle in the SCGF picture (solid line) and in the BHF picture (dashed line). The calculation was performed at* $T = 5\,MeV$ *and* $\rho = 0.16\,fm^{-3}$.

internal energy from nucleons in these states. This is illustrated in the left panel of Fig. 4.22, where the running integrals of Eqs. (4.25) and (4.21) over a sphere in momentum space are plotted. While the BHF integral saturates quickly above k^*, an attractive contribution of more than 2 MeV from states between k^* and $3k^*$ is observed in the SCGF result. The internal energy can be split in a kinetic part,

$$\frac{E_{kin}}{A} = \frac{\gamma}{\rho}\int \frac{\mathrm{d}^3k}{(2\pi)^3}\frac{k^2}{2m}\,n(k). \tag{4.26}$$

and a remaining contribution, which is interpreted as the potential part,

$$\frac{E_{pot}}{A} = \frac{\gamma}{\rho}\int \frac{\mathrm{d}^3k}{(2\pi)^3}\frac{1}{2}\left(\bar{\omega}_r(k) - \frac{k^2}{2m}\right)n(k). \tag{4.27}$$

The saturation of the running integrals for these expressions are compared with the corresponding BHF results in the middle and the right panel of Fig. 4.22. The absolute value of the kinetic and the potential part in the SCGF picture are 12 MeV and 10 MeV greater than the BHF results. As much as 56% of the kinetic

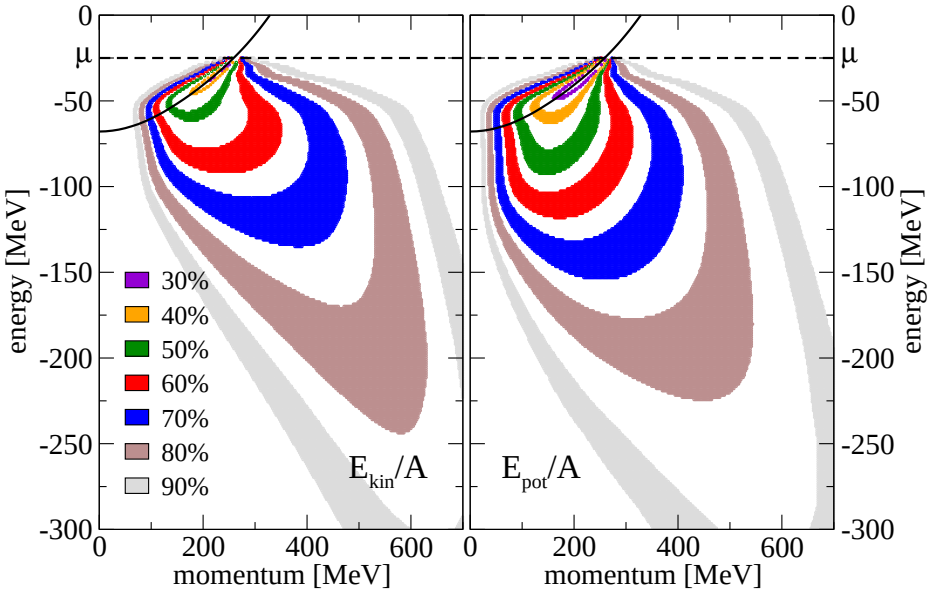

Figure 4.23: *Distribution of the kinetic energy contributions (left panel) and the potential energy contributions (right panel) in the energy-momentum plane. The regions inside the various bands contain a contribution of 90%, 80%, 70%, 60%, 50%, 40% and 30% to the total integral. The solid line is the SCGF quasiparticle energy. The data were obtained using the extrapolation of the self energy to zero temperature at nuclear matter saturation density, $\rho = 0.16\,fm^{-3}$. The chemical potential is $\mu = -25\,MeV$ (dashed line).*

energy and 44% of the potential energy are from off-shell nucleons in high momentum states as can be seen from Tab. 4.6. Only after integrating up to $5k^*$, E_{kin}/A and E_{pot}/A are fully converged.

The strength of a state k is fragmented according to the spectral function, and so one can not only look for the momentum regions that contribute to the kinetic energy and the potential energy, but also for the respective energy domains. In Fig. 4.23, the region that is enclosed by one of the bands represents the smallest possible area in the energy-momentum plane that contributes a given percentage to the total kinetic energy (left panel) and potential energy (right panel). For the present analysis, the zero temperature spectral function that was derived from the extrapolation procedure (cf. Section 4.3) was inserted into the kinetic and

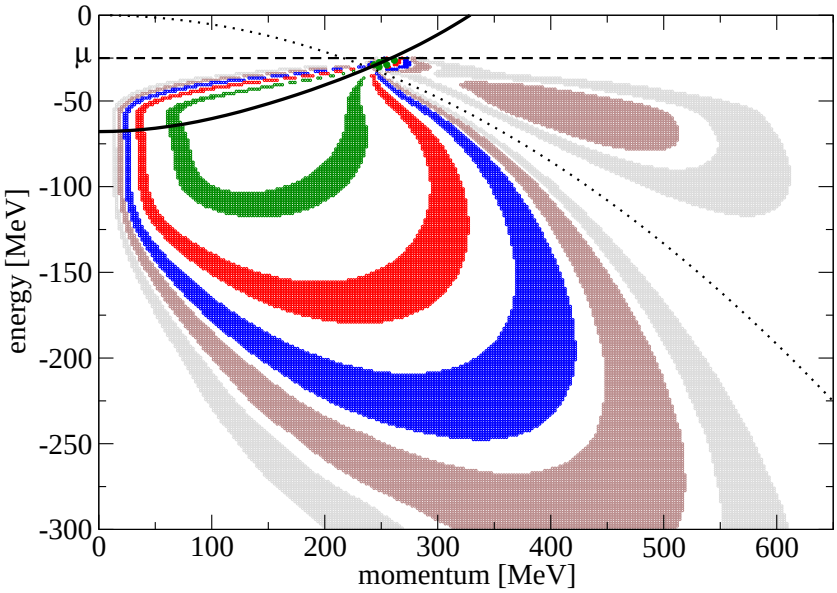

Figure 4.24: *Positive and negative contributions to the binding energy in the energy-momentum plane. Bands of the same color code indicate contributions of equal absolute size (attractive below the dotted line and repulsive above). The straight line marks the SCGF quasiparticle energy and the chemical potential is indicated by the horizontal dashed line. The parameters are the same as in Fig. 4.23.*

the potential contribution to Eq. (4.20). At zero temperature, only energies up to $\omega = \mu$, the chemical potential, can contribute to the integral. About $40\% - 50\%$ of the kinetic and the potential energy is concentrated in the quasiparticle region. The rest is spread over the low energy – high momentum region. Both plots look similar, however, the bands are deformed into the direction of high momentum rather than into the direction of low energy in the case of the kinetic energy and vice versa for the potential energy.

The contributions to the kinetic energy are positive everywhere in the energy-momentum plane, while those to the potential energy is always negative. In Fig. 4.24, the sum of both distributions is shown. Each band indicates a region with a contribution of equal absolute size to the internal energy. The dotted line is determined by the condition:

$$\frac{k^2}{2m} + \omega = 0 \tag{4.28}$$

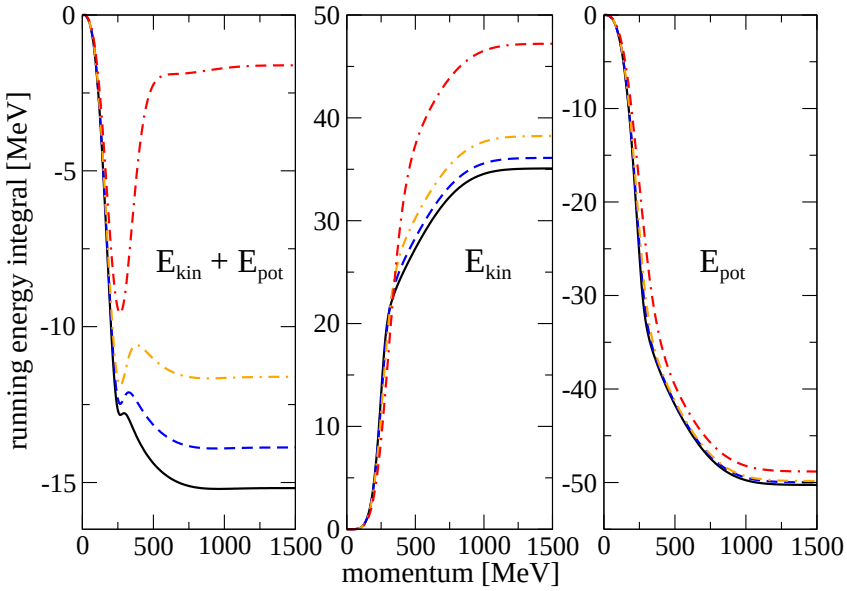

Figure 4.25: *The running integral illustrates the saturation of the kinetic energy, the potential energy and the binding energy per particle for* $T = 5\,MeV$ *(solid line),* $T = 7\,MeV$ *(dashed line),* $T = 10\,MeV$ *(dash-dotted line) and* $T = 20\,MeV$ *(double-dash-dotted line). All calculations were done at saturation density.*

The left hand side is the weighting factor of Koltun's sum rule, which means, that below the dotted line, the distribution is attractive, above, it is repulsive. The contribution of a momentum state $k = 600\,\mathrm{MeV}$ is repulsive down to energies of $-200\,\mathrm{MeV}$, nevertheless, the net contribution of the state to the binding energy is attractive (cf. left panel of Fig. 4.22). This illustrates the role of the negative energy tail of the spectral function for the nuclear binding energy.
Finally, the temperature dependence of the running integral is studied. Like in Fig. 4.22, the internal energy, the kinetic energy and the potential energy at saturation density are displayed separately in Fig. 4.25. A strong repulsive effect in the internal energy can be observed, which is roughly proportional to T^2. (a closer analysis shows that the exact temperature dependence of the kinetic energy cannot be given in a simple analytic form even for free particles). The potential energy depends only very weakly upon the temperature (right panel). Almost the complete repulsion is induced by an increasing kinetic energy (middle panel). This is due to the thermal excitation of on-shell particles in a narrow momentum inter-

val above k^*. The results for temperatures up to 10 MeV in the left panel show that the high momentum off-shell nucleons above $k \approx 500$ MeV provide attraction. However, at $T = 20$ MeV, also the off-shell nucleons yield a repulsive contribution.

Chapter 5

Summary and Conclusions

Based on recent (e,e'p) knock-out experiments in finite nuclei, experimentalists are now able to pin down the role of short-range NN correlations on a quantitative level. The shell-model states below the Fermi energy are not fully occupied, and the missing strength is redistributed to high momenta. Both from the experimental and from the theoretical point of view, the spectral function is the key quantity to study the properties of nucleons that are moving in the nuclear medium.

Among other many-body approaches, the theory of Green's function provides a particularly suitable framework to determine the spectral function. The Green's function describes the propagation of a nucleon in the many-body system. Along its path, a particle collides with the particles in the surrounding medium, which, in turn, alter the particles' own properties from those in free space. The nucleon self energy accounts for these medium-modifications. There is an obvious aspect of recursivity in this situation, since the same kind of self-modification must apply for all particles in the medium. A solution to the many-body problem must therefore be self-consistent in this regard.
In this work, a fully self-consistent solution for symmetric nuclear matter at finite temperature has been obtained in the T matrix approximation: to some extent, it is justified to consider nuclear matter as a dilute system, because the range of the interaction is shorter than the mean interparticle distance. In a low density system, the successive exchange of several bosons between only two nucleons is more likely than the simultaneous participation of three or more nucleons in a collision process. The multiple-scattering process between the dressed fermions

modifies their relative wave function in such a way that their repulsive cores do not overlap. By taking into account these correlations in terms of an effective interaction, realistic NN potentials can be applied. In a mean-field picture, where correlations are neglected and the nucleons move in a potential that is averaged over the Fermi sea, the use of realistic NN forces would never lead to satisfying results. Partial summation over ladder diagrams to all orders leads to a Lippmann-Schwinger type of equation for the energy-dependent T matrix or, alternatively, to the Brueckner G matrix, both of which can be interpreted as effective in-medium interactions.
The central improvement concerning the matter of self-consistency in this Thesis is that the intermediate nucleon pair in the ladder equation is described by a product of two full in-medium Green's functions. This object takes into account forward (particle-particle) and backward (hole-hole) propagation of the NN pair. By assuming a propagation on the energy shell (quasiparticle approximation) and by neglecting the backward propagation, the ladder equation for the T matrix reduces to the familiar Bethe-Goldstone equation.

For the first time, the self-consistent Green's function has been computed from the T matrix without any approximation apart from the angle-averaging of the two-particle propagator in the ladder equation. In previous studies that go beyond the quasiparticle approximation, either the self energy or the spectral function was parameterized, or the T matrix was determined for separable potentials only.
At finite temperature, the numerical solution has been obtained with an iterative procedure that leads to very stable results at finite temperatures. The realistic CD-BONN potential was applied. In the discussion of the self-consistent results for the T matrix, special attendance was paid to the differences between the quasiparticle picture and the full solution: artificial phase space restrictions in the quasiparticle scheme lead to a lower bound for the total energy of the scattered NN pair, whereas the full solution extends to more negative energies.
The phase transition to a superfluid states below a critical temperature is a well-known phenomenon in Fermi liquids. Calculations in the superfluid phase cannot be performed in the T matrix approach, but precursor effects for the phase transition have been studied. In the full SCGF solution, they are weaker than in the quasiparticle scheme and it was found that T_C is overestimated in a quasiparticle description. In the SCGF scheme, the critical temperature was not reached in the temperature and density range that could be covered.
The energy dependence and the density dependence of the imaginary part of the

nuclear self energy have been discussed thoroughly. Since a direct calculation at zero temperature is not possible with the implemented iteration procedure, an extrapolation scheme has been developed. An extrapolation of the results to zero temperature is most easily done on the level of the self energy, because of its rather smooth energy dependence.
The spectral function of a correlated system is composed of a peak and a broad background distribution that extends to very high positive energies and displays also a negative energy tail. In contrast to the zero temperature case, the hole and the particle part of the spectral function are not separated at $\omega = \mu$ at finite temperature. Compared to spectral functions that were obtained in a quasiparticle picture, the negative energy tail of the self-consistent results is smoother and extends to more negative energies. Generally, the agreement between the quasiparticle and the self-consistent spectral function becomes better at high momenta. Self-consistent spectral functions in hot and dense nuclear matter can be applied in microscopic simulations of heavy-ion collisions or supernova explosions. It was found that the spectral functions at finite temperature differ from the zero temperature result mainly in a temperature dependent energy interval around the chemical potential, leading to a temperature broadening of the quasiparticle peak for the loosely-bound states. Investigating the density dependence of the on-shell width at a single temperature, one finds an increasing width for deeply bound states and a sharpening peak for states at the Fermi edge.
A nuclear matter spectral function, calculated at the mean density of ^{12}C has been compared to an experimental spectral function for this nucleus. The results describe the data surprisingly well, especially for momenta up to twice the Fermi momentum. For even higher momenta, the energy tail of the theoretical curves overshoots the data, and the strength at low energies is underestimated. The SCGF results have also been compared to recent theoretical spectral functions for finite systems. The deviations to the experimental result are similar in all models, but the T matrix results yields the best description, which can be seen as a hint that the self-consistent dressing of the Green's function is important. However, to draw further conclusions, an explicit calculation for the finite system should be made, using dressed Green's functions.
The effect of short-range correlations on the momentum distributions has also been investigated in this Thesis. SRC lead to a constant depletion of low momentum states with respect to the Fermi-Dirac distribution, and, in turn, high momentum states up to five times the Fermi momentum are partially occupied. The

temperature-induced softening effect on $n(k)$ is limited to momenta up to only two times the Fermi momentum in the temperature range that was considered. The total depletion of the deeply bound states that has been computed within the framework of self-consistent Green's functions is only about half of the value that was measured recently in an (e,e'p) experiment on ^{208}Pb. Other many-body theories, as the theory of correlated basis functions, are closer to the experimental value. However, the experimental error bars are still quite large.
A somewhat surprising result is the decrease of the depletion at high densities, between ρ_0 and $3\rho_0$. In previous studies, a similar dependence was found at lower densities and assigned to attractive correlations in the deuteron channel. Since the deuteron formation is suppressed at high densities, the origin of this effect should be further investigated.
Finally, the saturation properties of hot nuclear matter have been studied. Due to an increase in kinetic energy, the internal energy of hot nuclear matter is $5-2$ MeV higher than at zero temperature. This is due to a higher kinetic energy of the nucleons. The total effect on the internal energy is more pronounced at low densities. Compared to the result of a continuous-choice BHF calculation at the same temperature, a density dependent overall repulsive effect between 2 and 7 MeV was found, which shifts the minimum of the equation of state towards the empirical value of the saturation point. However, the saturation density is still too large (no three-body force was used in the calculation).
The difference with respect to the BHF result can be assigned to the backward propagation that is taken into account in the T matrix approach. An analysis of the contribution of the individual momentum states shows that the repulsion is due to the low momentum states. The high-momentum off-shell nucleons, and especially the strength located in the negative energy tail, provide attraction.
The Hugenholtz-Van Hove theorem states, that at zero temperature, the chemical potential must be equal to the binding energy per particle at the saturation point and it is badly violated in lowest order Brueckner theory. Although the equation of state has only been computed at finite temperature, we can conclude that the theorem is well satisfied.

The results of this Thesis show that the fingerprints of correlations in nuclear systems can be described within the self-consistent Green's functions approach. As far as experimental data are available, the results agree well on a qualitative level. It should be stressed that the theory contains no free parameters that can be used to fit experimental or semi-experimental data as the nuclear saturation point. One

should also keep in mind that in nuclear systems, there are a variety of additional phenomena that can play a role, as to mention further self energy contributions from long-range correlations, internal excitations of nucleons or relativistic effects, none of which have been taken into account in the present approach. Probably one of the major achievements of this work is the conceptually consistent treatment of the non-relativistic nuclear many-body problem. It can be considered as a solid starting point for further investigations that aim on a more quantitative description of the available data. A possible project that points into the direction of a realistic description of hadronic neutron star matter would be the extention of the formalism to hot asymmetric or hyperonic matter.

Appendix A

Expansion of the Green's Function

As for the zero temperature case, there exists a diagrammatic expansion of the finite temperature single-particle Green's function in terms of unperturbed Green's functions. The Feynman diagrams provide some insight into the structure of the approximations being made. Each approximation scheme corresponds to a certain class of diagrams. For the finite temperature case in an equilibrium system, the structure of the single-particle Green's function that was given by Eq. (2.2) must be studied,

$$\mathrm{i}g(\mathbf{x}t;\mathbf{x}'t') = \frac{\mathrm{Tr}\{e^{-\beta(H-\mu N)}\mathbb{T}[\psi(\mathbf{x}t)\psi^\dagger(\mathbf{x}'t')]\}}{\mathrm{Tr}\{e^{-\beta(H-\mu N)}\}}, \tag{A.1}$$

The time arguments t and t' are chosen to be imaginary. The denominator of Eq. (A.1) is the grand partition function of the system, Z, that can also be expressed in terms of the thermodynamic potential Ω,

$$Z = e^{-\beta\Omega}. \tag{A.2}$$

The Hamiltonian of the system of interacting nucleons is given by

$$H = H_0 + H_1 = \int \mathrm{d}^3x\, \psi^\dagger(\mathbf{x}t)T(\mathbf{x})\psi(\mathbf{x}t) + \frac{1}{2}\int \mathrm{d}^3x \int \mathrm{d}^3x'\, \psi^\dagger(\mathbf{x}t)\psi^\dagger(\mathbf{x}'t)V(\mathbf{x},\mathbf{x}')\psi(\mathbf{x}'t)\psi(\mathbf{x}t), \tag{A.3}$$

where the field operators are expressed in the Heisenberg picture. The well-known textbook relation between operators in the Schrödinger picture and in the Heisenberg picture can be formally continued to imaginary times [fet71]. The time evolution of the Heisenberg operators is governed by the full Hamiltonian,

$$\hat{O}_H(\mathbf{x}t) = e^{\mathrm{i}tH}\hat{O}_S(\mathbf{x})e^{-\mathrm{i}tH}, \tag{A.4}$$

while H_0 determines the evolution of operators in the inteaction picture

$$\hat{O}_I(\mathbf{x}t) = e^{\mathrm{i}tH_0}\hat{O}_S(\mathbf{x})e^{-\mathrm{i}tH_0}. \tag{A.5}$$

It follows that operators in the interaction picture and the Heisenberg picture are related by the transformation

$$\hat{O}_H(\mathbf{x}t) = \mathbb{U}(0,t)\,\hat{O}_I(\mathbf{x}t)\,\mathbb{U}(t,0). \tag{A.6}$$

$\mathbb{U}$ is the evolution operator,

$$\mathbb{U}(t,t') = e^{\mathrm{i}tH_0}e^{-\mathrm{i}(t-t')H}e^{-\mathrm{i}t'H_0}. \tag{A.7}$$

$\mathbb{U}$ is not unitary for imaginary times, but it obeys the group property and a differential equation,

$$\mathrm{i}\frac{\partial}{\partial t}\mathbb{U}(t,t') = -H_1(t)\,\mathbb{U}(t,t'). \tag{A.8}$$

The time dependence of $H_1(t)$ is given by Eq. (A.5); note that the subscript I is omitted. The formal solution to this differential equation is

$$\mathbb{U}(t,t') = \sum_{n=0}^{\infty}\frac{(-\mathrm{i})^n}{n!}\int_t^{t'}\mathrm{d}t_1\cdots\int_t^{t'}\mathrm{d}t_n\mathbb{T}[H_1(t_1)\cdots H_1(t_n)] \tag{A.9}$$

With the evolution operator $\mathbb{U}$, the numerator of the statistical operator, $e^{-\beta(H-\mu N)}$, is expressed as

$$e^{-\beta(H-\mu N)} = e^{-\beta(H_0-\mu N)}\mathbb{U}(-\mathrm{i}\beta,0). \tag{A.10}$$

Using Eq. (A.9) and Eq. (A.10), the grand partition function can be expanded as follows:

$$\begin{aligned} e^{-\beta\Omega} &= \mathrm{Tr}\,e^{-\beta(H-\mu N)} \\ &= e^{-\beta\Omega_0}\sum_{n=0}^{\infty}\frac{(-\mathrm{i})^n}{n!}\int_0^{-\mathrm{i}\beta}\mathrm{d}t_1\cdots\int_0^{-\mathrm{i}\beta}\mathrm{d}t_n\mathrm{Tr}\{\rho_{G_0}\mathbb{T}[H_1(t_1)\cdots H_1(t_n)]\}, \end{aligned} \tag{A.11}$$

where the statistical operator of the non-interacting system has been introduced,

$$\rho_{G_0} = \frac{e^{-\beta(H_0-\mu N)}}{e^{-\beta\Omega_0}}. \tag{A.12}$$

The time-ordered Green's function can be rewritten using interaction picture field operators,

$$\mathrm{i}g(\mathbf{x}t;\mathbf{x}'t') = e^{\beta(\Omega-\Omega_0)}\mathrm{Tr}\{\rho_{G_0}\,\mathbb{T}\,[\mathbb{U}(-\mathrm{i}\beta,t)\,\psi_I(\mathbf{x}t)\,\mathbb{U}(t,t')\,\psi_I^\dagger(\mathbf{x}'t')\,\mathbb{U}(t',0)]\} \tag{A.13}$$

Inserting Eq. (A.9) into this expression, the Green's function becomes, after some combinatoric considerations [fet71],

$$\begin{aligned}\mathrm{i}g(\mathbf{x}t;\mathbf{x}'t') = e^{\beta(\Omega-\Omega_0)}\sum_{n=0}^{\infty}\frac{(-\mathrm{i})^n}{n!}\int_0^{-\mathrm{i}\beta}\mathrm{d}t_1\cdots\int_0^{-\mathrm{i}\beta}\mathrm{d}t_n \\ \times\,\mathrm{Tr}\{\rho_{G_0}\mathbb{T}[H_1(t_1)\cdots H_1(t_n)\psi_I(\mathbf{x}t)\psi_I^\dagger(\mathbf{x}'t')]\}\end{aligned} \tag{A.14}$$

The interaction picture operator H_1 can be expressed in terms of interaction picture field operators,

$$H_1(t_1) = \frac{1}{2}\int\mathrm{d}^3x\int\mathrm{d}^3x'\int_0^{-\mathrm{i}\beta}\mathrm{d}t_2\,\psi_I^\dagger(\mathbf{x}t_1)\psi_I^\dagger(\mathbf{x}'t_2)V(\mathbf{x}t_1;\mathbf{x}'t_2)\psi_I(\mathbf{x}'t_2)\psi_I(\mathbf{x}t_1), \tag{A.15}$$

where

$$V(\mathbf{x}t_1;\mathbf{x}'t_2) = V(\mathbf{x},\mathbf{x}')\,\delta(t_1-t_2). \tag{A.16}$$

Since H_1 contains four field operators, a term of order n in Eq. (A.14) contains $4n+2$ field operators. The zeroth and the first order contributions in the expansion read:

$$\begin{aligned}\mathrm{i}g(\mathbf{x}t;\mathbf{x}'t') &= e^{\beta(\Omega-\Omega_0)}\Big[\mathrm{Tr}\{\rho_{G_0}\mathbb{T}[\psi_I(\mathbf{x}t)\psi_I^\dagger(\mathbf{x}'t')]\} \\ &+ \frac{(-\mathrm{i})}{2}\int\mathrm{d}^3x_1\int_0^{-\mathrm{i}\beta}\mathrm{d}t_1\int\mathrm{d}^3x_2\int_0^{-\mathrm{i}\beta}\mathrm{d}t_2V(\mathbf{x}_1t_1;\mathbf{x}_2t_2) \\ &\quad\times\mathrm{Tr}\{\rho_{G_0}\mathbb{T}[\psi_I^\dagger(\mathbf{x}_1t_1)\psi_I^\dagger(\mathbf{x}_2t_2)\psi_I(\mathbf{x}_2t_2)\psi_I(\mathbf{x}_1t_1)\psi_I(\mathbf{x}t)\psi_I^\dagger(\mathbf{x}'t')]\} \\ &+ \cdots\Big].\end{aligned} \tag{A.17}$$

Still, time ordered products like the one in Eq. (A.17) have to be decomposed. A generalized Wick's theorem states that the traces in Eq. (A.14) are equal to the sum of all fully contracted terms, where the contraction of two field operators in the interaction picture is defined as

$$\dot{A}\dot{B} = \mathrm{Tr}\{\rho_{G_0}\mathbb{T}[AB]\} \tag{A.18}$$

The contraction is a complex number and not an operator. Note that the Green's function of the non-interacting system is just the contraction between a creation operator $\psi_I(\mathbf{x}t)$ and an annihilation operator $\psi_I^\dagger(\mathbf{x}'t')$

$$\mathrm{i}g^0(\mathbf{x}t;\mathbf{x}'t') = \mathrm{Tr}\{\rho_{G_0}\mathbb{T}[\psi_I(\mathbf{x}t)\psi_I^\dagger(\mathbf{x}'t')]\}. \tag{A.19}$$

A contraction between two creation operators or two annihilation operators vanishes. Using the invariance of the trace under cyclic permutations, the first order term in Eq. (A.17) can be arranged in six distinct ways such that each of these six contributions is a product of three non-vanishing contractions. Denoting creators by C and annihilators by A, and keeping the indices of the arguments, these six possible fully contracted terms are

$$\begin{aligned}\mathrm{Tr}\{\rho_{G_0}\mathbb{T}[C_1C_2A_2A_1AC']\} &= \dot{A}\dot{C}'\ddot{A}_1\ddot{C}_1\dddot{A}_2\dddot{C}_2 - \dot{A}\dot{C}'\ddot{A}_1\ddot{C}_2\dddot{A}_2\dddot{C}_1 + \dot{A}\dot{C}_2\ddot{A}_2\ddot{C}_1\dddot{A}_1\dddot{C}' \\ &- \dot{A}\dot{C}_2\ddot{A}_1\ddot{C}_1\dddot{A}_2\dddot{C}' + \dot{A}\dot{C}_1\ddot{A}_1\ddot{C}_2\dddot{A}_2\dddot{C}' - \dot{A}\dot{C}_1\ddot{A}_2\ddot{C}_2\dddot{A}_1\dddot{C}'.\end{aligned} \tag{A.20}$$

These contributions can be classified into two types. The first two terms are disconnected in the sense that they contain a contraction between the external fields $\psi_I(\mathbf{x}t)$ and $\psi_I^\dagger(\mathbf{x}'t')$ (denoted by $\dot{A}\dot{C}'$ in Eq. (A.20)). In this case, the contraction does not depend on the integration variables $\mathbf{x}_1$, t_1, $\mathbf{x}_2$ or t_2 and so the disconnected terms can be written as a product of a factor that contains the external points and a factor that contains only integration variables. The remaining four contributions are connected and do not factorize. This classification applies to all orders of the expansion.

A consequence of this factorization property for single disconnected terms is, that the whole expansion series (everything between the square brackets in Eq. (A.17)) factorizes into the sum $\mathbb{S}_{conn}(\mathbf{x}t;\mathbf{x}'t')$ of an infinite number of all connected contributions, that include also external indices, and a sum $\mathbb{S}_{int}$ of an infinite number of terms that do not depend upon the external variables, so that one can write

$$\mathrm{i}g(\mathbf{x}t;\mathbf{x}'t') = e^{\beta(\Omega-\Omega_0)}\left[\mathbb{S}_{conn}(\mathbf{x}t;\mathbf{x}'t')\times\mathbb{S}_{int}\right] \tag{A.21}$$

Wick's theorem can be applied in a similar form for the expansion of the partition function, Eq. (A.11). Inspecting the structure of the integrals, it can be verified that the expansion of $e^{-\beta\Omega}$ cannot contain external points. It turns out that $e^{-\beta(\Omega-\Omega_0)}$, the denominator of Eq. (A.21), is the sum of all internal contributions,

$$e^{-\beta(\Omega-\Omega_0)} = \mathbb{S}_{int}. \tag{A.22}$$

It follows that only the connected terms must be considered in the expansion of the Green's function,

$$\mathrm{i}g(\mathbf{x}t;\mathbf{x}'t') = \mathbb{S}_{conn}(\mathbf{x}t;\mathbf{x}'t'). \tag{A.23}$$

A further reduction of the number of connected terms can be achieved. The third and the fifth term of the six fully contracted objects in Eq. (A.20) can be generated from each other by exchanging the labels of the integration variables. They are topologically equivalent and give identical contributions. The same applies for term four and six. Generally, each connected contribution in nth order of the expansion of ig occurs in $2^n\, n!$ topologically equivalent permutations. This cancels the factor $\frac{1}{n!}$ in Eq. (A.14) and the $\frac{1}{2^n}$ that is introduced by the n interaction Hamiltionians.
The remaining topologically distinct connected contributions are, up to first order

$$\begin{aligned}\mathrm{i}g(\mathbf{x}t;\mathbf{x}'t') &= \mathrm{i}g^0(\mathbf{x}t;\mathbf{x}'t') + \mathrm{i}^2\int \mathrm{d}^3x_1 \int_0^{-\mathrm{i}\beta} \mathrm{d}t_1 \int \mathrm{d}^3x_2 \int_0^{-\mathrm{i}\beta} \mathrm{d}t_2 V(\mathbf{x}_1t_1;\mathbf{x}_2t_2) \\ &\quad \times\big[- g^0(\mathbf{x}t;\mathbf{x}_1t_1)g^0(\mathbf{x}_2t_2;\mathbf{x}_2t_2^+)g^0(\mathbf{x}_1t_1;\mathbf{x}'t') \\ &\quad + g^0(\mathbf{x}t;\mathbf{x}_2t_2)g^0(\mathbf{x}_2t_2;\mathbf{x}_1t_1)g^0(\mathbf{x}_1t_1;\mathbf{x}'t')\big] + \cdots \end{aligned} \tag{A.24}$$

By carrying out a similar analysis for higher order terms, an expansion of the full Green's function in terms of free propagators is obtained. For applications in uniform and isotropic systems, it is convenient to work with the Fourier transform of this expansion. All objects in Eq. (A.24), both on the right hand side and on the left hand side, are expressed by their Fourier representation, e.g.,

$$g(\mathbf{x}t;\mathbf{x}'t') = \int \frac{\mathrm{d}^3k}{(2\pi)^3}\, e^{\mathrm{i}\mathbf{k}(\mathbf{x}-\mathbf{x}')} \frac{1}{-\mathrm{i}\beta} \sum_\nu e^{-\mathrm{i}z_\nu(t-t')} g(k,z_\nu). \tag{A.25}$$

The first order terms contain a 12-dimensional integration and four Matsubara summations. The integral representation of the three-dimensional Dirac function,

$$\int \mathrm{d}^3x\, e^{\mathrm{i}\mathbf{k}\mathbf{x}} = (2\pi)^3\, \delta^{(3)}(\mathbf{k}), \tag{A.26}$$

and the useful relation for the Matsubara frequencies,

$$\int_0^{-\mathrm{i}\beta} \mathrm{d}t\, e^{-\mathrm{i}(z_\nu - z_{\nu'})t} = -\mathrm{i}\beta\, \delta_{z_\nu, z_{\nu'}}, \tag{A.27}$$

allow to express momentum and frequency conservation at each vertex. In this way, many of the integrals and the Matsubara summations can be eliminated. The final expression for the Fourier transform of the Green's functions expansion up to first order is given in Eq. (2.18) of Section 2.1.
It is clear that the procedure that was sketched in this Section becomes very tedious beyond the first order terms. Fortunately, for practical purposes, it is not necessary to compute all possible contractions of field operators and to perform Fourier transformations of complicated expressions. A set of rules, the so-called Feynman rules, takes advantage of the fact that each term in the expansion can be interpreted as a Feynman diagram and of the one-to-one correspondence between the diagrams and the mathematical expressions. By following these rules, the value of the nth order contribution to the Green's function can be determined much more quickly. For the momentum space representation of the Green's function series, the Feynman rules are given in Appendix B.

Appendix B

The Feynman Rules

The Feynman rules as stated below form a set of instructions to find the value of the nth-order contribution to the momentum-frequency representation of the Green's function, $g(k, z_\nu)$.

1. Draw all topologically distinct connected diagrams with n (wavy) interaction lines and $2n+1$ (straight) fermion lines. An arrow indicates the direction of momentum flow. Up to first order, this is shown in Fig. 2.1.

2. Associate a wave vector $\mathbf{k}_i$ and a discrete fermion Matsubara frequency z_{ν_i} with each line ($i = 1, \ldots, 2n$). One of the two external lines in each diagram must be labeled by $\mathbf{k}$ and z_ν.

3. To calculate the value of a diagram, write down a factor

   $$g^0(k_i, z_{\nu_i}) = \frac{1}{z_{\nu_i} - k_i^2/2m}$$

   for each fermion line labeled with $\mathbf{k}_i$ and z_{ν_i}.

4. With each potential line, associate a factor

   $$\mathrm{i}\,\langle \mathbf{k}_1\mathbf{k}_2|V|\mathbf{k}_3\mathbf{k}_4\rangle\,(2\pi)^3\;\delta^{(3)}(\mathbf{k}_1+\mathbf{k}_2-\mathbf{k}_3-\mathbf{k}_4)(-\mathrm{i}\beta)\delta_{\nu_1+\nu_2,\nu_3+\nu_4}.$$

   The labels of in-going and out-going propagator lines are shown in Fig. B.1. The Dirac function and the Kronecker delta guarantee the conservation of momentum and energy in the collision process.

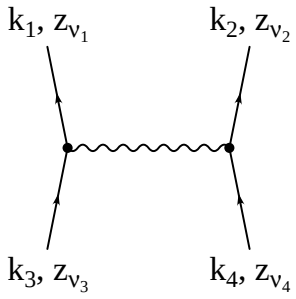

Figure B.1: *Orientation of the frequency and momentum labels in the factor that is associated with the potential line.*

5. Integrate over the momenta associated with all fermion lines except the external fermion line labeled by $\mathbf{k}$ and sum over all Matsubara frequencies except the one labeled by z_ν. Associate a factor $(2\pi)^{-3}$ with each integration and a factor $\frac{1}{-\mathrm{i}\beta}$ with each Matsubara summation.

6. Sum over all internal spin and isospin projections.

7. Add a factor $(-1)^F$ to the final expression, where F is the number of closed fermion loops in the respective diagram.

8. Whenever a propagator line either closes on itself or is joined by the same interaction line, insert a convergence factor $e^{z_\nu \eta}$, where $\eta = 0^+$ is small and positive such that

$$\lim_{\mathrm{Re}\, z \to \infty} \eta \,\mathrm{Re}\, z = \infty. \tag{B.1}$$

This factor is required to prevent divergent contributions from the arcs, for instance in the contour integration in Section 2.2.

Bibliography

[abr75] A.A. Abrikosov, L.P. Gorkov and I.E. Dzyaloshinsky, *Methods of Quantum Field Theory in Statistical Physics* (Dover, New York, 1975).

[alm93] T. Alm, B. L. Friman, G. Röpke and H. Schulz, *Nucl. Phys. A* **551**, 45 (1993).

[alm96] T. Alm, G. Röpke, A. Schnell, N.H. Kwong and H.S. Köhler, *Phys. Rev. C* **53**, 2181 (1996).

[ami96] K. Amir-Azimi-Nili, H. Müther, L.D. Skouras, and A.Polls, *Nucl. Phys. A* **604**, 245 (1996).

[bal90] M. Baldo, I. Bombaci, G. Giansiracusa, U. Lombardo, C. Mahaux and R. Sartor, *Phys. Rev. C* **41**, 1748 (1990).

[bal92] M. Baldo, I. Bombaci, and U. Lombardo, *Phys. Lett.* **B 283**, 8 (1992).

[bat01] M.F. van Batenburg, Ph.D. Thesis, Utrecht (2001).

[ben89] O. Benhar, A. Fabrocini, and S. Fantoni, *Nucl. Phys. A* **505**, 267 (1989).

[ben90] O. Benhar, A. Fabrocini, and S. Fantoni, *Phys. Rev. C* **41**, R24 (1990).

[ben94] O. Benhar, A. Fabrocini, S. Fantoni and I. Sick, *Nucl. Phys. A* **579**, 493 (1994).

[bis98] R. Bishop in *Microscopic Quantum Many-Body Theories and Their Applications*, eds. J. Navaro and A. Polls, (Springer 1998).

[bru54] K.A. Brueckner and C.A. Levinson and H.M. Mahmoud, *Phys. Rev.* **95**, 217 (1954).

[bru58] K.A. Brueckner and J.L. Gammel, *Phys. Rev.* **109**, 123 (1958).

[bet36] H.A. Bethe, Rev. Mod. Phys. **8**, 139 (1936).

[bet63] H.A. Bethe, B.H. Brandow and A.G. Petschek, *Phys. Rev.* **129**, 225 (1963).

[blo58] C. Bloch and C. De Dominicis, *Nucl. Phys.* **7**, 459 (1958).

[boz99] P. Bożek, *Nucl. Phys. A* **657**, 187 (1999).

[boz01] P. Bożek and P. Czerski, *Eur. Phys. J. A* **11**, 271 (2001).

[boz02a] P. Bożek, *Phys. Rev. C* **65**, 054306 (2002).

[boz02b] P. Bożek, *Eur. Phys. J. A* **15**, 325 (2002).

[boz03] P. Bożek and P. Czerski, Acta Phys. Polon. B **34**, 2759 (2003).

[car91] J.A. Carlson and R.B. Wiringa in *Computational Nuclear Physics*, eds. K. Langanke, J.A. Maruhn and S.E. Koonin, (Springer 1991).

[cep95] D.M. Ceperley, Rev. Mod. Phys. **67**, 279 (1995).

[cla59] J.W. Clark and E. Feenberg, *Phys. Rev.* **113**, 388 (1959).

[cla79] J. Clark, Prog. in Part. and Nucl. Phys. **2**, 89 (1979).

[coe70] F. Coester, S. Cohen, B. Day and C.M. Vincent, *Phys. Rev. C* **1**, 769 (1970).

[day67] B.D. Day, Rev. Mod. Phys. **39**, 719 (1967).

[dew00] Y. Dewulf, Ph.D. Thesis, Gent (2000).

[dew02] Y. Dewulf, D. Van Neck, and M. Waroquier, *Phys. Rev. C* **65**, 054316 (2002).

[dew03] Y. Dewulf, W.H. Dickhoff, D. Van Neck, E.R. Stoddard and M. Waroquier, *Phys. Rev. Lett.* **90**, 2003 (152501).

[dic81] W.H. Dickhoff, A. Faessler, J. Meyer-ter-Vehn and H. Müther, *Phys. Rev. C* **23**, 1154 (1981).

[dic82] W.H. Dickhoff, A. Faessler and H. Müther, *Nucl. Phys. A* **389**, 492 (1982).

[dic83] W.H. Dickhoff, A. Faessler, H. Müther and S. Wu, *Nucl. Phys. A* **405**, 534 (1983).

[dic92] W.H. Dickhoff and H. Müther, Rep. Prog. Phys. **11**, 1947 (1992).

[dic99] W.H. Dickhoff, C.C. Gearhart, E.P. Roth, A. Polls and A. Ramos, *Phys. Rev. C* **60**, 064319 (1999).

[fan84] S. Fantoni and V.R. Pandharipande, *Nucl. Phys. A* **427**, 473 (1984).

[fan98] S. Fantoni and A. Fabrocini in *Microscopic Quantum Many-Body Theories and Their Applications*, eds. J. Navaro and A. Polls, (Springer 1998).

[fee69] E. Feenberg, *Theory of Quantum Fluids* (Academic Press, New York, 1969).

[fet71] A.L. Fetter and J.D. Walecka, *Quantum Theory of Many-Particle Systems*, McGraw-Hill Publishing Company Inc., New York (1971).

[fri02] T. Frick, Kh. Gad, H. Müther and P. Czerski, *Phys. Rev. C* **65**, 34321 (2002).

[fri03] T. Frick and H. Müther, *Phys. Rev. C* **68**, 034310 (2003).

[fri04] T. Frick, H. Müther and A. Polls, `nucl-th/0401015`.

[fro77] B. Frois, J.B. Bellicard, J.M. Cavedon, M. Huet, P. Leconte, P. Ludeau, A. Nakada, Phan Zuan Hô and I. Sick, *Phys. Rev. Lett.* **38**, 152 (1977).

[gol57] J. Goldstone, Proc. Roy. Soc. A **239**, 267 (1957).

[gor58] L.P. Gorkov, JETP **34**, 505 (1958).

[gra89] P. Grangé, A. Lejeune, M. Martzloff and J.-F. Mathiot, *Phys. Rev. C* **40**, 1040 (1989).

[gua98] R. Guardiola in *Microscopic Quantum Many-Body Theories and Their Applications*, eds. J. Navaro and A. Polls, (Springer 1998).

[haf70] M. I. Haftel and F. Tabakin, *Nucl. Phys. A* **158**, 1 (1970).

[hei95] E. Heinz, H. Müther and H.A. Mavromatis, *Nucl. Phys. A* **587**, 77 (1995).

[hug58] N.M. Hugenholtz and L. Van Hove, *Physica* **24**, 363 (1958).

[jac98] J.D. Jackson, *Classical Electrodynamics* (John Wiley & Sons, New York, 1998).

[jac82] A.D. Jackson, A. Lande and R.A. Smith, *Phys. Rep.* **86**, 55 (1982).

[jeu76] J.P. Jeukenne, A. Lejeune and C. Mahaux, *Phys. Rep.* **25**, 83 (1976).

[kad62] L.P. Kadanoff and G. Baym, *Quantum Statistical Mechanics* (Benjamin, New York, 1962).

[kra86] W.D. Kraeft, D. Kremp, W. Ebeling and G. Röpke, *Quantum Statistics of Charged Particle Systems* (Akademie-Verlag, Berlin, 1986).

[kue78] H. Kümmel, K.H. Lührmann and J.G. Zabolitzky, *Phys. Rep.* **36**, 1 (1978).

[lut61] J.M. Luttinger, *Phys. Rev.* **121**, 942 (1961).

[mac89] R. Machleidt, Adv. Nucl. Phys. **19**, 189 (1989).

[mac96] R. Machleidt, F. Sammarruca and Y. Song, *Phys. Rev. C* **53**, R1483 (1996).

[mar59] P.C. Martin and J. Schwinger *Phys. Rev.* **115**, 1342 (1959).

[mat67] R. D. Mattuck, *A Guide to Feynman Diagrams in the Many-Body Problem*, (McGraw-Hill Publishing Company Ltd., London, 1967).

[mut95] H. Müther, G. Knehr, and A. Polls, *Phys. Rev. C* **52**, 2955 (1995).

[nam60] Y. Nambu *Phys. Rev.* **117**, 648 (1960).

[neg88] J.W. Negele and H. Orland, *Quantum Many-Particle Systems*, (Addison-Wesley, Reading, 1988).

[pie98] S.C. Pieper in *Microscopic Quantum Many-Body Theories and Their Applications*, eds. J. Navaro and A. Polls, (Springer 1998).

[ram88] A. Ramos, Ph.D. Thesis, Barcelona, (1988).

[ram89] A. Ramos, A. Polls, and W.H. Dickhoff, *Nucl. Phys. A* **503**, 1 (1989).

[rei68] R.V. Reid, Ann. Phys. (N.Y.) **50**, 411 (1968).

[roh03] D. Rohe, *Eur. Phys. J. A* **17**, 493 (2003).

[rot00] E.P. Roth, Ph.D. Thesis, St. Louis, (2000).

[sak95] J.J. Sakurai, *Modern Quantum Mechanics* (Addison-Wesley, Reading, 1995).

[sar96] R. Sartor, *Phys. Rev. C* **54**, 809 (1996).

[sch90] M. Schmidt, G. Röpke and H. Schulz, Ann. Phys. (N.Y.) **202**, 57 (1990).

[snl96] A. Schnell, Ph.D. Thesis, Rostock (1996).

[slr99] E. Schiller, H. Müther and P. Czerski, *Phys. Rev. C* **59**, 2934 (1999); *Phys. Rev. C* **60**, 059901(E) (1999).

[sic91] I. Sick and P.K.A. deWitt Huberts, Comm. Nucl.Part. Phys. **20**, 177 (1991).

[son98] H.Q. Song, M. Baldo, G. Giansiracusa and U. Lombardo, *Phys. Rev. Lett.* **81**, 1584 (1998).

[sto94] V.G.J. Stoks, R.A.M. Klomp, C.P.F. Terheggen and J.J. de Swart *Phys. Rev. C* **49**, 2950 (1994).

[suz00] K. Suzuki, R. Okamato, M. Kohno and S. Nagata, *Nucl. Phys. A* **665**, 92 (2000).

[ter91] A.R. Tereno, Ph.D. Thesis, Tübingen (1991).

[tho60] D.J. Thouless, Ann. Phys. (N.Y.) **10**, 553 (1960).

[var88] D.A. Varshalovich, A.N. Moskalev and V.K. Khersonskii *Quantum Theory of Angular Momentum*, (World Scientific, Singapore, 1988).

[von90] B.E. Vonderfecht, C.C. Gearhart, W.H. Dickhoff, A. Polls and A. Ramos, *Phys. Lett. B* **253**, 1 (1990).

[von91] B.E. Vonderfecht, W.H. Dickhoff, A. Polls and A. Ramos, *Phys. Rev. C* **44**, R1265 (1991).

[von93] B.E. Vonderfecht, W.H. Dickhoff, A. Polls and A. Ramos, *Nucl. Phys. A* **555**, 1 (1993).

[wei36] C.F. von Weizsäcker, Z. Phys. **96**, 431 (1936).

[wir88] R.B. Wiringa, V. Fiks and A. Fabrocini, *Phys. Rev. C* **38**, 1010 (1988).

[wir95] R.B. Wiringa, V.G.J. Stoks and R. Schiavilla, *Phys. Rev. C* **51**, 38 (1995).

[yuk35] H. Yukawa, Prog. Phys. Math. Soc. Jpn. **17**, 48 (1935).

[zuo99] W. Zuo, I. Bombaci and U. Lombardo, *Phys. Rev. C* **60**, 024605 (1999).

Zusammenfassung in deutscher Sprache

In der vorliegenden Arbeit werden Nukleon-Nukleon (NN)-Korrelationen in symmetrischer Kernmaterie im Rahmen der Theorie selbstkonsistenter Green'scher Funktionen (SCGF) bei endlichen Temperaturen und endlichem chemischen Potential untersucht. Dabei wird ein realistisches Modell für die Kernkraft zugrundegelegt, welches in der Lage ist, die zugänglichen Zwei-Nukleon Daten aus NN-Streuung sowie die Eigenschaften des Deuterons mit hoher Präzision zu beschreiben. Ausgehend von der diagrammatischen Entwicklung der Ein-Teilchen Green's Funktion im Medium werden zunächst am Beispiel der Hartree-Fock-Naeherung grundlegende Begriffe wie die selbstkonsistente Renormierung der Selbstenergie-Diagramme sowie Techniken zur Berechnung von Matsubara-Summen erklärt. Zur Beschreibung stark korrelierter Vielteilchen-Systeme ist jedoch die Hartree-Fock-Naeherung ungeeignet, da Korrelationen in den HF-Produktwellenfunktionen nicht beruecksichtigt werden koennen. Insbesondere die Vernachlässigung von kurzreichweitigen Korrelationen (SRC), die genau solche Konfigurationen, in denen NN-Paare kleine Relativabstände haben, unterdrücken, führt zu einer unphyikalischen Übergewichtung der repulsiven Beiträge im NN-Potential und zu ungebundenen Systemen. Eine geeignete Methode, solche kurzreichweitigen Korrelationen sowie die v.a. durch das Pion vermittelten Tensorkorrelationen zu berücksichtigen, ist die thermodynamische T-Matrix, eine effektive Wechselwirkung, die durch eine Streugleichung im Medium bestimmt wird. Ähnlich wie in der Lippmann-Schwinger-Gleichung, die die Streuung freier Teilchen beschreibt, werden dabei die sogenannten Leiter-Diagramme aufsummiert. Die Integralgleichung beinhaltet eine Zweiteilchen-Green'sche Funktion, die die Propagation von zwei nicht wechselwirkenden Nukleonen zwischen den einzelnen Streuprozessen beschreibt.

Während in allen bisher durchgefuehrten Rechnungen dieser Art auf verschiedene Naeherungsmethoden zur Lösung der T-Matrix Gleichung zurückgegriffen wurde, wird die Zweiteilchen-Green'sche Funktion in der hier vorliegenden Arbeit als Produkt aus zwei vollwertigen Einteilchen-Propagatoren in ihrer vollen Energie-und Impulsabhängigkeit explizit berechnet. Neben der üblichen Berücksichtigung von Teilchen-Teilchen Propagation wird dabei auch Loch-Loch-Propagation in allen Ordnungen berücksichtigt.
Aus der effektive Wechselwikung wird die Selbstenergie der Nukleonen bestimmt. Die Berechnung dieser komlexwertigen Größe wird durch die Anwendung von Dispersionsrelationen möglich, die eine Trennung von Real-und Imaginärteil erlauben. Aus der Selbstenergie kann leicht die Spektralfunktion der Nukleonen bestimmt werden. Dies ist eine zentrale Größe in der Theorie Green'scher Funktionen, die dem Imaginärteil der Einteilchen-Green'schen Funktion proportional ist, und die die Energieverteilung quantenmechanischer Impulszustände beschreibt. In einem korrelierten Vielteilchen-System ist nämlich eine strenge Energie-Impuls-Relation wie für freie Teilchen nicht mehr erfüllt, und ein Teilchen in einem definierten Impulszustand ist deshalb über verschiedene sogenannte "off-shell"-Energien verschmiert.
Ein wesentlicher Punkt bei dem beschriebenen Verfahren ist, dass die Bestimmung der "off-shell"-Struktur der Spektralfunktion in selbstkonsistenter Weise erfolgt, was bei Quasiteilchen-Näherungen (QPGF) nicht der Fall ist. Dort wird bei der Berechnung der effektiven Wechselwirkung und der Selbstenergie angenommen, dass die Nukleonen "on-shell" sind, also eine Energie-Impuls-relation erfüllen, was die Lösung des gekoppelten Gleichungssystems stark vereinfacht. Ist die Spektralfunktion einmal bestimmt, können alle Einteilchen-Observable sowie die Grundzustandsenergie des Vielteilchen-Systems aus ihr berechnet werden.
Daneben ist die Spektralfunktion auch eine bestimmende Größe bei "knock-out"-Reaktionen, bei denen z.B. durch Beschuß mit hochenergetischen Elektonen ein Proton aus einem Atomkern herausgeschlagen und detektiert wird. Der Wirkungsquerschnitt für solche Kernreaktionen ist proportional zur Spektralfunktion.

Die Ergebnisse der selbstkonsistenten T-Matrix zeigen deutliche Abweichungen von den Resultaten, die in Quasiteilchen-Näherungen berechnet wurden. Die Unterschiede lassen sich konkret auf die Nährungen zurückführen, die bei der Bestimmung Zweiteilchen-Green'schen Funktion gemacht werden. In der QPGF-Beschreibung werden insbesondere solche Beiträge zur T-Matrix zu stark unterdrückt, die von den Loch-Loch-Leiterdiagrammen bei stark negativen Paarener-

gien herrühren. Ein anderes interessantes Phänomen, der Übergang zu einer suprafluiden Phase, kann im Rahmen des Formalismus "normaler" Green'scher Funktionen nicht beschrieben werden. Allerdings läßt dich die Übergangstemperatur T_C des Phasenübergangs durch die Bedingung bestimmen, dass bestimmte T-Matrixelemente singulär werden. Dabei zeigt sich, dass die Quasiteilchen-Näherung T_C überschätzt, da SCGF-Rechnungen in der normalen Phase noch bei Temperaturen durchgefürht werden können, die schon unterhalb der Übergangstemperatur der Quasiteilchen-Näherung liegen.
Aus der T-Matrix und der Spektralfunktion kann der Imaginärteil der Selbstenergie berechnet werde. Die Energie-, die Impuls- und die Dichteabhängigkeit dieser Größe wird in der Arbeit ausführlich diskutiert. Da die Energieabhängigkeit der Selbsenergie relativ glatt ist, eignet sich diese auch zur Extrapolation der Ergebnisse bei endlicher Temperatur auf $T = 0$, was insbesondere für den Vergleich mit experimentellen Ergebnissen wichtig ist.

Beim Vergleich der Resultate der selbstkonsistenten Spektralfunktion mit den QPGF-Ergebnissen zeigt sich, dass sich die oben auf der Ebene der T-Matrix beschriebene Unterdrückung bei stark negativen Energien auch auf der Ebene der QPGF-Spektralfunktion auswirkt. Die Temperatur- und Dichteabhängigkeit der Spektralfunktion im Bereich von $3\,\mathrm{MeV} < T < 20\,\mathrm{MeV}$ und $0.1\,\mathrm{fm}^{-3} < \rho < 0.5\,\mathrm{fm}^{-3}$ werden ebenfalls diskutiert. Eine erst kürzlich aus den experimentallen Daten einer (e,e'p)-Reaktion an ^{12}C extrahierte Spektralfunktion wird mit einer selbstkonsistent berechneten Spektralfunktion bei mittleren Dichte des Kohlenstoff-Kerns verglichen. Die Rechnung zeigt eine recht gute Übereinstimmung mit den experimentellen Daten, was deshalb erstaunlich ist, weil die Daten besser beschrieben werden als von kürzlich publizierten Rechnungen, die speziell für endliche Systeme durchgeführt wurden.
Auch für die Besetzung der tief gebundenen Zustände in ^{208}Pb existieren experimentell gemessene Werte. SRC sorgen bereits im Grundzustand dafür, dass ein bestimmter Anteil der Nukleonen in den Zuständen, die eigentlich voll besetzt sind, zu sehr hohen Impulszuständen gestreut werden, so dass die Orbitale im Bereich unterhalb der Fermikante nur teilweise besetzt, und diejenigen oberhalb der Fermikante nicht völlig unbesetzt sind. Die experimentell bestimmten Werte für Blei können mit der Besetzungszahlen $n(k)$ der Zustände mit kleinen Impulsen in Kernmaterie verglichen werden. Der auf Temperatur Null extrapolierte Wert für $n(0)$ ist allerdings mit 0.89 um mehr als 10% größer als der Mittelwert aus den fünf tiefstgebundenen Zustände in Blei. Allerdings sind die experimenellen Feh-

lerbalken ebenfalls recht groß. In der Arbeit wird außerdem die Besetzung von Zuständen mit sehr hohem Impuls diskutiert.
Zum Schluß wird das Sättigungsverhalten von Kernmaterie studiert. Dafür wird die interne Energie pro Nukleon mit der sogenannten Koltun-Summenregel berechnet. Im Vergleich zu einer "continuous choice" Brueckner-Hartree-Fock (BHF)-Rechnung, die ebenfalls von Quasiteilchen ausgeht, kann ein repulsiver Effekt beobachtet werden, der bei hohen Dichten (ca. $3\rho_0$) auf ca. 6 MeV anwächst. Diese Repulsion ist auf die Loch-Loch-Propagation zurückzuführen. Der Sättigungspunkt von Kernmaterie wird dadurch zu etwas niedrigeren Dichten verschoben, allerdings bei weitem nicht in die Nähe von ρ_0.
Eine genauere Analyse des Ursprungs für den repulsiven Effekt zeigt, dass diejenigen Nukleonen, die sich in nur teilweise besetzten Orbitalen mit sehr hohen Impulsen aufhalten, einen stark attraktiven Beitrag zur Gesamtenergie des Systems leisten, und das owohl sie eine sehr hohe kinetische Energie besitzen. Diese Nukleonen sind "off-shell" und können in einer reinen Quasiteilchen-Näherung wie der BHF-Theorie nicht beschrieben werden. Der im Saldo repulsive Effekt liegt somit darin begründet, dass die Bindung von Nukleonen in Orbitalen mit kleineren Impulsen sehr viel schwächer ist als im BHF-Bild.

Die in der vorliegenden Arbeit erarbeitete Lösung für die Green'sche Funktion ermöglicht eine konsistente Beschreibungs unendlich ausgedehnter nukleare Systeme bei endlichen Temperaturen und in einem weiten Dichtebereich. Die Resultate können ohne größere Schwierigkeiten auf Temperatur Null extrapoliert werden, was einen Vergleich mit Messungen an endlichen Systemen erlaubt. Da die eigentlich in endlichen Systemen anzuwendenden theoretischen Methoden grundsätzlich anders (und schwieriger) sind, sollte man jedoch nicht vergessen, dass solche Vergleiche letztlich höchstens qualitativen Charakter haben können.
Anders sieht dies mit Anwendungen in astrophysikalischen Systemen wie Neutronensternen aus, wo Effekte, die durch die endliche Ausdehnung des Systems herrühren, keine Rolle spielen. Ein erster weiterer Schritt zur realistischen Beschreibung hadronischer Materie im Inneren eines Neutronensterns wäre die Berechnung β-stablier asymmetrischer Kernmaterie unter Einbeziehung der "off-shell"-Struktur der Neutronen-und der Protonen-Spektralfunktion. Darüber hinausgehend könnte dann das Auftreten anderer Leptonen wie des μ^- sowie von Baryonen mit "Strangeness" wie des Σ^- oder des Λ bei hohen Dichten modelliert werden. Für solche Projekte bildet der im Rahmen dieser Arbeit erarbeitete Computer-Code die Ausgangsbasis.

Danksagung

An dieser Stelle möchte ich allen, die zum Gelingen dieser Arbeit beigetragen haben, meinen Dank aussprechen.

An erster Stelle möchte ich dem Betreuer meiner Arbeit, Herrn Prof. Dr. Herbert Müther für die maßgebliche Unterstützung bei der Bearbeitung des Themas danken. Er hatte für die auftretenden Fragen und Probleme immer ein offenes Ohr und war während der ganzen Zeit stets bereit für fruchtbare fachliche Diskussionen. Er hat es mir auch ermöglicht, meine Ergebnisse auf mehreren nationalen und internationalen Tagungen zu präsentieren.

Mein besonders herzlicher Dank gilt Herrn Prof. Dr. Arturo Polls, der mich in vielen Gesprächen immer motiviert hat. Unter anderem während zahlreicher Aufenthalte in Barcelona habe ich von ihm fachlich, aber auch menschlich viel gelernt.

Danken möchte ich auch den aktuellen und ehemaligen Mitgliedern meiner Arbeitsgruppe, Khaled Hassaneen, Jan Kuckei, Fernando Montani und Oliver Plohl.

Während der ganzen Zeit war ich darauf angewiesen, die Computer-Infrastruktur des Instituts zu nutzen. Deshalb möchte ich mich auch bei den System-Administratoren Dominik Epple, Christian Fischer, Jochen Gattnar, Markus Kloker, Christian Korn und Laurent Moyaerts bedanken.

Für die finanzielle Unterstützung der Arbeit durch ein Graduiertenstipendium danke ich dem Europäischen Graduiertenkolleg Basel-Tübingen „Hadronen im Vakuum, in Kernen und Sternen“.

Nicht zuletzt danke ich auch meiner Freundin Linda und meinen Eltern, die mich immer mit sehr viel Geduld und Liebe begleitet haben.